AD-A064 933 AIR FORCE INST OF TECH WRIGHT-PATTERSON AFB OHIO SCH--ETC F/G 20/12
INVESTIGATION OF WEB-DENDRITE SILICON.(U)
DEC 78 T J SETTECERRI

UNCLASSIFIED AFIT/GEO/PH/78D-4 NL

1 OF 2
AD
A064933

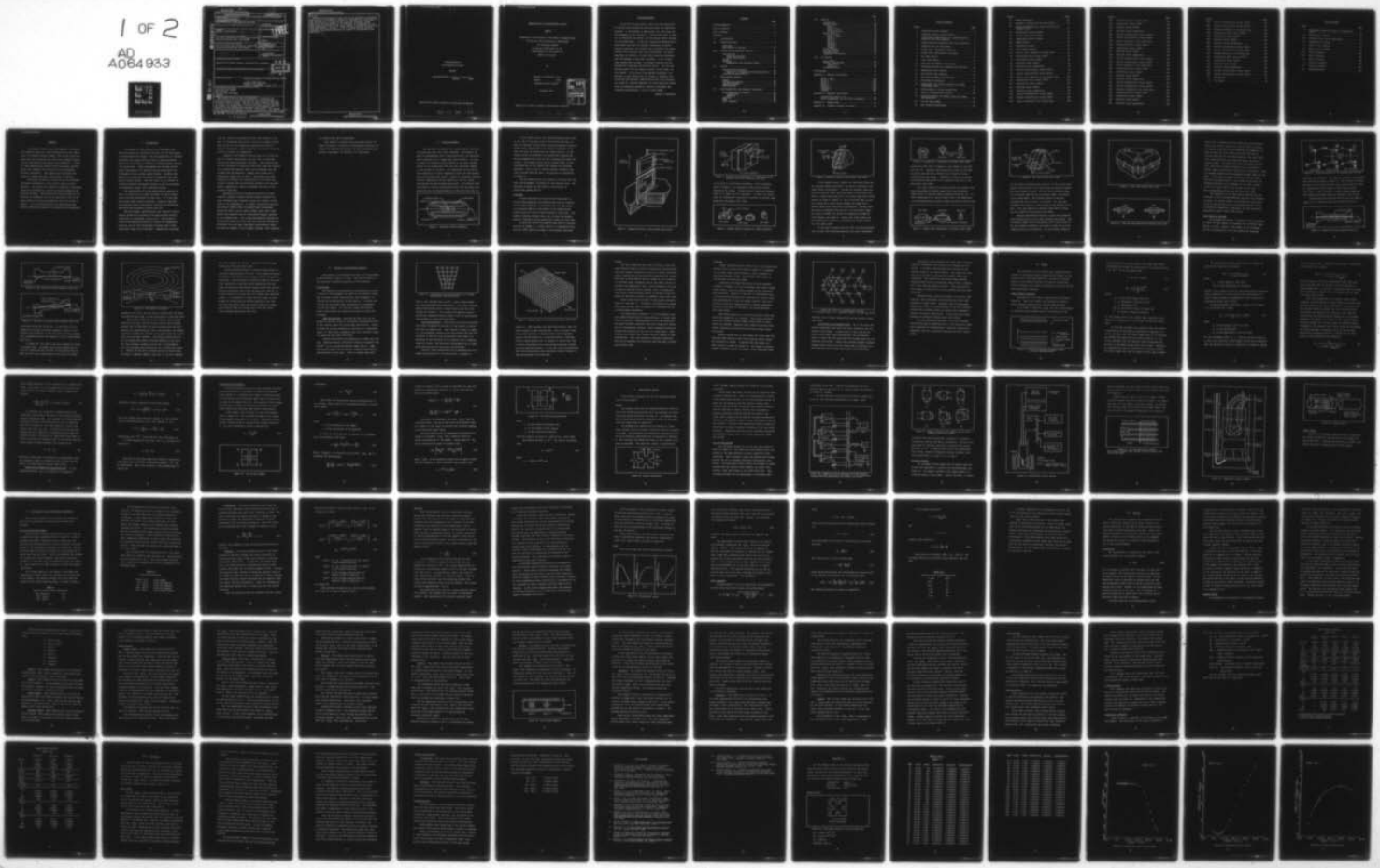

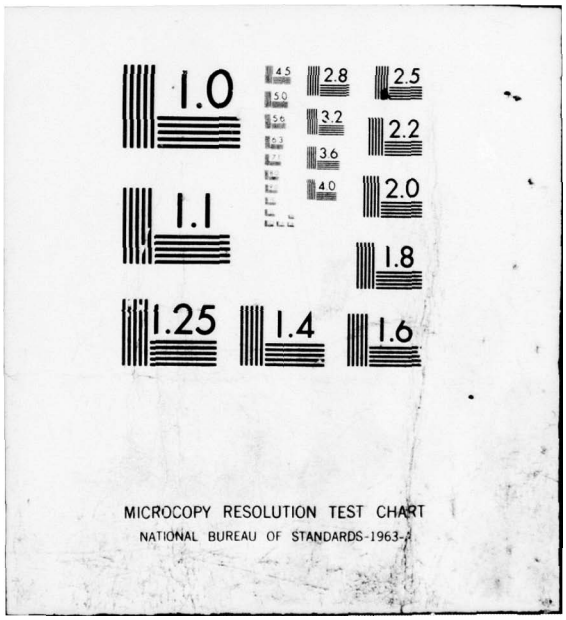
1.0
1.1
1.25
1.4
1.6
1.8
2.0
2.2
2.5
2.8
3.2
3.6
4.0
4.5
5.0
5.6
6.3
MICROCOPY RESOLUTION TEST CHART
NATIONAL BUREAU OF STANDARDS-1963-A

UNCLASSIFIED

SECURITY CLASSIFICATION OF THIS PAGE (When Data Entered)

REPORT DOCUMENTATION PAGE	READ INSTRUCTIONS BEFORE COMPLETING FORM
1. REPORT NUMBER: AFIT/GEO/PH/78D-4	2. GOVT ACCESSION NO. / 3. RECIPIENT'S CATALOG NUMBER
4. TITLE (and Subtitle): INVESTIGATION OF WEB-DENDRITE SILICON.	5. TYPE OF REPORT & PERIOD COVERED: MS Thesis
	6. PERFORMING ORG. REPORT NUMBER
7. AUTHOR(s): Thomas J. Settecerri (Master's Thesis)	8. CONTRACT OR GRANT NUMBER(s)
9. PERFORMING ORGANIZATION NAME AND ADDRESS: Air Force Institute of Technology (AFIT-EN), Wright-Patterson AFB, Ohio 45433	10. PROGRAM ELEMENT, PROJECT, TASK AREA & WORK UNIT NUMBERS: 23000106
11. CONTROLLING OFFICE NAME AND ADDRESS: Air Force Material Laboratory (AFML-LPO), Wright-Patterson AFB, Ohio 45433	12. REPORT DATE: December 1978
	13. NUMBER OF PAGES: 169
14. MONITORING AGENCY NAME & ADDRESS (if different from Controlling Office)	15. SECURITY CLASS. (of this report): Unclassified
	15a. DECLASSIFICATION/DOWNGRADING SCHEDULE

16. DISTRIBUTION STATEMENT (of this Report)

Approved for public release; distribution unlimited.

17. DISTRIBUTION STATEMENT (of the abstract entered in Block 20, if different from Report)

18. SUPPLEMENTARY NOTES

Approved for public release; IAW AFR 190-17

JOSEPH P. HIPPS, Maj, USAF
Director Of Information
19 Jan 79

19. KEY WORDS (Continue on reverse side if necessary and identify by block number)

Web-Dendrite Silicon
Dendritic-Web Growth
Web Silicon
van der Pauw Technique
Dendrite

20. ABSTRACT (Continue on reverse side if necessary and identify by block number)

Web-dendrite silicon was investigated to establish its potential value as a starting material for the fabrication of infrared detector arrays. The van der Pauw technique was used to measure the electrical transport properties of this material and assess its homogeneity. A total of eight samples were prepared from boron-doped, gallium-doped, and "undoped" web provided by the Westinghouse Electric Corporation. The samples were evaluated with respect to growth direction and position in → over

DD FORM 1 JAN 73 1473 EDITION OF 1 NOV 65 IS OBSOLETE

UNCLASSIFIED

SECURITY CLASSIFICATION OF THIS PAGE (When Data Entered)

012225

AD A064933

DDC FILE COPY

LEVEL II

DDC
RECEIVED
FEB 22 1979
A

the web.

The growth procedures of web silicon are discussed; including a description of the defects common to this material. The results are analyzed to determine uniformity, impurity concentrations, and the activation energy of the majority carriers. These particular web specimens are not suitable as candidates for device fabrication, due to the large numbers of dislocations/defects they were found to contain. It is not known whether the dislocations and defects observed are common to all dendritic-web materials.

AFIT/GEO/PH/78D-3

INVESTIGATION OF
WEB-DENDRITE SILICON

THESIS

AFIT/GEO/PH/78D-3 Thomas J. Settecerri
Captain USAF

Approved for public release; distribution unlimited.

79 01 30 165

AFIT/GEO/PH/78D-4

INVESTIGATION OF WEB-DENDRITE SILICON

THESIS

Presented to the Faculty of the School of Engineering
of the Air Force Institute of Technology
Air Training Command
in Partial Fulfillment of the
Requirements for the Degree of
Master of Science

by

Thomas J. Settecerri, B.S.
Captain USAF
Graduate Electro-Optics

December 1978

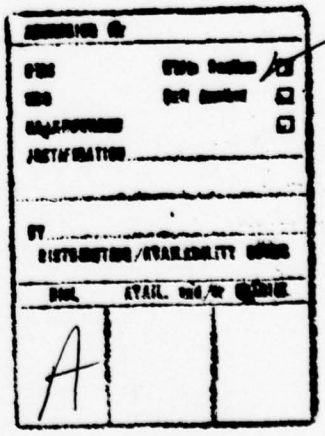

Approved for public release; distribution unlimited

79 01 30 165

Acknowledgements

As is true of any project, there are many associates or friends whose assistance and advice make its completion possible. I am grateful to many people for their help and encouragement in this endeavor. I would first like to thank Dr. D. Shankland, my advisor, for his timely advice throughout this experiment. I must also express my appreciation to Steve Smith and Paul von Richter, University of Dayton Research Institute, for without their assistance the experimental work could not have been accomplished. But most important, as cohorts in crime, their enduring friendship made the passage of time more enjoyable. To Dr. Joseph Lang, Thomas More College, I am deeply indebted for his mathematical expertise and skillful advice. His time and patience spent with me helped to layout a more clear, concise thesis. In the area of web growth techniques I am grateful to have worked with Lt. Thomas C. Chandler; his references and personal communications were most valuable. And lastly Dr. Patrick Hemenger, Air Force Materials Laboratory; his dedicated guidance, extensive knowledge, and tremendous perseverance I can not thank enough.

Thomas J. Settecerri

Contents

		Page
Acknowledgements		ii
List of Figures		v
List of Tables		ix
Abstract		x
I.	Introduction	1
II.	Growth Procedure	4
	Dendrites	5
	Twin Planes in the Web	12
III.	Defects in Web-Dendrite Silicon	17
	Dislocations	17
	Edge Dislocations	17
	Screw Dislocations	18
	Linage	20
	Twinning	21
	Noncoherent and Secondary Twins	22
IV.	Theory	24
	Charge Balance Equation	24
	High and Low Temperature Characteristics	28
	Resistivity and Mobility	30
V.	Experimental System	34
	Sample	34
	van der Pauw System	35
	Equipment System	37
	Sample Holder	41
VI.	Data Acquisition and Analysis Techniques	42
	Data Collection Procedures	42
	Resistivity	44
	Mobility	44
	Analysis	46
	Data	48
	Error Analysis	49

Page

VII. Results 53

Assumptions 53
Samples Tested 54
Boron 1 56
Boron 2 56
Boron 3 and 4 56
Gallium 1 and 2 56
Sample Results 57
Boron 1 run 1 57
Boron 1 run 2 58
Boron 2 59
Boron 3 60
Boron 4 61
Gallium 1 62
Gallium 2 63
Undoped 64
Curve Fitting 66
Etching Results 66
Flatness Report 67
Comparison of Results 67

VIII. Conclusion 71

R_2/R_1 Ratio 71
Further Observations 74
Resistivity 74
Mobility 74
Recommendations 74

Bibliography 76

Appendix A: Results and Figures A1

Boron 1 run 1 . . . . . A1
Boron 1 run 2 . . . . . A10
Boron 2 . . . . . A19
Boron 3 . . . . . A28
Boron 4 . . . . . A37
Gallium 1 . . . . . A46
Gallium 2 . . . . . A55
Undoped A64

Appendix B: Expanded Derivations B1

Resistivity versus 1/T B1
Error Propagation for One Level Acceptors B3

Appendix C: Dektak Scan C1

Appendix D: Computer Program Flow Chart D1

List of Figures

Figure		Page
1	Idealized Growth Schematic	4
2	Schematic Section of Web Growth	6
3	Orientation Relationship of a Diamond-Lattice Dendrite with Twin Lamellae	7
4	Single Crystal Oriented in any <211> Direction .	7
5	Dendrite with one Twin Plane	8
6	Single Twin "Favorable" Direction	9
7	Single Twin "Unfavorable" Direction	9
8	Two Twin Planes	10
9	Three Twin Planes	11
10	Even and Odd Numbered Twin Planes	11
11	Twinning Operation for Diamond-Like Lattices . .	13
12	Symmetrical Twin Lamellae	13
13	Web without Twin Lamellae	14
14	Web with Secondary Twin Lamellae	14
15	Web-Dendrite Schematic	15
16	Compression and Dilation Region at an Edge Dislocation Site	18
17	Spiral Ramp of a Screw Dislocation	19
18	Twin in a Hypothetical Lattice	22
19	Relative Position of Energy Levels in p-type Semiconductors	24
20	van der Pauw Sample	30
21	Hall Mobility Measurement	33

Figure		Page
22	Sample Dimensions	34
23	Diagram of Guarded van der Pauw System	36
24	Sample Connections for taking van der Pauw Transport Data	37
25	Experimental System Design	38
26	van der Pauw Wiring Detail	39
27	Temperature Control System	40
28	Sample Holder	41
29	Theoretical Curves	48
30	Boron-Doped Samples	61
A1	Boron 1 run 1 Relative to Growth Axis	A1
A2	Resistivity Ratio versus 1000/T	A4
A3	Resistivity versus 1000/T	A5
A4	Mobility versus 1000/T	A6
A5	Mobility versus Temperature	A7
A6	Carrier Concentration versus 1000/T	A8
A7	Carrier Concentration versus 1000/T	A9
A8	Boron 1 run 2 Relative to the Growth Axis . . .	A10
A9	Resistivity Ratio versus 1000/T	A13
A10	Resistivity versus 1000/T	A14
A11	Mobility versus 1000/T	A15
A12	Mobility versus Temperature	A16
A13	Carrier Concentration versus 1000/T	A17
A14	Carrier Concentration versus 1000/T	A18
A15	Boron 2 Relative to the Growth Axis	A19

Figure		Page
A16	Resistivity Ratio versus 1000/T	A22
A17	Resistivity versus 1000/T	A23
A18	Mobility versus 1000/T	A24
A19	Mobility versus Temperature	A25
A20	Carrier Concentration versus 1000/T	A26
A21	Carrier Concentration versus 1000/T	A27
A22	Boron 3 Relative to the Growth Axis	A28
A23	Resistivity Ratio versus 1000/T	A31
A24	Resistivity versus 1000/T	A32
A25	Mobility versus 1000/T	A33
A26	Mobility versus Temperature	A34
A27	Carrier Concentration versus 1000/T	A35
A28	Carrier Concentration versus 1000/T	A36
A29	Boron 4 Relative to the Growth Axis	A37
A30	Resistivity Ratio versus 1000/T	A40
A31	Resistivity versus 1000/T	A41
A32	Mobility versus 1000/T	A42
A33	Mobility versus Temperature	A43
A34	Carrier Concentration versus 1000/T	A44
A35	Carrier Concentration versus 1000/T	A45
A36	Gallium 1 Relative to the Growth Axis	A46
A37	Resistivity Ratio versus 1000/T	A49
A38	Resistivity versus 1000/T	A50
A39	Mobility versus 1000/T	A51
A40	Mobility versus Temperature	A52

Figure		Page
A41	Carrier Concentration versus 1000/T	A53
A42	Carrier Concentration versus 1000/T	A54
A43	Gallium 2 Relative to the Growth Axis	A55
A44	Resistivity Ratio versus 1000/T	A58
A45	Resistivity versus 1000/T	A59
A46	Mobility versus 1000/T	A60
A47	Mobility versus Temperature	A61
A48	Carrier Concentration versus 1000/T	A62
A49	Carrier Concentration versus 1000/T	A63
A50	Undoped Relative to the Growth Axis	A64
A51	Resistivity Ratio versus 1000/T	A67
A52	Resistivity versus 1000/T	A68
A53	Mobility versus 1000/T	A69
A54	Mobility versus Temperature	A70
A55	Carrier Concentration versus 1000/T	A71
A56	Carrier Concentration versus 1000/T	A72
C1	Dektak Scan	C2
D1	Flow Chart	D2

List of Tables

Table		Page
I	Recommended Applied Voltage per Temperature Range	42
II	Data Record Sequence	43
III	Relative Error Versus Temperature	51
IV	Comparison of Results	69
V	Boron 1 run 1 Results	A2
VI	Boron 1 run 2 Results	A11
VII	Boron 2 Results	A20
VIII	Boron 3 Results	A29
IX	Boron 4 Results	A38
X	Gallium 1 Results	A47
XI	Gallium 2 Results	A56
XII	Undoped Results	A65

Abstract

Web-dendrite silicon was investigated to establish its potential value as a starting material for the fabrication of infrared detector arrays. The van der Pauw technique was used to measure the electrical transport properties of this material and assess its homogeneity. A total of eight samples were prepared from boron-doped, gallium-doped, and "undoped" web provided by the Westinghouse Electric Corporation. The samples were evaluated with respect to growth direction and position in the web.

The growth procedures of web silicon are discussed; including a description of the defects common to this material. The results are analyzed to determine uniformity, impurity concentrations, and the activation energy of the majority carriers. These particular web specimens are not suitable as candidates for device fabrication, due to the large numbers of dislocations/defects they were found to contain. It is not known whether the dislocations and defects observed are common to all dendritic-web materials.

I. Introduction

The purpose of this thesis is to investigate web-dendrite silicon as a potential material for the fabrication of infrared detector arrays. The next generation of infrared detectors will require material that is highly sensitive across the IR spectrum in addition to being extremely uniform over large areas. These requirements are forcing current growth techniques to be improved and may bring about the development of new crystal growth methods. Dendritic-web growth is a relatively new method of preparing long, thin single-crystal ribbons. This web ribbon is of interest to infrared detection development because it has the potential of yielding the larger area uniformity desired.

The desirability of having semiconductor material in sheet or ribbon form of proper thickness for device fabrication has been recognized for some time. It is one step that would reduce material handling. Excessive handling can adversely affect semiconductor material by introducing impurities and mechanical defects (Ref 3:1).

The boron-doped, gallium-doped, and "undoped" silicon samples tested were provided by the Westinghouse Electric Corporation in Pittsburgh, Pennsylvania. This study involved investigating web-dendrite silicon for homogeneity using the van der Pauw measurement technique over a wide temperature range (Ref 14:220-222). Samples were evaluated

both as a function of growth direction and location in the web. To accomplish this project electrical transport equipment in the Air Force Materials Laboratory was used to measure resistivity, carrier mobility, and carrier concentration as a function of temperature.

Samples of web-dendrite silicon were cut out from the web in a clover leaf pattern (see Fig. 22) to facilitate the van der Pauw measurement technique. This method allows for the uniformity in different directions along the material to be tested and compared, which is an advantage over the standard Hall bar approach. Samples were tested over a temperature range of 20 to 400 K. The results were then analyzed to determine the concentration of the donor and acceptor centers, and the activation energy of the carriers. Lastly, samples were etched to determine how free of dislocations they were.

Measuring electrical transport properties of semiconductor material requires special purpose equipment because extremely high resistance values are commonly encountered at low temperatures. To obtain resistivity, mobility, and carrier density data, the guarded Hall measurement system was used to avoid signal leakage paths (Ref 6:698). Current was measured with an electrometer ammeter operated in the feedback mode. The voltage measurements required for calculating resistivity were made with standard differential voltmeters via unity gain high-input electrometers, which were used as buffers to avoid sample loading. Data reduction

for analysis was then accomplished.

This thesis is divided into seven major parts: (1) Growth Procedure; (2) Defects in Web-Dendrite Silicon; (3) Theory; (4) Experimental System; (5) Data Acquisition and Analysis Techniques; (6) Results; (7) Conclusions.

II. Growth Procedure

The web-dendrite process is a crystal growth technique for producing long, thin ribbon crystals. Web-dendrite is grown by propagating, from a supercooled melt, two dendrites which originate from a single seed (Ref 10:2475). For proper growth the dendrite seed is placed in the exact thermal center of the liquid melt with the <111> direction tangent to the surface of the melt. The temperature of the melt is then adjusted to a "hold" temperature until the seed neither melts nor freezes (Ref 12:17). Growth is started by lowering the melt temperature several degrees so that the liquid surrounding the seed becomes supercooled. The dendrite seed then grows to form an ellipsoidal button with its major axis along the line of thermal symmetry of the melt (see Fig. 1).

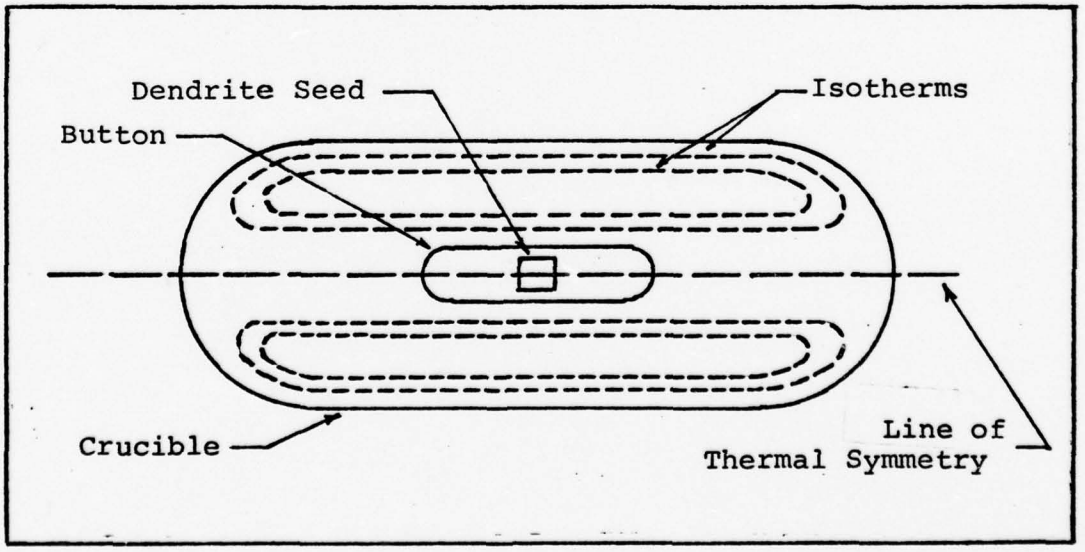

Figure 1 Idealized Growth Schematic

As the button grows, two bounding dendrites will form at the ends of the major axis of the button (see Fig. 2). When the distance between these bounding dendrites reaches a steady state, determined by the thermal conditions of the melt, the seed is pulled from the liquid silicon. As the dendrite seed is withdrawn, the needle-like bounding dendrites propagate down into the melt, growing just below the surface. The ribbon portion of the crystal forms, by the solidification of the liquid film, between the bounding dendrites. This is due to surface tension created as the seed is pulled from the melt. The process is illustrated in Figure 2.

The web freezes above the surface of the melt with the same crystalographic orientation as the dendrite seed. The mechanism by which the web forms is very similar to Czochralski growth (Ref 2).

Dendrites

To grow web-dendrite silicon by the twin plane re-entrant edge mechanism, the dendrite seed must be oriented in the proper position or web growth will not take place. "A re-entrant edge at a twin plane in the diamond-cubic lattice acts as a site of easy nucleation" (Ref 5:Q6). The dendrite seed may contain zero, one, or more twin planes. However, different crystal growth will result for each case.

To grow the button the dendrite seed must be oriented as shown in Figure 3. A seed, placed in a supercooled melt with the <2$\bar{1}\bar{1}$> direction normal to the surface, will grow

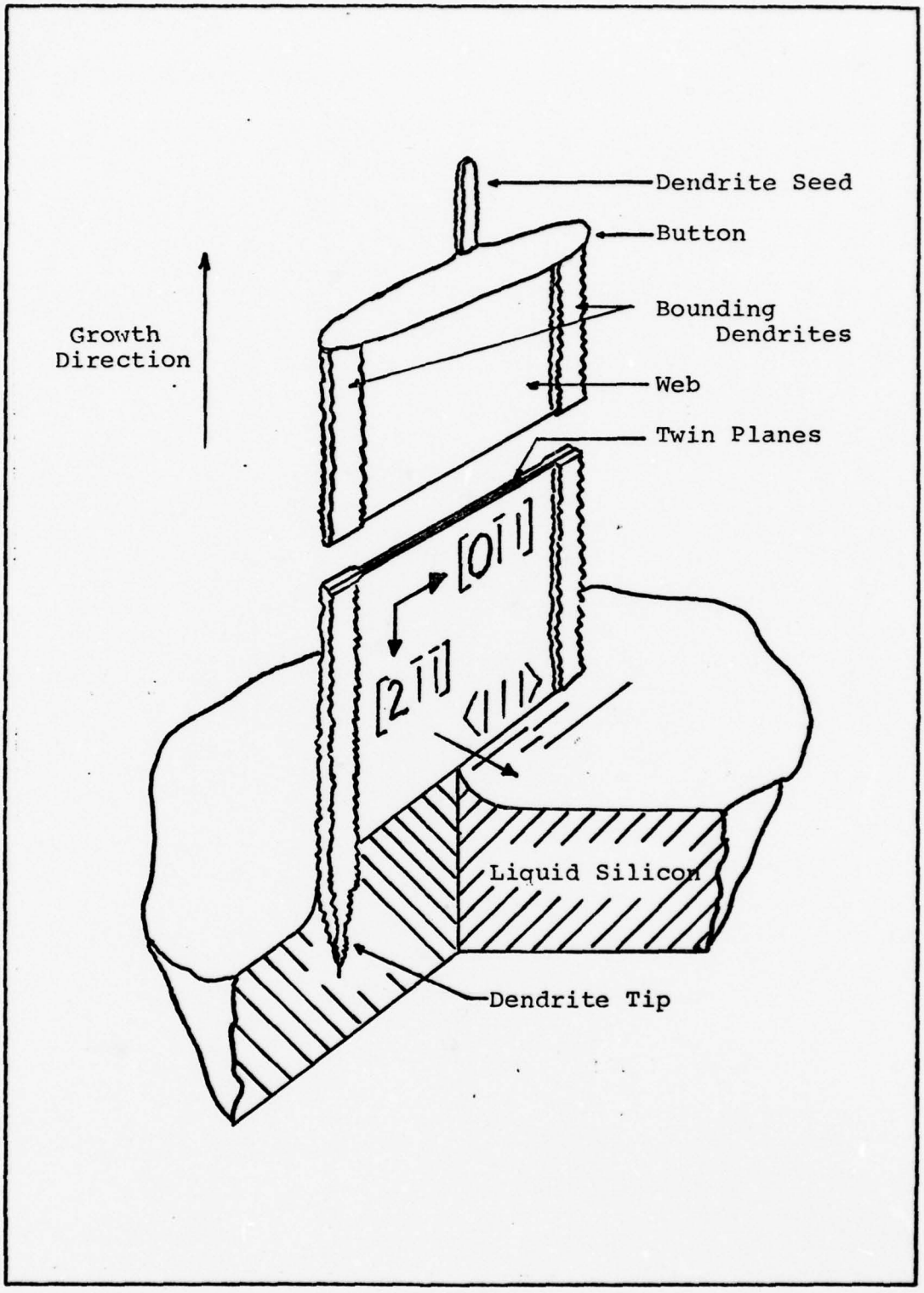

Figure 2 Schematic Section of Web Growth (Ref 12:17)

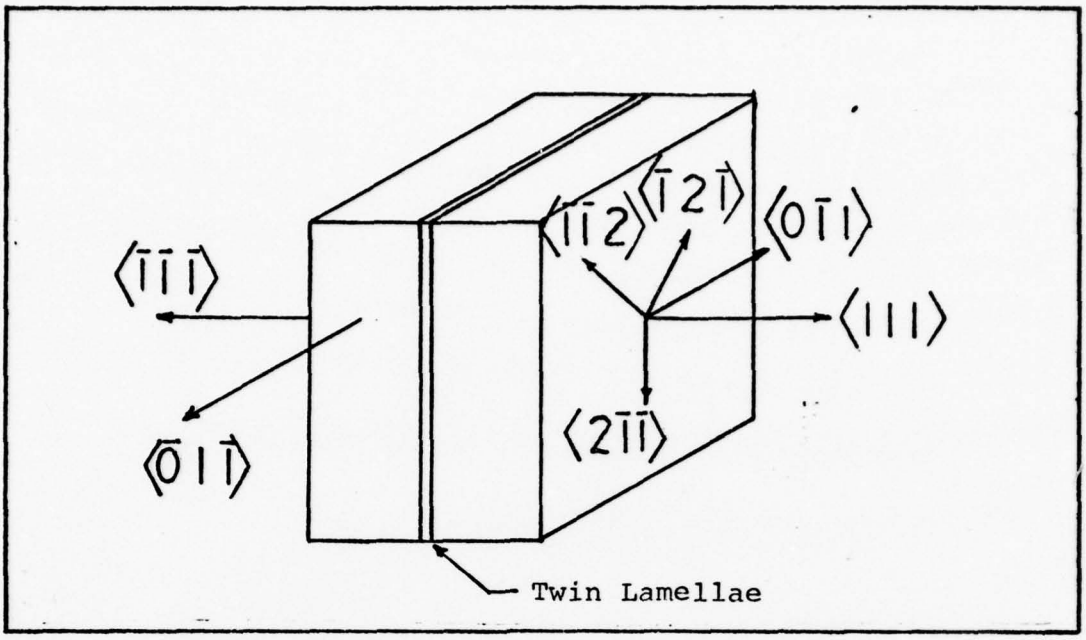

Figure 3 Orientation Relationship of a Diamond-Lattice Dendrite with Twin Lamellae (Ref 5:Q5)

in the form of a distorted octahedron. This octahedron, shown in Figure 4, is completely bound by [111] facets meeting at the ridges. Growth will not take place because there is no easy site for nucleation. In fact, on a [111] plane two dimensional nucleation is needed for further layer generation and growth (Ref 5:Q6).

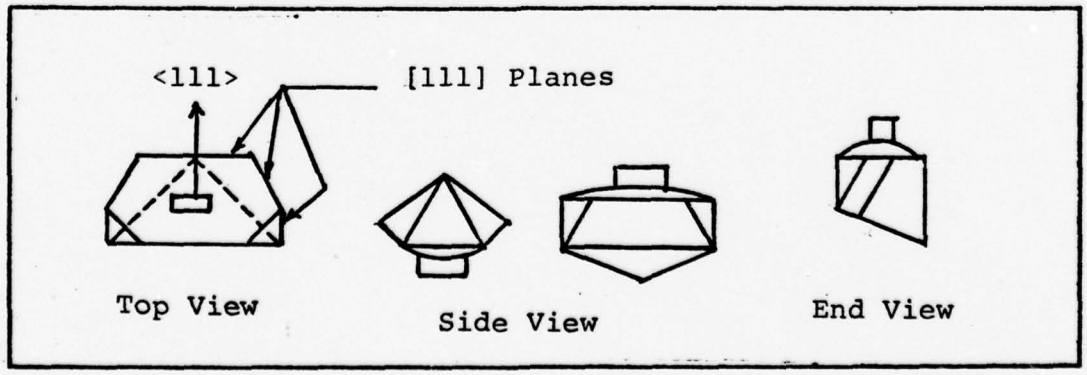

Figure 4 Single Crystal Oriented in <2$\bar{1}\bar{1}$> Direction

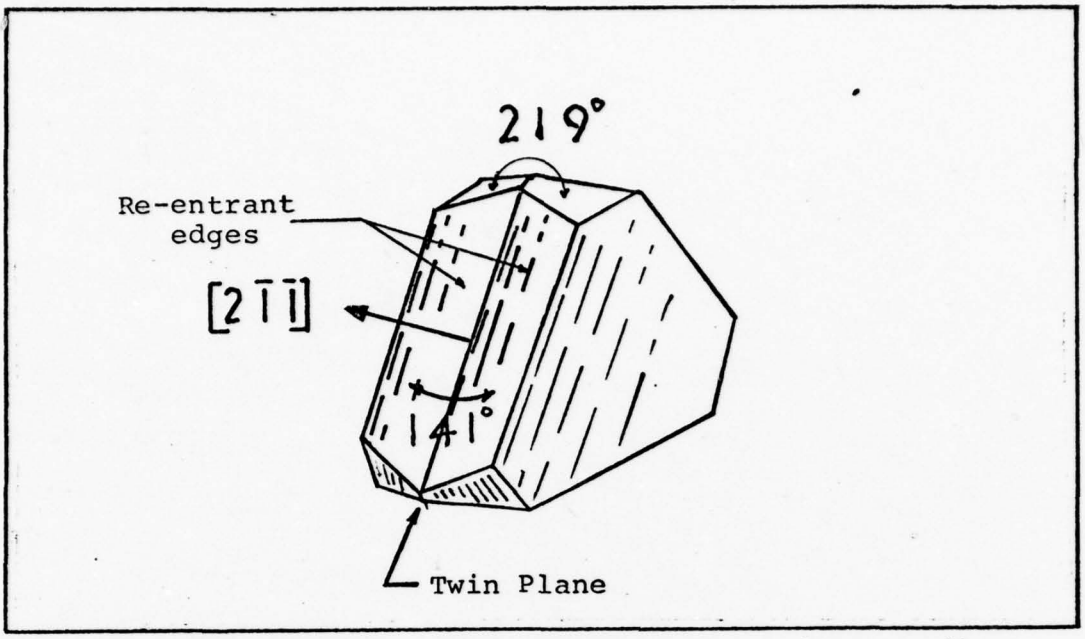

Figure 5 Dendrite with one Twin Plane (Ref 5:Q6)

If the dendrite seed contains one twin plane there are two possible growth directions; one called "favorable", the other called "unfavorable". Placing the dendrite seed into the melt with the $<2\bar{1}\bar{1}>$ direction normal to the melt's surface, a crystal will grow with a re-entrant edge (also called groove) as shown in Figure 5. This re-entrant edge is much more conducive to layer growth because the edges form a groove, which is an easy site of nucleation. However, when the seed is withdrawn from the melt, the re-entrant edges will grow out until the crystal is completely bounded by [111] facets; see Figure 6. Growth will stop because now two dimensional nucleation is required for further growth to occur (Ref 11:18).

If the seed is placed with the $<\bar{2}11>$ direction pointed into the melt the bounding dendrites will have a preferred

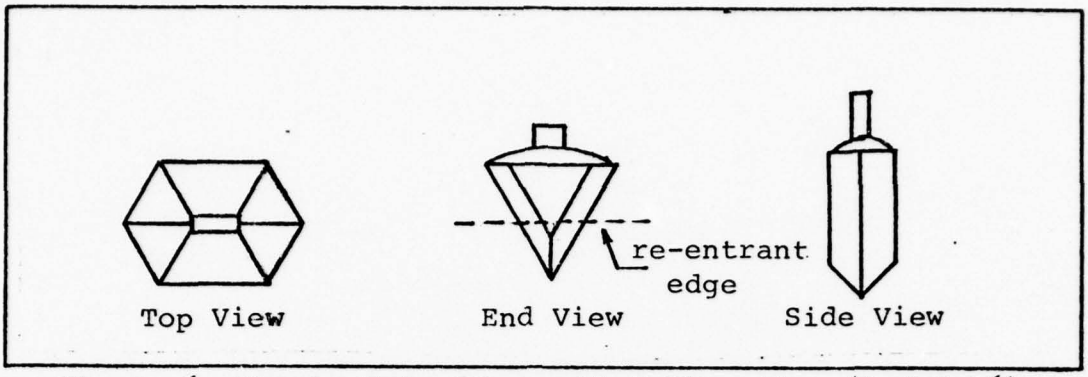

Figure 6 Single Twin "Favorable" Direction (Ref 5:Q6)

growth direction that is tangent to the surface of the melt (see Fig. 7). However, again growth will stop, as the seed is pulled from the melt, because [111] facets will completely bound the crystal. Therefore, it can be concluded that dendritic-web growth is not possible with zero or one twin plane (Ref 5:Q6).

If a seed contains two closely spaced twin planes, they form alternating re-entrant edges (141°) and re-entrant ridges (219°) at the twin plane boundaries (see Fig. 8). In this configuration the facets formed lead to the generation of self-perpetuating re-entrant ridges and grooves (Ref 12:18).

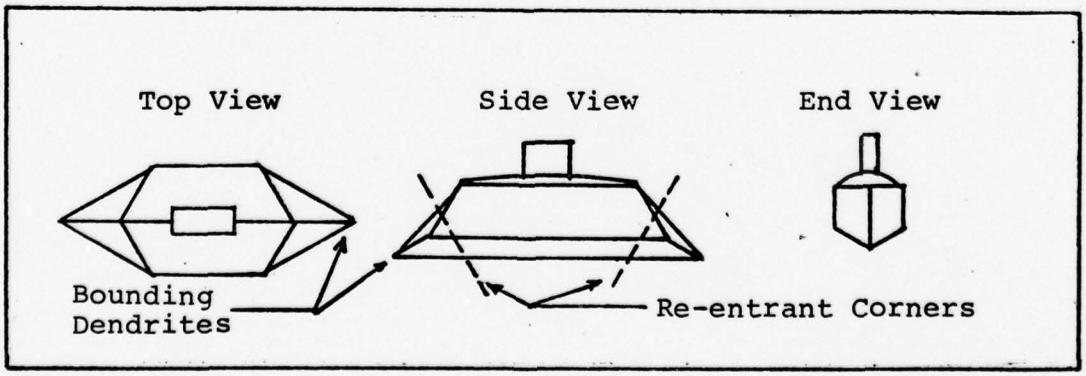

Figure 7 Single Twin "Unfavorable" Direction (Ref 5:Q6)

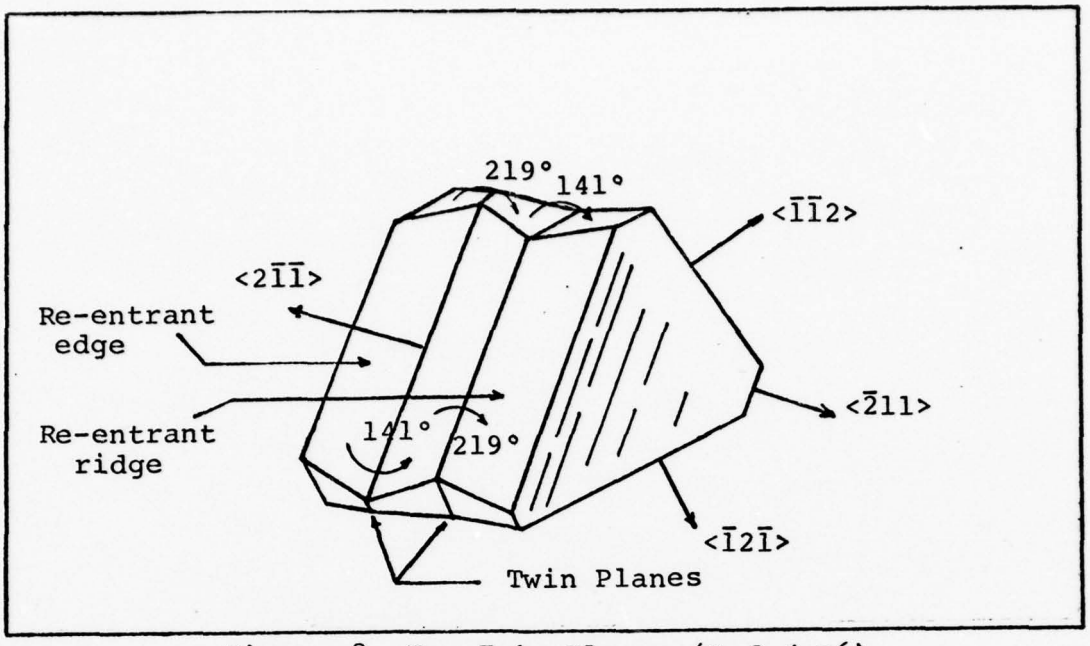

Figure 8 Two Twin Planes (Ref 5:Q6)

As this button is pulled from the melt; it can be seen from Figure 8 that all six <211> directions are equally probable for layer growth to start. All six <211> directions have one re-entrant edge and one re-entrant ridge; thus growth is not predictable. The bounding dendrites may grow straight down into the melt, as desired. Or, they may propagate out at 60° to a line normal to the surface of the melt. This also applies to dendrite seeds which contain any even number of twin Planes (Ref 5:Q6).

Ideally, web-dendrite silicon is grown from dendrite seeds having three or more oddly numbered twin planes. The re-entrant ridges (219°) and grooves (141°) still occur at the twin planes boundaries; see Figure 9 where the R's are ridges and the G's are grooves. As this button, shown in

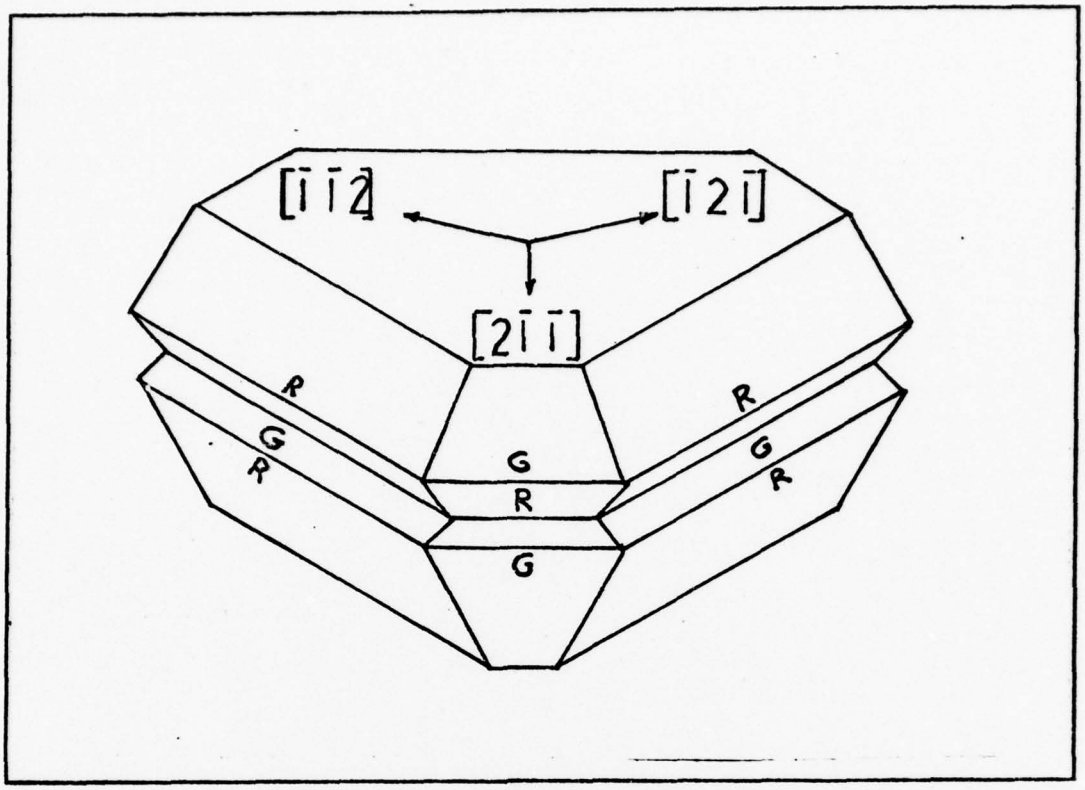

Figure 9 Three Twin Planes (Ref 5:Q6)

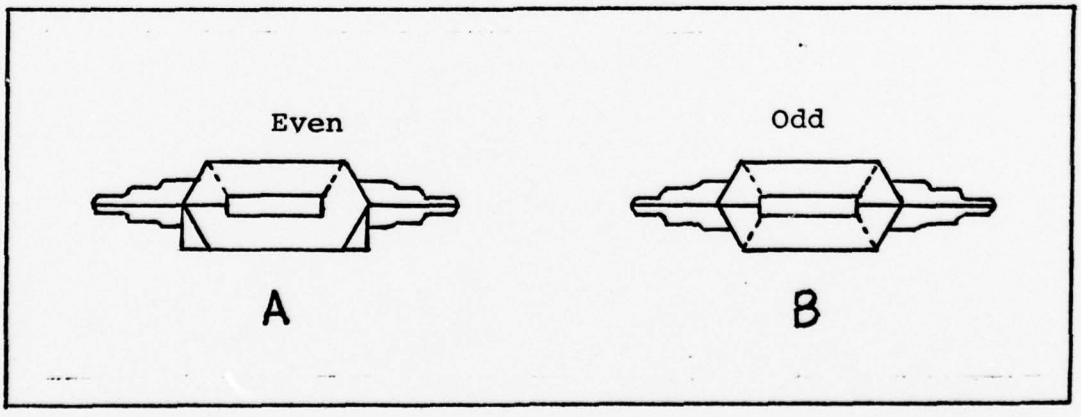

Figure 10 Even and Odd Numbered Twin Planes (Ref 5:Q6)

Figure 10b, is pulled from the liquid melt, a predictable growth will result, because not all six $<2\bar{1}\bar{1}>$ directions are equally favorable for the dendrites to propagate. As seen in Figure 9, three $<2\bar{1}\bar{1}>$ directions have one re-entrant ridge and two re-entrant grooves. The other three $<\bar{2}11>$ directions have one re-entrant groove and two re-entrant ridges. Web growth will only take place with the $<2\bar{1}\bar{1}>$ direction as shown in Figures 2 or 3, because re-entrant edges or grooves are easy sites of nucleation. Here, the bounding dendrites will propagate straight down into the melt. If the seed is placed in the melt with the $<\bar{2}11>$ direction pointing normal to the surface of the melt, the bounding dendrites will propagate out the $<2\bar{1}\bar{1}>$ corners at 60° to a line normal to the surface of the melt. In this configuration the web can not form (Ref 5:Q6).

The separation of the twin planes controls the tip curvature of the bounding dendrites, and once this distance is known, the overall growth of the dendrites can be analyzed in term of heat flow in the supercooled melt and in the dendrites themselves. Typically, the twin planes are separated by 1000 - 1000 Å (Ref 12:19).

Twin Planes in the Web

As discussed previously, in diamond lattice structures at least two twin planes are necessary for re-entrant edge growth to occur. However, twin planes are not necessary for the solidification of the web between the bounding

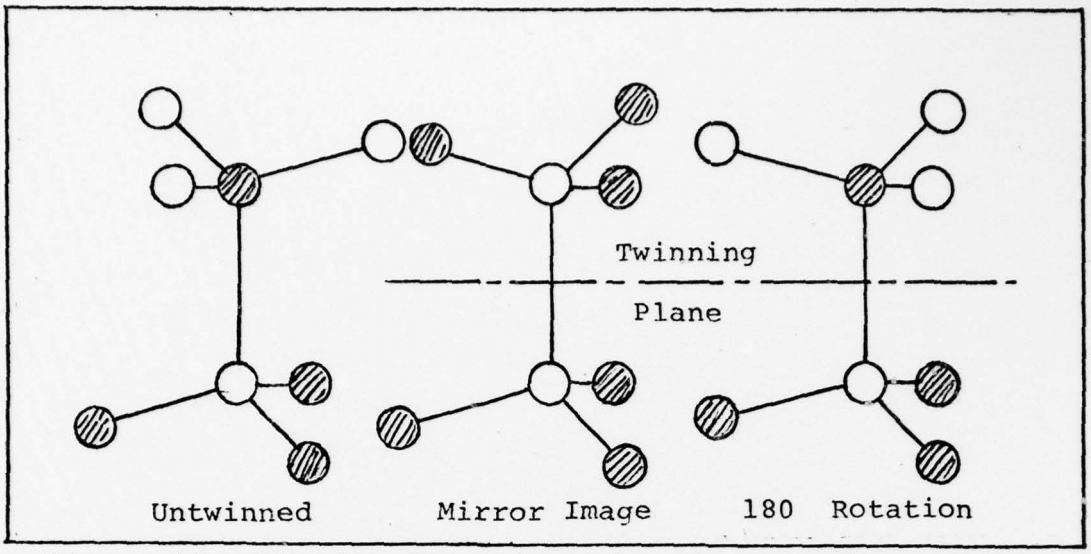

Figure 11 Twinning Operations for Diamond-Like Lattices

dendrites (Ref 10:2475). The twinning operation for diamond-like lattices is shown in Figure 11. Twin planes in silicon parallel to the [111] plane are very coherent and may either be classified as mirror image or 180° rotation twins (Ref 5:Q1). A twin boundary is called coherent when the twin plane and boundary plane are identical (Ref 8:149).

Ideally the seed is pulled from the melt as shown in Figure 12, for then the twin plane structure will be

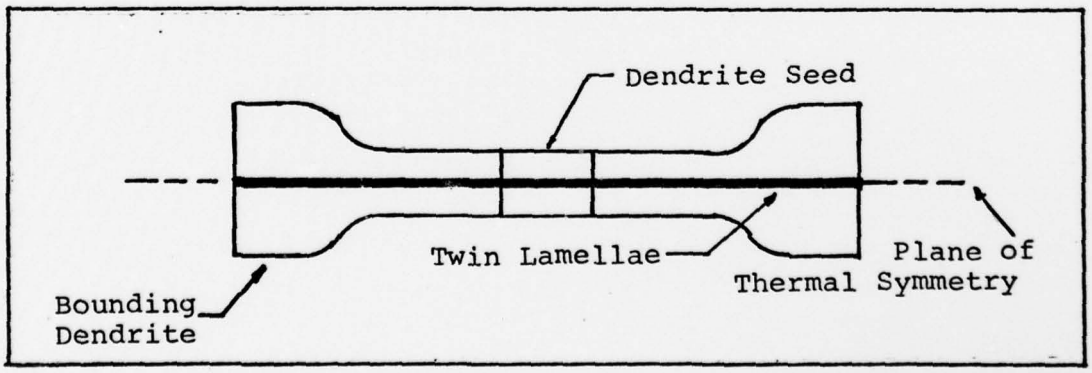

Figure 12 Symmetrical Twin Lamellae (Ref 3:3)

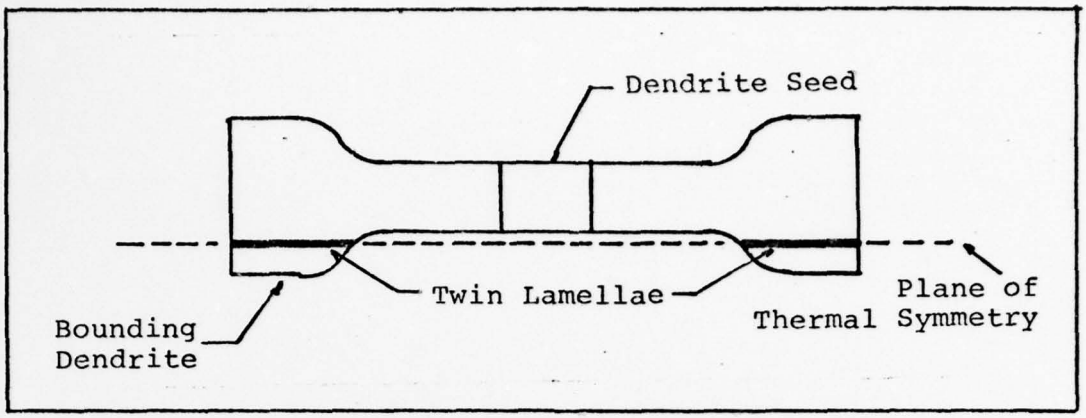

Figure 13 Web without any Twin Lamellae (Ref 3:3)

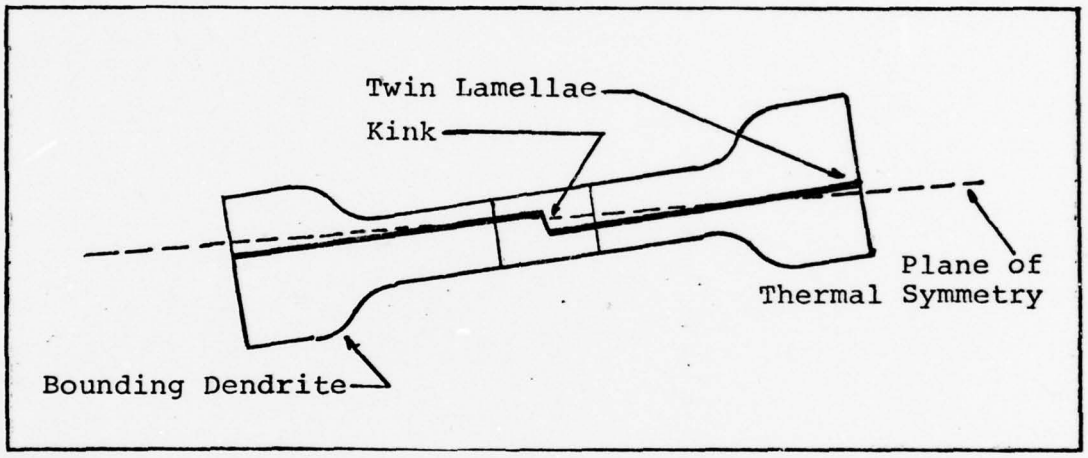

Figure 14 Web with a Secondary Twin Lamellae (Ref 3:3)

continuous across the entire web. If the seed is not aligned with the line of thermal symmetry, either no twin lamellae may be present or the twin structure may propagate with a mismatch or kink; see Figures 13 and 14 respectively (Ref 3:3).

In Figure 14, the kink in the twin lamellae is called a secondary twin. Secondary twins form perpendicular to the [111] planes and are a source of dislocations (Ref 2). When the web is not superimposed on the plane of thermal

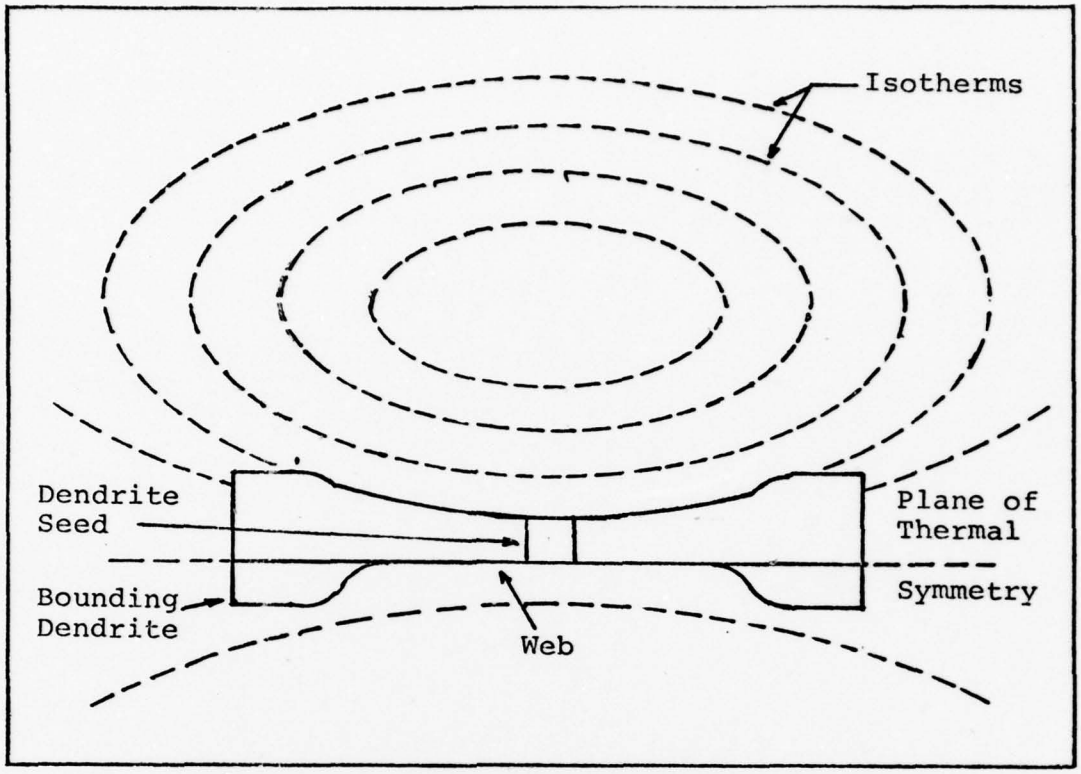

Figure 15 Web-Dendrite Schematic

symmetry of the melt, the web will be thicker near the bounding dendrites (see App. C); and dislocation or slip may occur.

When growth conditions are not proper, often several dendrites will grow from the button, and web will solidify between each of them when the seed is pulled from the melt. However, by controlling pull rate, seed position, and thermal conditions silicon web crystals can be grown with one or possibly two very flat surfaces. The flatter surface will be the one nearest the plane of thermal symmetry of the melt. The other surface, slightly concave due to misalignment, will coincide with the isotherms in the crucible; see Figure 15. Ideally, if the web is located exactly centered along the plane of thermal symmetry (see Fig. 1) the twin lamellae

will form centered in the web. This web will show equal flatness on both sides (Ref 5:Q4).

Another problem inherent to dendritic-web growth is caused by supercooling in the melt. Since supercooling must be achieved, the walls of the crucible can act as sites of nucleation. This extraneous nucleation caused by the walls' lower temperature, proceeds inward towards the seed and stops the growth of the material being pulled from the melt. Because silicon has such a high melting point (1414°C), no crucible material is known that will supress this undesired growth. It is possible to reduce the occurrence of this problem by controlling the thermal symmetry of the melt such that the silicon near the walls is kept at a temperature greater than its melting point while the center region remains supercooled (Ref 3:2).

III. Defects in Web-Dendrite Silicon

Most defects in web-dendrite silicon can be classified as dislocations, linage, or twins. Each has an effect on the electrical transport properties of the material.

Dislocations

The majority of dislocations in web material occur as a result of the entrapment of liquid in the dendrite region. Upon freezing, stress resulting from this entrapment, is relieved by the generation of dislocations. If proper precautions are not taken these dislocations can propagate into the web region. The two most common dislocations found in web silicon are edge dislocations and screw dislocations.

Edge Dislocations. Dislocations that occur on the surface of the web result in compression and dilation points in the lattice; these are called edge dislocations. Figure 16 shows the lattice deformation resulting in a compression region "C" just above a dangling bond, and a dilation region "D" below the free bond (Ref 8:83).

Surface dislocations are measured as a number per unit area. Material having a dislocation density of greater than $10^3/cm^2$ is not considered detector grade (Ref 2). Edge dislocations affect the electrical transport properties of semiconductors in two ways. First, an energy level will

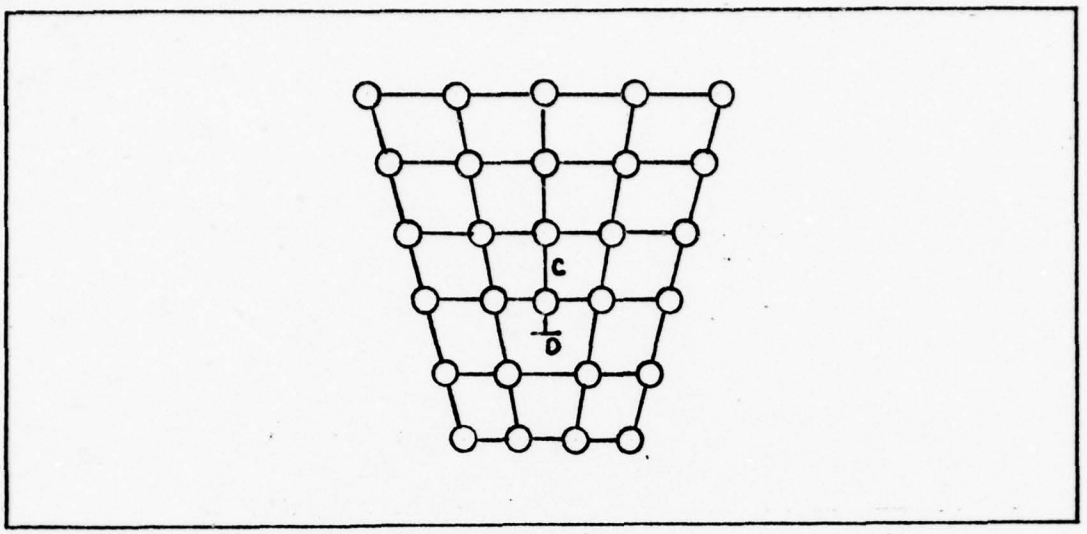

Figure 16 Compression and Dilation Region at an Edge Dislocation Site (Ref 8:83)

form in the forbidden gap; second, a space charge domain will form surrounding the dislocation. If a line of closely spaced dislocations exists a space-charge pipe will form through the material. It is known that applied electric fields have different effects across a line of dislocations than parallel to them (Ref 8:157-162).

Screw Dislocations. Slips known as screw dislocations occur when the growth in one part of the crystal is faster than that in another part. What results is shown in Figure 17. The difference between screw dislocations and edge dislocations is that the screw dislocation step leads to a smoothing of the deformity in the lattice; and no dangling bonds are formed. The electronic disturbances due to ideal screw dislocations are very minor (Ref 8:94-96).

However, screw dislocations do not generally lie in a single plane parellel to the slip vector, as shown in

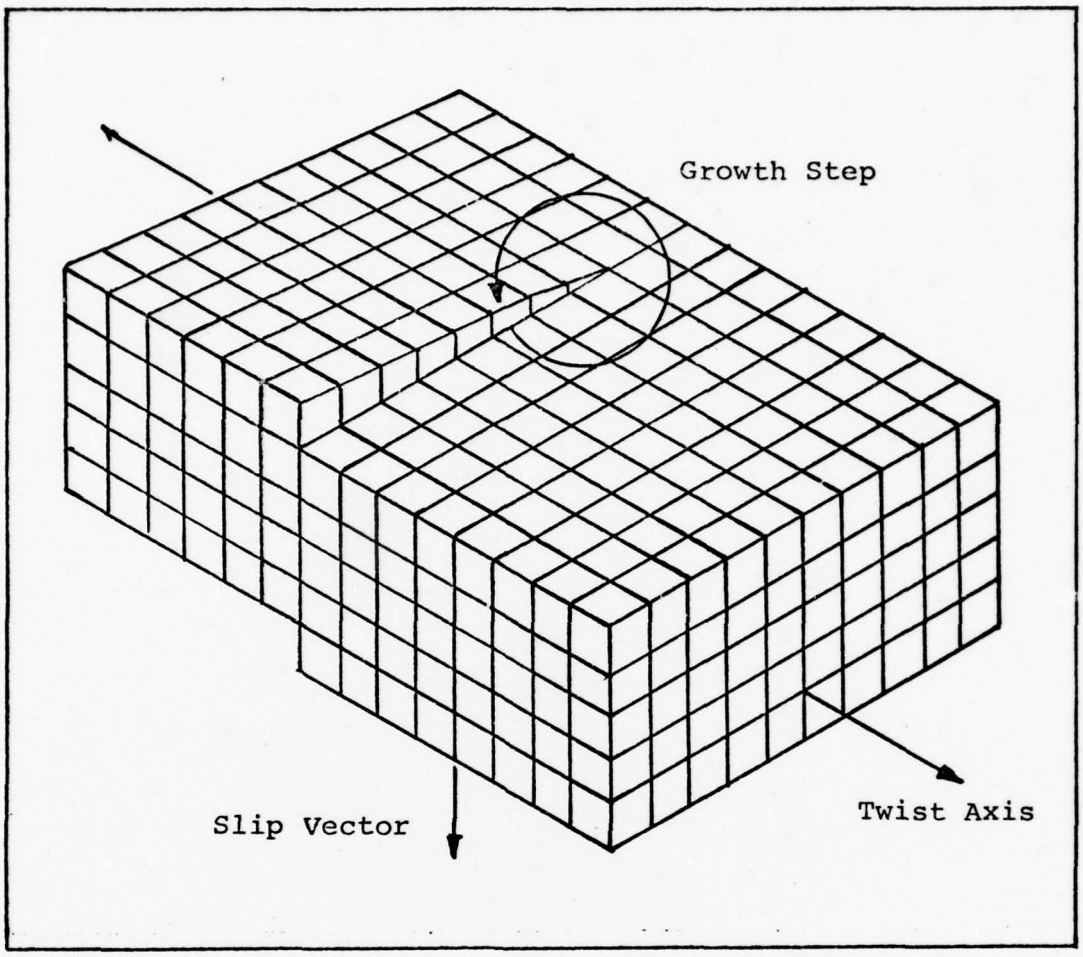

Figure 17 Spiral Ramp of a Screw Dislocation (Ref 8:95)

Figure 17. They normally form bend dislocations, that ultimately result in edge dislocations. This is because slips occur preferentially on densely packed crystallographic planes, and the growth of a screw dislocation, resulting from an uneven growth rate, is subject to forces that tend to divert slip planes into lower-energy positions; thereby creating edge dislocations. It has been shown experimentally that screw dislocations show electronic behavior similar to edge dislocations (Ref 8:154-156).

Linage

The word linage has been used to define or describe many different kinds of defects occurring in crystal growth. But since today's crystals are grown in a rather controlled manner, defects can be defined and recognized quite clearly. With this in mind, Matare defines linage as the occurrence of low-angle grain boundaries due to very small overlap of dilation and compression zones. Grain boundaries are lines of defects that may follow straight lines; but generally they follow curved pathways, appear in groups, or may disappear at some point without any apparent reason (Ref 8:91).

Matare also reserved linage to mean grain boundaries angles of less than 1°. Boundaries originating from grains with angles greater than one degree are classified as low or medium-angle boundaries.

Low angle grain boundaries ($\theta \leq$ a few degrees) have been studied extensively in semiconductors, to reveal their effect in devices. Experimentally it has been shown that low angle boundaries generate electronic properties undesirable to semiconductor devices. Grain boundaries produce an increase in potential at the site of a dislocation. Additionally they create line charges that are regions of high conductivity. Thus, the electronic transport properties will not be desirable for materials with this type of defect (Ref 8:92-93, 167).

Twinning

Twins, discussed briefly above, have a more complicated pattern than the ideal twin shown in Figure 11. Movement of an atomic layer, which produces a twin is similar to that which produce a slip. Twins differ from slips, in that ideally no bonds are broken.

Observing the ridges and grooves of twin lamellae, as shown in Figure 9, it can be surmised that strain energy stored along a twin can produce changes in the electronic band structure. However, in the case of undisturbed twins no electrical effects have been observed, not even in life-time measurements of minority change carriers. This most sensitive electronic characteristic is almost independent of twins in the path of carriers if no doping gradients exist (Ref 8:97).

Twin plane defects can occur which greatly affect the electrical properties of a crystal. Twin planes may glide across one another creating higher energy areas or zones within the crystal. Dangling bonds caused by gliding twins attract conduction electrons and form space-charge layers (Ref 8:148).

Another problem due to twin planes can result when the twinning angle reaches a high value causing nearest neighbor distances to change. A hypothetical twin plane in a cubic lattice is shown in Figure 18. The change in nearest neighbor distance results in changes in the electronic band

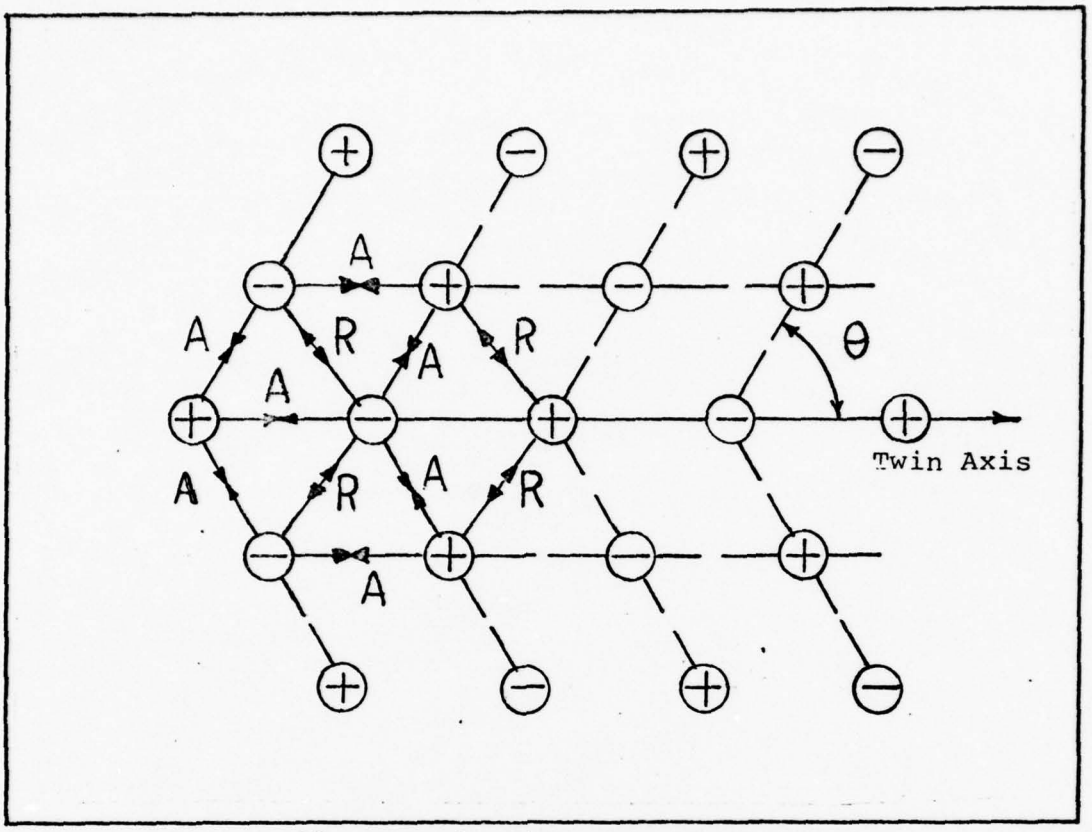

Figure 18 Twin in a Hypothetical Lattice
R = Repulsive Force, A = Attractive Force, $\theta \leq 45°$ (Ref 8:78)

structure due to higher repulsive forces and lattice strain (Ref 8:79).

Noncoherent and Secondary Twins. Up to this point the defects associated with twins have been considered only for coherent twin planes. A large class of twin lamellae defects, which create impurity gradients, are noncoherent twins, in which the twin plane and the boundary plane are not identical (Ref 8:149). These cause nearest-neighbor distance changes, which result from the strain that is absorbed in a twin lamellae when freezing takes place (Ref 8:149-150).

Noncoherent twin boundaries are areas where structure sensitive parameters like mobility and lifetimes are affected. A reliable, reproducible device should not use material known to have these defects. The reason for this lies in the effect it will have on a device under bias conditions. The resistivity and photovoltage measured experimentally across a noncoherent twin reveals a maximum due to the impurity gradient present. This situation is most common in silicon for the [111]-growth direction (Ref 8:150-151).

Secondary twins, which form normal to the [111] twin lamellae, show interatomic bond deformations rather than dangling or broken bonds. Secondary twins are generally formed where there is a discontinuity in the twin lamellae. Knowing that secondary twins are present will eliminate a material for device fabrication. It was found that these regions are photoelectrically active (Ref 8:100).

From the preceding discussion, it can be concluded that defects play an important part in the electrical transport properties of semiconductors. Moreover, defects can completely rule out a potential material for device fabrication.

IV. Theory

The first part of this section will explain the derivation of the change balance equation with respect to temperature for p-type semiconductors. Second is the development of the equations needed to calculate resistivity, carrier mobility, and carrier concentration from the van der Pauw measurement technique.

Charge Balance Equation

The position of the Fermi energy levels are shown in Figure 19. This is an energy level diagram for semiconductor material doped with an acceptor impurity only.

It is shown in M^{c}Kelvey, et al. that the concentration of conduction holes depends only on the position of the

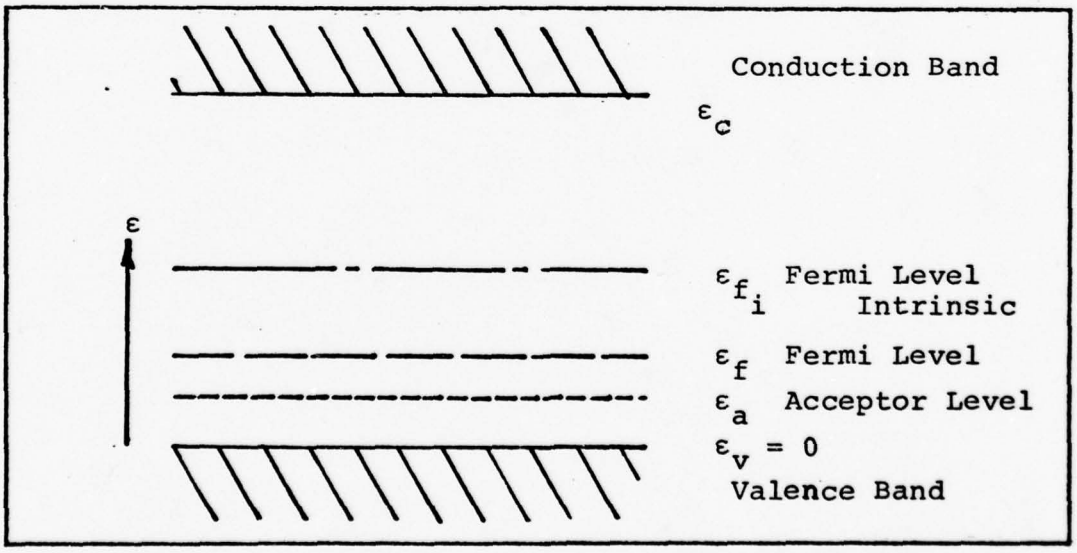

Figure 19 Relative Position of Energy Levels in p-type Semiconductors

Fermi energy level and the form of the bands (Ref 9:266). Following this concept the concentration of conduction holes, p in cm^{-3} can be calculated from:

$$p = N_F \exp(-\epsilon_f/kT) \tag{1}$$

$$N_F = \frac{2(2\pi m_h^* kT)^{3/2}}{h^3} \tag{2}$$

where

ϵ_f is the Fermi energy level (ev)

k is Boltzmann's constant (ev/ K)

T is temperature (K)

m_h^* is the effective mass for holes (g)

h is Planck's constant (erg-sec)

ϵ_v, the energy level of the valence band, normally in the exponent of equation (1), is set equal to zero as a reference.

In both the extrinsic and intrinsic cases the carrier concentration in the bands is determined by equation (1). In the intrinsic case the Fermi energy level is located half way between the conduction and valence bands at T = 0 K. In the extrinsic case the impurity center determines the position of the Fermi energy level (Ref 11:122). Therefore, to determine the carrier concentration a relation between the Fermi energy level and the impurity level must be known.

The probability that an energy level is occupied is given by the Fermi-Dirac function:

$$f(\epsilon) = \frac{1}{1 + \exp\left[(\epsilon - \epsilon_f / kT\right]} \tag{3}$$

where

ϵ is the energy at some level

$f(\epsilon)$ is the probability of occupation

However, since complex levels are associated with any impurity level, equation (3) is only valid if the probability of a level ϵ being occupied is independent of the occupation of neighboring levels (Ref 11:123).

Following Putley's derivation, equation (3) is valid if ϵ_a is written for ϵ where

$$\epsilon_a = kT \ln \left[\sum_i g_i \exp\left(-\epsilon_i / kT\right)\right] \tag{4}$$

where

ϵ_i is the energy of the i-th level

ϵ_1 is the ground state

g_i is the degeneracy of the i-th level

For the hydrogenic model $g_1 = 2$ and the relative values of ϵ_1 and ϵ_2 are such that ϵ_2 and higher levels can be neglected. Thus the impurity centers are considered to occupy the energy

of their lowest level. Equation (4) can then be substituted into equation (3) to give:

$$f(\epsilon_1) = \frac{1}{1 + \frac{1}{4} \exp\left[\frac{(\epsilon_f - \epsilon_1)}{kT}\right]} \tag{5}$$

The extra factor of $\frac{1}{2}$ in the demoninator comes into play due to the fact that the acceptor level for silicon is doubly degenerate. ϵ_1 can now be identified with the energy level indicated in Figure 19 for the position of the impurity level (Ref 11:123).

Given the probability of an acceptor center being occupied, the distribution of holes between the valence band and the impurity level can be calculated. At absolute zero the acceptor impurity centers, N_a, will contain N holes. These holes are available for conduction, when they are excited into the valence band as temperature is increased. Therefore, the number, p, of holes in the valence band is given by equation (1), and the number of conduction holes remaining in the acceptor center can be found by multiplying the right-hand-side of equation (5) by N_a (Ref 11:124). Adding these expressions yields a relation for the total number of holes available for conduction:

$$N = \frac{N_A}{1 + \frac{1}{4} \exp\left[\frac{(\epsilon_f - \epsilon_a)}{kT}\right]} + p \tag{6}$$

Substituting equation (1) into equation (6) to eliminate the Fermi energy level ϵ_f, an expression for the carrier concentration as a function, dependent only on temperature, results.

$$\frac{p\,(N_a - N + p)}{(N + p)} = \tfrac{1}{4}\, N_F \exp\,(-\epsilon_a/kT) \qquad (7)$$

In equation (7), N may have a maximum value of N_a conductors; this would be the case if the material contained acceptor impurities only. But, because it is very difficult to prepare material containing only one type of impurity; there will normally be, in p-type material, a donor level present such that $N_a > N_d$. At absolute zero the N_d donor centers will be occupied or neutralized by holes from the acceptor centers. Therefore, at temperatures sufficient to excite holes from the acceptor level to the valence band the actual number of holes available for conduction is:

$$N = N_A - N_D \qquad (8)$$

Material of this type is considered as "compensated" since the available number of conduction holes is less than the number of p-type impurity centers (Ref 11:125).

High and Low Temperature Characteristics. At low temperatures where $N_a >> p$, equation (7) reduces to:

$$p = \left(\frac{N}{N_2 - N} \right) \frac{N_F}{4} \exp\left(-\epsilon_a / kT\right) \qquad (9)$$

Taking the natural logarithm of both sides yields:

$$\ln p = \ln \left[\frac{.25\, N}{N_a - N} \right] + \ln N_F - \epsilon_a / kT \qquad (10)$$

From this equation the activation energy, ϵ_a, can be determined by differentiating $\log p$ with respect to $1/T$.

$$\Delta \left[\ln \left(\frac{P}{T^{3/2}} \right) \right] = \frac{-\epsilon_a}{k} \Delta \left(\frac{1}{T} \right) \qquad (11)$$

Remembering that $T^{3/2}$ comes from the term containing N_F.

At high temperatures such that $kT >> \epsilon_a$ equation (7) reduces to:

$$p = N_a - N_d \qquad (12)$$

From the low and high temperature results a theoretical logarithmic plot of carrier concentration against $1/T$ can be constructed. This curve is shown in the analysis part of section VI.

Resistivity and Mobility

The theory behind the van der Pauw technique for determining resistivity of a material is based on the theorem which applies to a uniformly flat sample of arbitrary shape, if the contacts are sufficiently small and are located near the edge of the sample (Ref 13). The results of this theorem will be used to derive the equations necessary for calculating resistivity, mobility, and carrier concentration.

A flat sample, free of holes, is cut in the pattern shown in Figure 20. Four contacts are made at the corners of the sample at points A, B, C, and D. Applying a current between contacts A and B, the potential voltage difference $V_c - V_d$ can be measured to define resistance R_1:

$$R_1 = \frac{V_c - V_d}{I_{ab}} \tag{13}$$

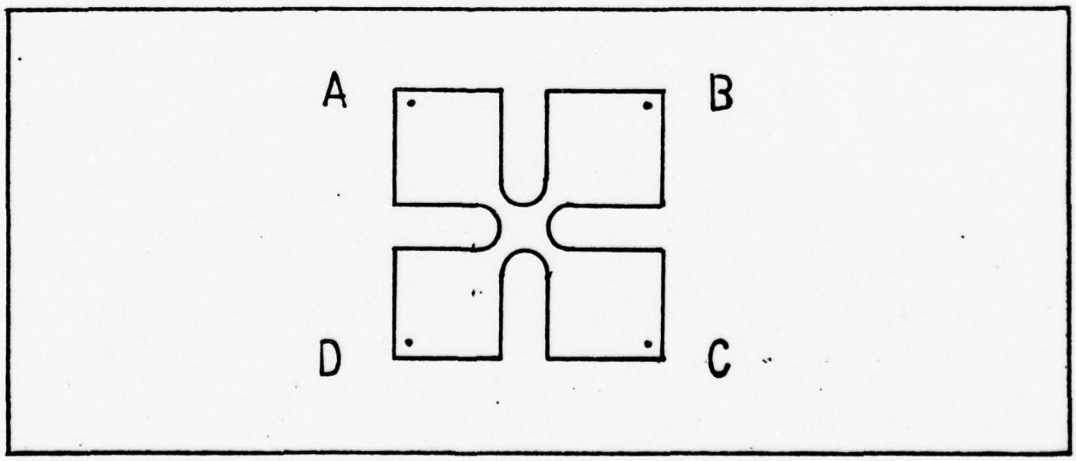

Figure 20 van der Pauw Sample

analogously

$$R_2 = \frac{V_b - V_c}{I_{ad}} \tag{14}$$

From these two resistances, measured perpendicular to one another, there exists the relationship derived in van der Pauw's paper:

$$\exp\left(\frac{-\pi t\, R_1}{\rho}\right) + \exp\left(\frac{-\pi t\, R_2}{\rho}\right) = 1 \tag{15}$$

where

t is the thickness of the sample

ρ is the resistivity of the material

In order to facilitate the calculation of ρ, equation (15) is rewritten in the form:

$$\rho = \frac{\pi\, t}{\ln 2}\left(\frac{R_1 + R_2}{2}\right) f\left(\frac{R_2}{R_1}\right) \tag{16}$$

Where, $f(R_2/R_1)$ is a function of the ratio R_2/R_1 and it satisfies the relationship:

$$\frac{R_2 - R_1}{R_2 + R_1} = \cosh^{-1}\left[\frac{\exp(\ln 2/f)}{2}\right] \tag{17}$$

A graph of equation (17) is shown in Reference 14, page 221. However, an approximate value for f can be used when R_2 and R_1 are nearly equal.

$$f(R_2/R_1) = 1 - \left(\frac{R_2 - R_1}{R_2 + R_1} \right)^2 \frac{\ln 2}{2} - \left(\frac{R_2 - R_1}{R_2 + R_1} \right)^4 \left[\frac{(\ln 2)^2}{4} - \frac{\ln 2}{12} \right] \tag{18}$$

Therefore, to determine ρ the ratio R_2/R_1 must be calculated first. The proof that these relationships apply to a lamella of any shape is derived from conformal mapping of the arbitrary sample shape.

The Hall mobility can be determined by measuring the change in resistance (ΔR_e) when a magnetic field is applied perpendicular to the sample. Using Figure 21 ΔR_e can be calculated as shown in equation (19).

$$\Delta R_e = \left| \frac{V_a - V_c}{I_{bd}} - \frac{V_a(\bar{B}) - V_c(\bar{B})}{I_{bd}} \right| \tag{19}$$

Where $V_a(\bar{B})$ is the measured voltage with an apply $\bar{B}$ field. The Hall mobility is then calculated from equation (20).

$$\mu = 10^8 \, (\Delta R_e t / B\rho) \tag{20}$$

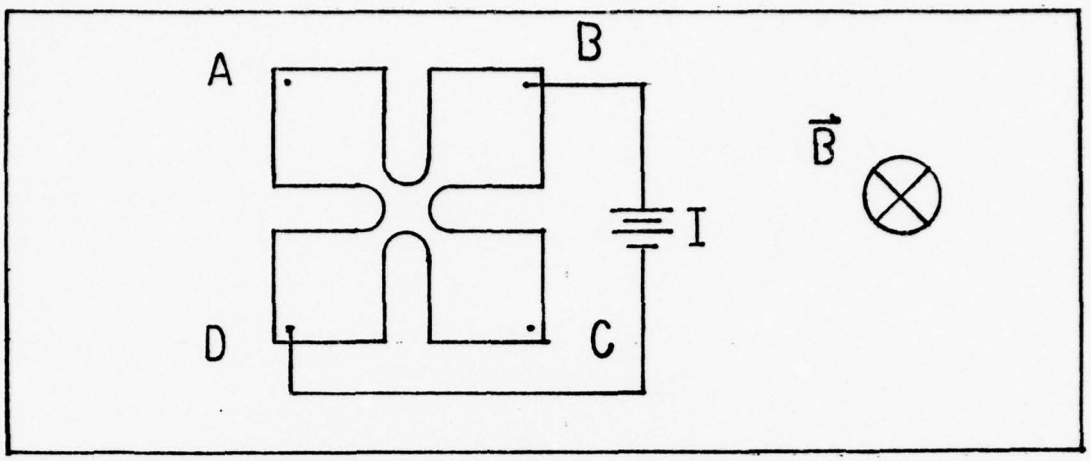

Figure 21 Hall Mobility Measurement

where

t is the sample's thickness (cm)

B is the magnetic field (gauss)

ρ is the resistivity (ohm-cm)

This will yield μ in units of cm^2/volt-sec (Ref 6:699).

The carrier density in cm^{-3} can then be calculated from:

$$p = (\rho e \mu)^{-1} \tag{21}$$

where

$e = 1.602 \times 10^{-19}$ coul

V. Experimental System

This section discusses the over all equipment system used in this project.

Sample

All samples came with the bounding dendrites intact so that X-ray diffraction patterns were not necessary for determining the growth direction (see Fig. 2). All samples were cut out from the web with an ultrasonic cutter to the dimensions and shape shown in Figure 22.

The samples were sparked with an element of a shallower acceptor level to provide a base for gold wire contacts to be made. The procedure was developed by personnel at the Air Force Materials Laboratory and is explained in Reference 4. The contacts, considered good down to 18 K, should be as ohmic as possible. The means the current is proportional

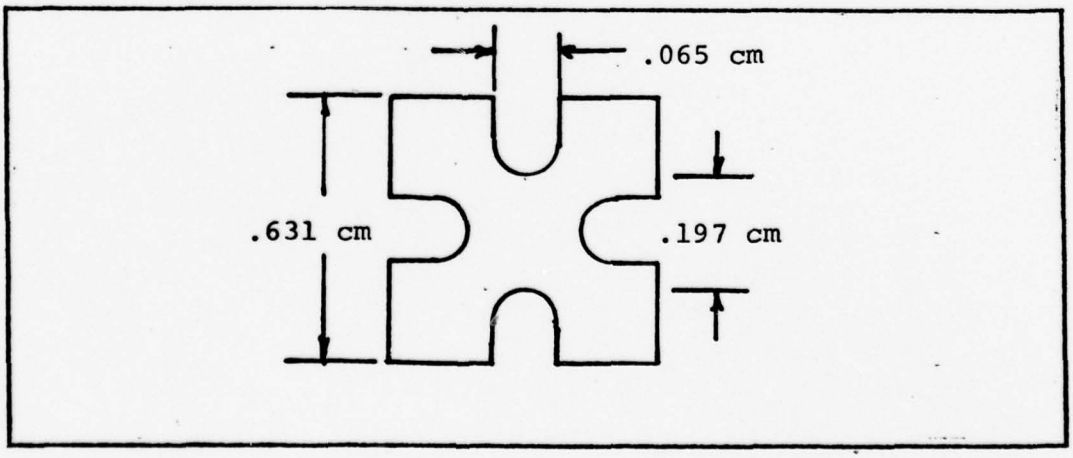

Figure 22 Sample Dimensions

to the voltage, applied across the contacts, in both bias directions.

Three basic ways ohmic contacts can be formed to semiconductor material are: first, by contacting with a metal of the proper work function so that the Schottky barrier is small for the thermally excited current; second, with contacts made by heavily doping the semiconductor material near the junction so that a current can be carried by quantum mechanical tunneling through the barrier; and third, ohmic contacts can be made by creating recombination centers in the interface region on the semiconductor side of the junction. Of these three approaches doping of high concentrations in order to produce tunneling is the most noted technique. Tunneling contacts are more reliably reproduced and generally remain ohmic over a wide temperature range (Ref 4:703).

van der Pauw System

The schematic diagram for the van der Pauw system is shown in Figure 23. The unity gain electrometers drive the shields to the same potential as their respective inner conductors. This technique, called the guarded Hall method, permits the use of standard laboratory differential voltmeters. The unity gain outputs reduce the leakage of signal currents and the system's time response, by nearly eliminating stray capacitance in the leads (Ref 1:24). This circuitry provides for the measurement of extremely high

resistances to be made. Current is measured by an electrometer ammeter operated in the feedback mode, which drives the input to ground.

The six different switch positions shown in Figure 24, allow for the following measurement to be made. Data

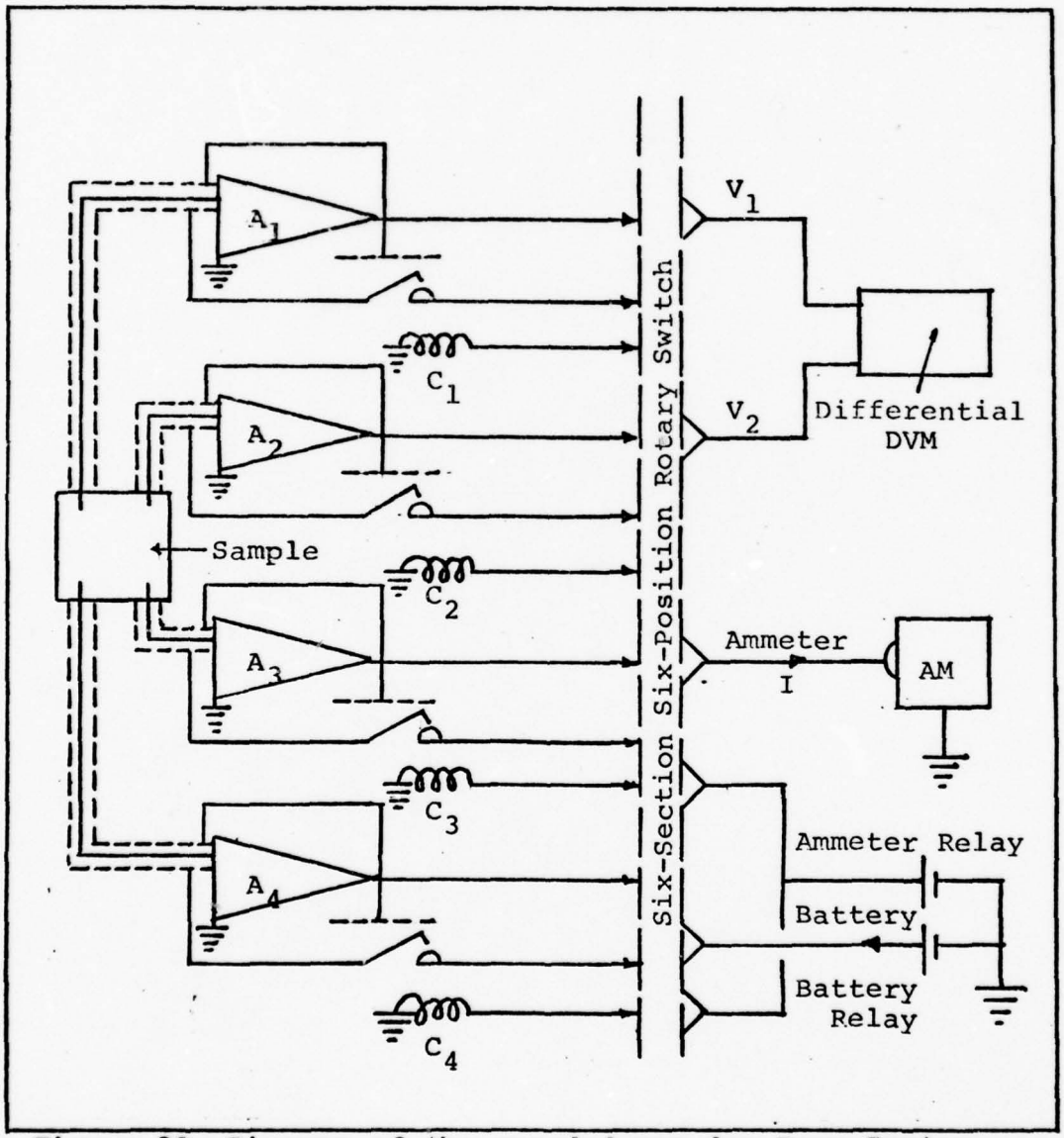

Figure 23 Diagram of the guarded van der Pauw System. A_1-A_4 unity gain amplifiers, AM ammeter, C_1-C_4 coils that activate the corresponding reed relays (Ref 6:699)

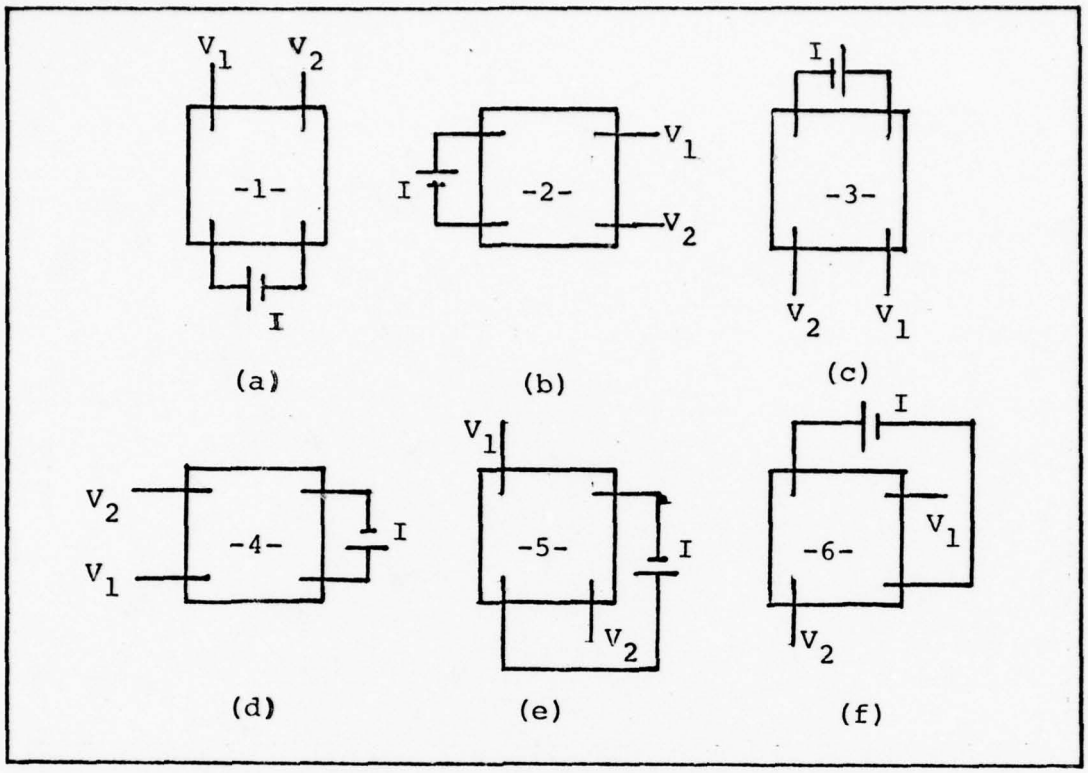

Figure 24 Sample Connection for taking van der Pauw Transport Data (Ref 6:698)

collected from switch positions 1 through 4 is needed to calculate R_1 and R_2, and thence resistivity. The Hall voltage needed to calculate mobility is measured from switch position 5 or 6. A complete data set for one temperature can be made, from the voltage and current readings, from switch positions 1, 2, and 5 or 3, 4, and 6.

Equipment System

The equipment system design used to measure data and control the experiment is shown on the following page; see Figure 25. The sample, mounted to the sample holder, is contained inside a Janis dewar. Inside the dewar, to insure

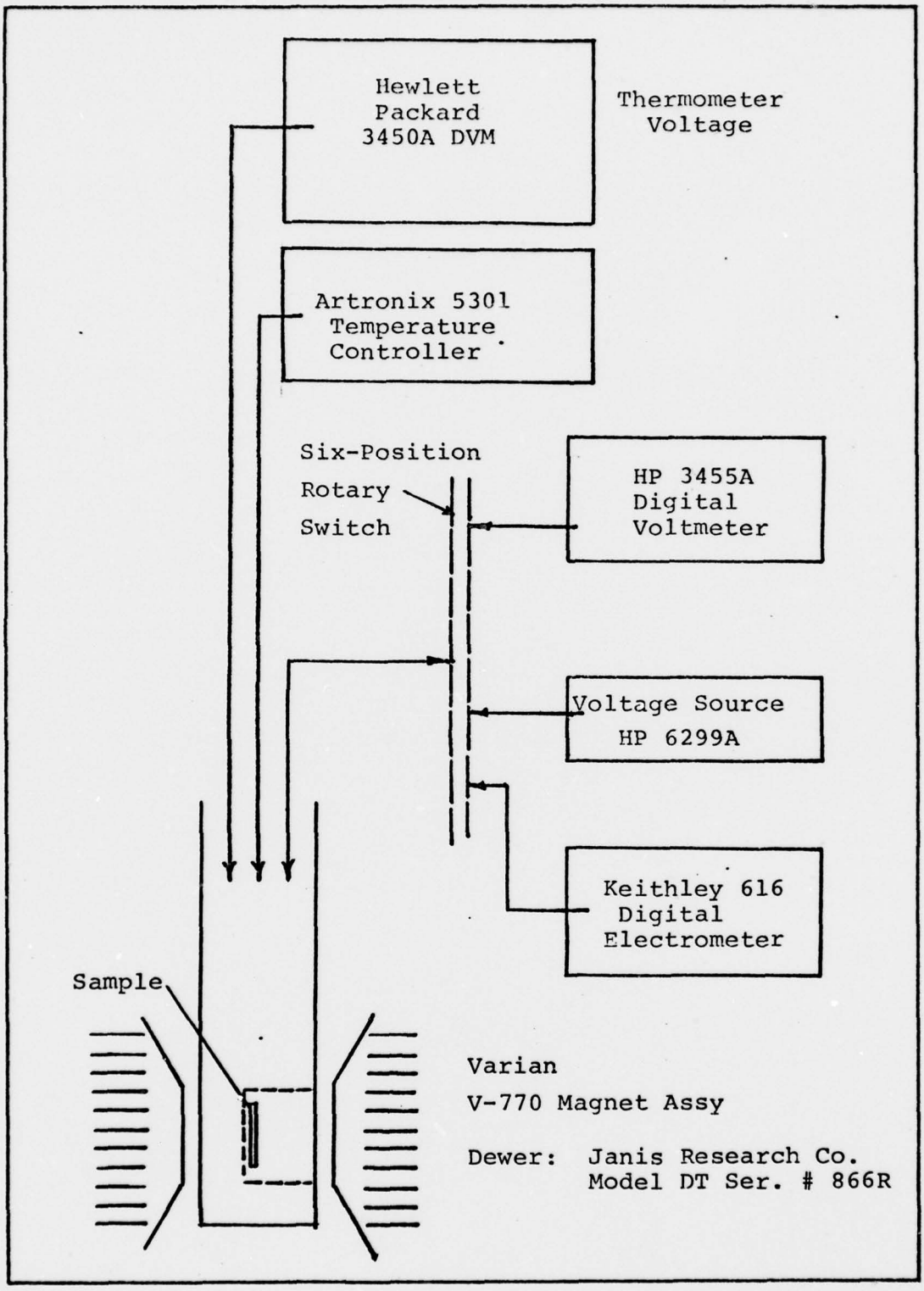

Figure 25 Experimental System Design

proper shielding, the inner shield of the trixial cable and outer shield of the coxial cable are electrically continuous. See Figure 26.

Liquid helium is made to boil as it passes through diffusion heaters near the bottom of the dewar. The vapors then pass over the sample to provide cooling. Two resistance heaters, wound at the ends of the sample holder, are used to control the sample's temperature; see Figure 27.

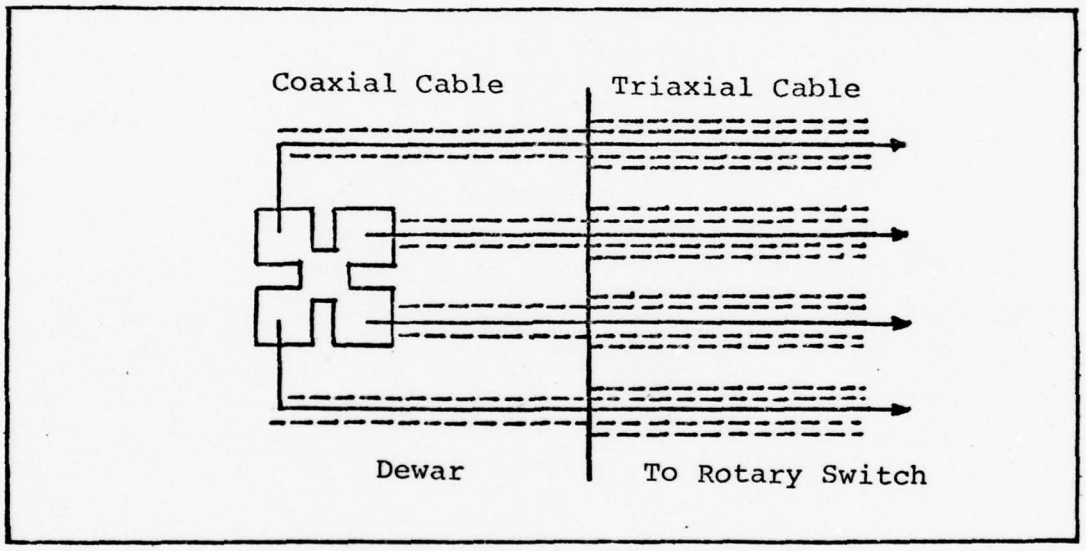

Figure 26 van der Pauw Wiring Detail
The Duetsch Company model DM5606-3719P receptacle and DS07-37195 plug.

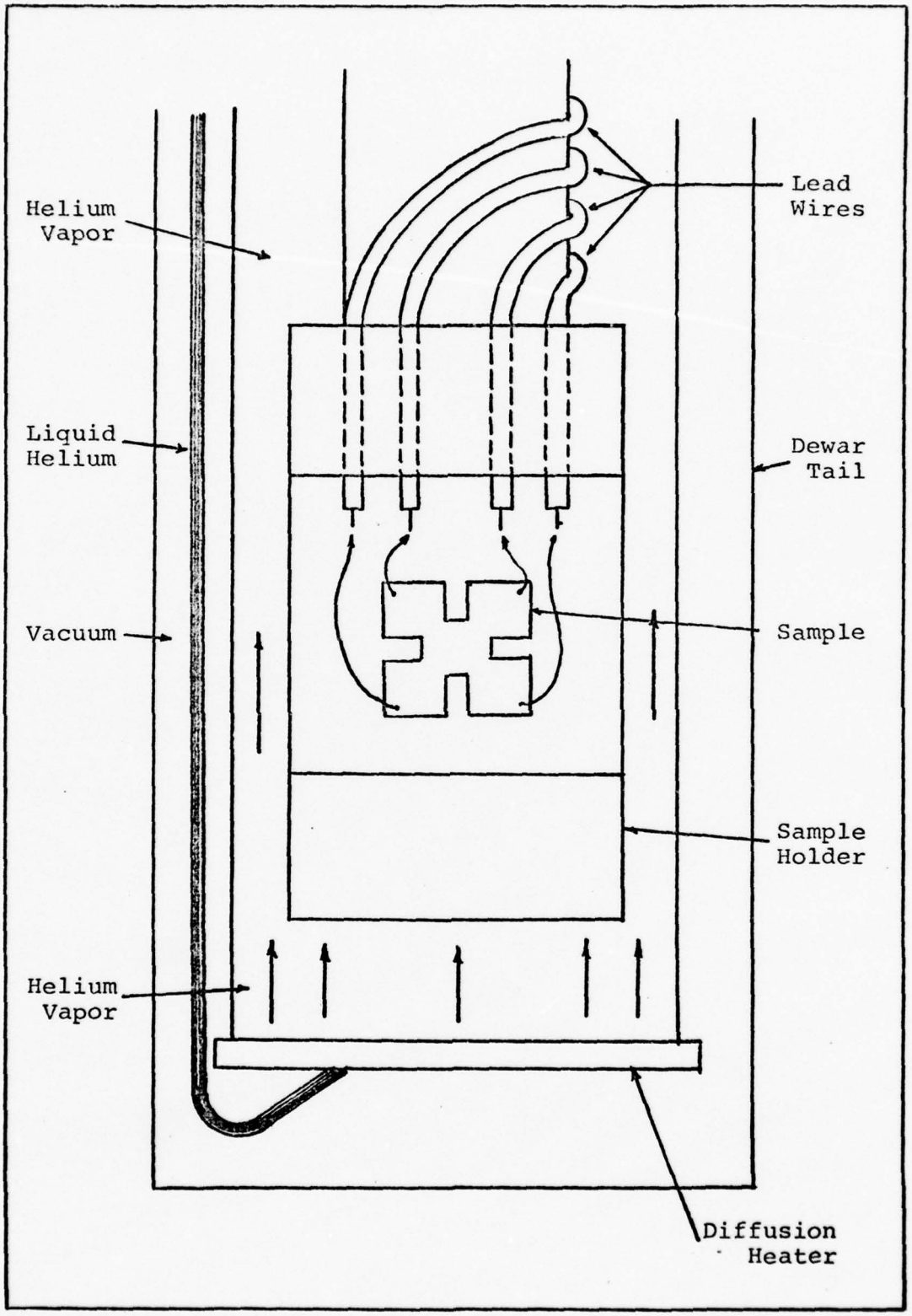

Figure 27 Temperature Control System

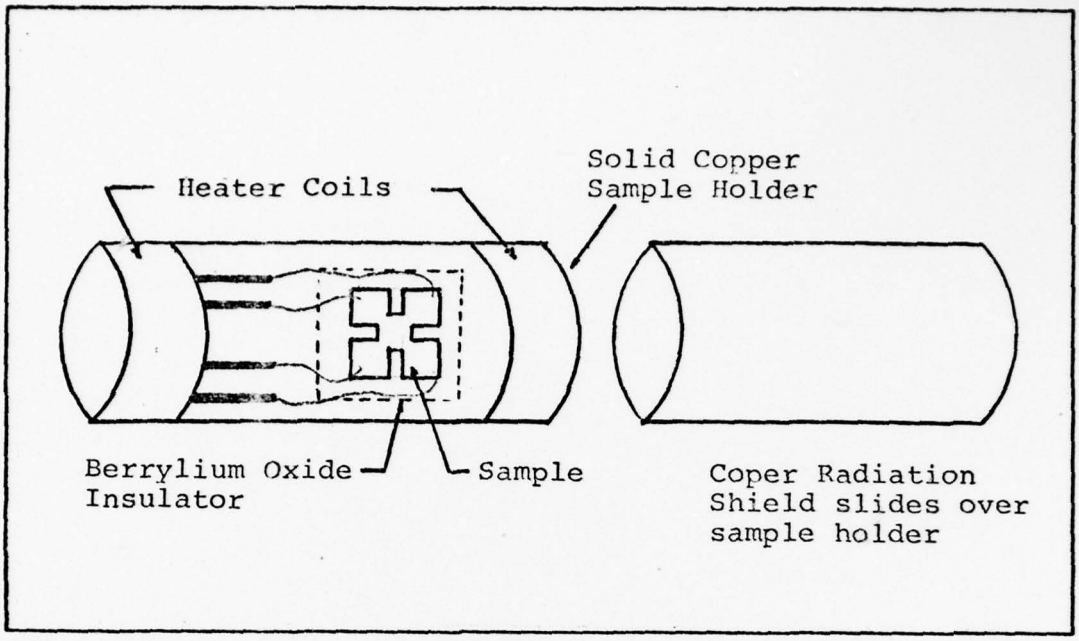

Figure 28 Sample Holder

Sample Holder

Details of the sample holder are shown in Figure 28. The holder provides for easy mounting of the sample for taking Hall data. Soldering the gold wire contacts to the sample holder was accomplished with indium solder.

VI. Data Acquisition and Analysis Techniques

This section explains the procedures and techniques used for the collection of data and its reduction for analysis.

Data Collection Procedures

The electrical transport system used in this study has a temperature range capability from 4.2 to 400 K. Prior to lowering the system's temperature for a sample run, the Keithley 610C electrometers are zeroed to provide unity gain inputs to the measurement equipment; see Figure 23. The van der Pauw sample contacts are checked at room temperature to assure that they are ohmic. This is accomplished by checking the voltage and current readings, from switch positions 1 through 4, to see that they are relatively equal; see Figure 24. The helium flow is then increased to lower the sample's temperature.

The voltage applied to the sample is decreased with temperature to assure that "hot" carriers are not generated in the sample. The applied voltage, which will keep the current in the linear operating range, is shown in Table I.

Table I

Applied Voltage versus Temperature

less than 60 K	2 V
60 - 150 K	3 V
150 - 400 K	4 V

As the temperature is decreased below 100 K the contacts, via switch positions 1 through 4, are repeatedly checked to see that they have not become insulators or rectifiers. As the temperature continues to drop, the contacts will freeze out becoming insulators, at this moment the voltage readings will suddenly begin varying randomly with noise. The contacts may become rectifiers when the Schottky barrier height reaches a level that stops the thermionic emission. Since thermionic emission has a steep temperature dependence, a space charge may develop at the contacts, which prevents current flow from crossing the barrier. These problems can normally be controlled down to 20 K (Ref 4:708).

The starting point for taking data was at the temperature where the contacts began freezing out. This generally occurred between 20 to 30 K. Data was recorded from the lowest temperature attainable up to 400 K according to the following table.

Table II

Data Record Sequence

below 30 K	every degree
30 - 40 K	every two degrees
40 - 100 K	every five degrees
100 - 300 K	every ten degrees
300 - 400 K	every twenty degrees

Resistivity. To reduce systematic errors that may occur in this experiment, when calculating resistivity, an averaging procedure was used in the collection of data. The current direction, for switch positions 1 through 4, was reversed to obtain two independent voltage and current measurements for calculating resistance. These two resistance calculations were then averaged to obtain R_1 or R_2.

$$R_i = \frac{\frac{V_{xy}}{I_{wz}} + \frac{V_{xy}}{I_{wz}}}{2} \quad i = 1, 2 \qquad (22)$$

Ideally, the readings in both current directions should be identical.

Mobility. To reduce systematic errors in the determination of the Hall voltage, the current direction in switch positions 5 and 6, were also reversed to yield two independent measurements. In addition, the random error due to the noise level was eliminated by using two antiparallel directions for the applied magnetic field. Starting with equation (19), instead of taking the absolute value of the change in resistance due to an applied $\bar{B}$ field, readings were taken with one current direction and two magnetic field directions, that are antiparallel. These two readings were then added and divided by 2 to obtain ΔR_e, for one current direction.

Then this same procedure was repeated with the current

direction reversed to obtain another value of ΔR_e to be averaged; see below.

$$\Delta R_e(f) = \left| \frac{\frac{V_x(\bar{B}+) - V_y(\bar{B}+)}{I_{wz}} - \frac{V_x(\bar{B}-) - V_y(\bar{B}-)}{I_{wz}}}{2} \right| \quad (23)$$

$$\Delta R_e(r) = \left| \frac{\frac{V_x(\bar{B}+) - V_y(\bar{B}+)}{I_{zw}} - \frac{V_x(\bar{B}-) - V_y(\bar{B}-)}{I_{zw}}}{2} \right| \quad (24)$$

$$\Delta R_e = \frac{\Delta R_e(f) + \Delta R_e(r)}{2} \quad (25)$$

where

$\Delta R_e(f)$ is ΔR_e calculated with the current in the forward direction

$\Delta R_e(r)$ is ΔR_e calculated with the current in the reverse direction

$V_x(B+)$ is the voltage measured when the magnetic field is applied L - R

$V_x(B-)$ is the voltage measured when the magnetic field is applied R - L

see Figure 25.

This procedure eliminates the off set error created, when there is no applied magnetic field.

Analysis

Early investigation into the conduction in silicon showed that intrinsic and extrinsic conduction existed. Evidence for the existence of both types of conduction was obtained from the measurement of the variation of the Hall coefficient and conductivity with temperature. When a magnetic field is applied normal to the direction of current flow, through a conducting material, an electric field will be created perpendicular to both the magnetic field vector and the current density vector. The Hall coefficient is the ratio of the electric field to the current density times the magnetic field.

$$R = \frac{E_y}{j_x B_z} \tag{26}$$

At low temperature the conductivity and the Hall coefficient of different materials may differ from one another by a factor of 10^4, but at high temperatures the results for all materials tends to fall on the same straight line (Ref 11:12). As expected this common line found at high temperatures indicates an intrinsic region. From the slope of the intrinsic line the energy gap between the valence and conduction bands can be determined. For silicon the gap is approximately 1.12 ev.

The point where the curve for a given material leaves the intrinsic line depends upon the number of impurities present. The concentration of intrinsic carriers falls

rapidly with temperature until the conduction is dominated by extrinsically generated carriers.

Below the intrinsic region the Hall coefficient remains a constant, but at still lower temperatures it starts to rise slowly indicating the carrier concentration is falling. Leaving the intrinsic region and looking at resistivity, which is the inverse of conductivity, it is observed that resistivity falls as temperature is lowered, passing through a minimum, and then rising as temperature decreases further. This behavior is due to the fact that resistivity is a function of two quantities, the concentration of carriers and their mobility. At temperatures near the intrinsic range concentration is a constant (see eq. 12) thus the variation of resistivity is determined by the carrier mobility. This indicates that mobility rises as temperature falls (Ref 11:12-14).

At moderate temperatures mobility is determined by the scattering of holes by lattice vibration, for p-type material. Since lattice vibration decreases with temperature, mobility will rise due to the fact that conduction holes are likely to travel further before reaching a vacancy. At lower temperatures where resistivity is increasing due to the reduction in carrier density, mobility tends to be a constant. At the lowest temperatures where the dominant scattering mechanism is due to impurities, mobility will begin to decrease (Ref 11:14).

From the graphs of the logarithms of carrier concentration and resistivity plotted versus 1/T; it can be shown, that when the dominant factor determining the value of concentration and resistivity is a Boltzmann exponential term, the plots will yield a straight line. The slope of this line will be proportional to the activation energy ϵ_a (see pgs. 29 and B1).

Using these results, the theoretical curves for the logs of resistivity, mobility, and carrier concentration versus 1/T can be drawn, as shown in Figure 29.

Data

From the voltage and current measurements recorded

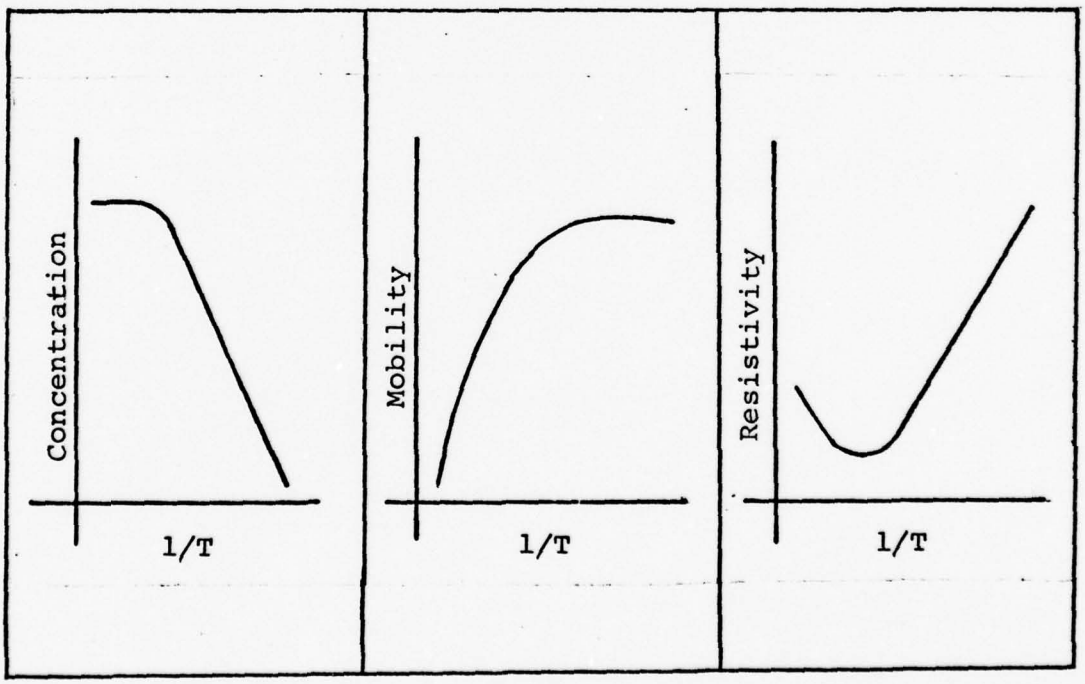

Figure 29 Theoretical Curves

the resistivity, mobility, and carrier concentration were calculated using equations (16), (20), and (21) respectively. In equation (16), the value for $f(R_2/R_1)$ is calculated from equation (18) when:

$$0.36 < R_2/R_1 < 2.8 \qquad (27)$$

Otherwise the graph shown in Reference 14, page 341 was used.

The logarithms of resistivity, mobility, and carrier concentration, along with the R_2/R_1 ratio were plotted against 1000/T; these graphs are shown in appendix A. From the evaluation and analysis of these plots, the temperature range most consistant with theory, was used to fit equation (7) to the calculated values of carrier concentration. A least-squares curve fitting computer routine was used to fit equation (7) to the data, after it is solved explicitly for p. This program determines N_a, N_d, and ϵ_a from the best fit of the data, assuming one acceptor level which is under-compensated. See appendix D.

Error Analysis

Solving equation (7) for p explicitly, the propagation of error for a one level acceptor can be determined.

$$p = \tfrac{1}{2} (N_D + F) \left[\sqrt{1 + \frac{4 (N_A - N_D) F}{(N_D + F)^2}} - 1 \right] \qquad (28)$$

where

$$F = \tfrac{1}{4} N \exp(-\epsilon_a/kT)$$

Given that the fluctuation of the temperature control system is:

$$\Delta T = 0.02 \text{ K} \tag{29}$$

the uncertainty in the carrier concentration can be determined by:

$$\Delta p = \frac{dp}{dT} \Delta T \tag{30}$$

The relative error is then defined from:

$$r = \frac{\Delta p}{p} = \frac{dp}{dT} \frac{\Delta T}{p} \tag{31}$$

After taking derrivatives and rearranging, the relative error in the carrier concentration can be calculated from:

$$r(\%) = 100 \left(\frac{N_A - N_D - p}{2p + N_D + F} \right) \left(\frac{3}{2} + \frac{\epsilon_a}{kT} \right) \frac{F}{p} \frac{\Delta T}{T} \tag{32}$$

The complete derivation is shown in appendix B.

At low temperatures where

$$p \longrightarrow \frac{N_A - N_D}{N_D} F$$

and (33)

$$F \longrightarrow 0$$

equation (32) reduces to:

$$r \approx \left(\frac{3}{2} + \frac{\epsilon_a}{kT} \right) \frac{\Delta T}{T} \tag{34}$$

Using boron as an example, where $\epsilon_a = .045$ ev, the following table can be generated using equations (29) and (34).

Table III

Relative Error versus Temperature

r (%)	T(K)
42.0	5
10.7	10
2.76	20
1.26	30
0.73	40

At higher temperatures the propagation of error, due to the uncertainty in the temperature of the control system (ΔT), has very little effect.

Sample data, taken previous to this report, was analyzed to determine its accuracy. Given this data, taken from van der Pauw measurements at one temperature, the standard deviation was calculated using statistical control charts. From these calculations, and the fact that no measurements in this investigation were taken below 20 K, a reasonable estimation of the sample data error can be made. That is, the error in resistivity, mobility, and carrier concentration, for all temperatures investigated, is slightly less than 3 percent.

VII. Results

This section first explains the assumptions that are made to assure the validity of the data. Second, is a general discussion of the samples tested and any peculiarities that occurred during data collection. Third, is a detailed breakdown of the specific results for each sample tested. Fourth, is the etching results of the samples. And lastly is a report on a flatness study performed on one of the silicon samples.

Assumptions

The conductivity σ is defined as the ratio of the current density j to the electric field E.

$$\sigma = j/E \tag{35}$$

It is necessary to specify that E be small, so that Ohm's law is obeyed. This assures that carriers are generated thermally and not by the applied electric field. At room temperature there is generally no problem since the maximum permissible steady field is usually limited by Joule heating (Ref 11:23). However, at low temperatures in semiconductors this is not the case. But, by keeping the applied voltage low to assure that "hot" carriers are not generated, Ohm's law will be obeyed.

A further condition of the measurements is the

assumption that conditions are isothermal. That is to say, temperature gradients do not exist across the sample. Also rectification effects at the contacts are assumed not present. The guarded Hall system greatly reduces all rectification effects; additionally, the contacts were checked prior to each sample run.

The effective mass for holes, although known to vary with temperature, is assumed to be a constant equal to .591 times the mass of the electron. This value calculated from the heavy, light, and split-off holes is used in the curve fitting computer routine.

Lastly, for this investigation the "r" factor, which is defined as the ratio of the Hall mobility to the drift mobility, is assumed to be a constant. The Hall mobility, calculated in this thesis, is determined from the Hall voltage which results from a magnetic field applied normal to the sample; see Figure 21, and equation (20). When an electric field is applied along a material, a component of the velocity in the direction of the field is added to the random thermal velocities of the atoms in the specimen. The drift mobility is the ratio of this velocity component divided by the electric field intensity. Currently research on the "r" factor is being carried on, but for this project it is assumed to be 1.

Samples Tested

To investigate the uniformity of web-dendrite silicon

the ratio of the resistance, in two perpendicular directions across the sample, was determined. The ratio, R_2/R_1, was calculated and plotted over the entire temperature range of the sample run. Ideally, this ratio for a geometrically symmetrical sample should be 1.

The growth direction was determined from the bounding dendrites for each sample. It is known that the arrow head shaped dendrites point down into the melt as they grow. Hence, their growth direction is down into the melt. However, the growth direction of the web region is out from the surface of the melt; this is the growth direction referred to in this report (Ref 2). R_1 and R_2 are referenced to the growth axis to facilitate the evaluation of the material's homogeneity. The growth direction relative to R_1 and R_2 is shown, for each sample tested, in appendix A.

At the lowest temperatures, where the contacts began freezing out, data was taken in all six switch positions at each temperature, for comparison. As the data will show, at temperatures below 30 K, there was a dramatic difference between the resistances calculated from switch positions 1 and 3. From Figure 24, it can be seen, that these two measurement configurations should yield identical results. As the sample temperature was increased this variation disappeared. The data was then alternately taken between the 1, 2, 5 switch position group and the 3, 4, 6 switch position group. (Except for Boron 1 run 1 explained later).

Eight web silicon samples were tested. They will be differentiated according to their dopant and the following list.

1. Boron 1 run 1
2. Boron 1 run 2
3. Boron 2
4. Boron 3
5. Boron 4
6. Gallium 1
7. Gallium 2
8. Undoped

Boron 1. This sample was evaluated in two different configuration: first, with R_2 parallel to the growth axis; second, with R_1 parallel to the growth axis.

Boron 2. This sample was cut out from the same growth run of web as Boron 1. Their separation along the web axis was unknown. However, it could be determined from the width of the web that Boron 1 solidified first.

Boron 3 and 4. These samples were cut out from the same piece of web; the distance between their center regions was approximately 1 cm. Boron 3 was cut out with one edge parallel to the growth axis. Boron 4 was cut out with its edges at 45° to the growth axis.

Gallium 1 and 2. These samples were from two different silicon pieces. Both samples were known to have a faint trace of linage, in the center of the web, running parallel to the growth axis.

All samples were observed to have one fairly flat side and one slightly concave. From the position of the web relative to the bounding dendrites each sample contained a twin lamella; see Figure 12 (Ref 2).

Sample Results

Boron 1 run 1. This sample was tested from 29 to 160 K. Data was taken from all six switch positions which gave two data points per temperature. This was done for two reasons: first to provide more experience with the temperature control system and secondly to show that switch positions 1, 2, and 5 will yield nearly identical results as positions 3, 4, and 6; under normal conditions (see Fig. 24).

Below 38 K the R_2/R_1 ratio was such that this sample showed signs of inhomogeneity. As the sample temperature was increased the ratio approached and remained about 1.05. The resistivity calculated from the lowest temperatures displayed departure from expected. From the lowest temperatures up to approximately 60 K the logarithm of resistivity against $1/T$ should be a straight line (see app. B). The deviation in the resistivity plot, from its theoretical curve, occurs where the R_2/R_1 ratio decreases. Resistivity reached its lowest value at 95 K.

The mobility calculated can be seen from its plot, to behave as expected. Mobility was maximum at 36 K.

The low temperature portion of the concentration plot bends away from its theoretical curve. This occurs where

the R_2/R_1 ratio decreases from a steady value. From the concentration plot and consideration of the R_2/R_1 ratio, the values from 38 to 160 K were used to determine N_a, N_d, and ϵ_a from the curve fitting routine. However, since the data was not taken at higher temperatures an exhaustion region was never reached. Thus, the values determined from the computer routine are not considered accurate. This run was aborted at 160 K due to a system malfunction.

Boron 1 run 2. This run, a continuation of Boron 1 run 1, served two purposes: first, to complete the high temperature data record, and second, to reassure that the R_2/R_1 ratio deviation at low temperatures was not due to the system or its alignment. To accomplish this, the sample was rotated in the sample holder, such that R_1 was now parallel to the growth axis.

Boron 1 run 2 was tested from 28 to 320 K. Above 38 K the R_2/R_1 ratio maintained a steady value of .950; below this temperature the ratio increased to 8.0. The steady value of .950 is the inverse of run 1 as expected.

At the lowest temperatures, the resistivity plot showed the same deviation as run 1. From the mobility plot, it can be seen that its calculated values behaved as theory dictates.

The low temperature portion of the concentration curve bends away from the theoretical curve where the R_2/R_1 ratio is poor. At 180 K there appears to be a discontinuity in the carrier concentration graph. Reviewing the data

showed that the second 180 K point through 320 K was taken three days after the lower temperature portion.

Resistivity reached its lowest value at 95 K. Mobility was maximum at 36 K. Noting the discontinuity at 180 K and the poor R_2/R_1 ratio at the lower temperatures, it was decided that the best fit would be made using the data between 36 and 180 K.

Boron 2. This sample was tested from 22 to 380 K. Data from temperatures lower than the previous boron-doped sample was measured. Since this sample is from the same silicon growth run, it can be assumed that these contacts were better.

The R_2/R_1 ratio had a steady value of 1.02 above 38 K. Below this temperature the ratio slowly increased to 2.0 at 25 K, then it climbed to 3.5 at 22 K.

The resistivity calculated did not depart very much from the norm. A slight bending can be noted below 28 K. The mobility again behaved as expected.

The carrier concentration plot deviated quite drastically from the theoretical curve below 30 K. The high temperature region behaved well. Above 300 K the conduction appears to be approaching the intrinsic region.

Resistivity reached a minimum at 90 K; while mobility reached a maximum at 32 K. The temperature range from 32 to 170 K was chosen for curve fitting the data for the following reasons. First the lower temperatures were picked where the R_2/R_1 ratio smoothed out. Second the

temperatures above 250 K were dropped to insure data used was not from the intrinsic conduction region. And lastly, values above 170 K were not included, so that a more direct comparison with Boron 1 run 2 could be made. When the temperature range from 32 to 250 K was used the value calculated for ϵ_a was .041 ev, which is far below the accepted activation energy for boron. Possible reasons for this are discussed in the conclusion. Over all this was the best sample tested.

Boron 3. This sample was evaluated from 20 to 400 K. Its R_2/R_1 ratio was not as bad at the lowest temperatures as compared with the previous boron-doped samples. At the lowest temperatures R_2/R_1 was 1.8 but a steady state value of 1.24 - 1.26 was not reached until 50 K. This points to inhomogeneities in the material.

The resistivity showed the same tendencies to bend away from a straight line until the R_2/R_1 ratio reached a steady state. The mobility was very constant between 22 and 36 K. At 20 and 21 K the sudden drop in mobility indicates that the contacts were beginning to freeze out.

The low temperature portion of the concentration curve deviated from the theoretical curve. Again, this occurred where the R_2/R_1 ratio diverged from its steady state value. Above 260 K the sample appears to be approaching the intrinsic conduction region.

Resistivity reached its minimum value at 95 K and mobility reached a maximum at 26 K. To determine the values

for N_a, N_d, and ϵ_a the temperature data below 32 K was discarded due to the R_2/R_1 ratio. The high temperature cut off of 240 K was picked to insure that conduction from the intrinsic region was not included.

Boron 4. This sample was cut out with its growth axis 45° from the bounding dendrites. Previous boron-doped samples were cut out with their growth axis parallel or pendicular to R_1. With this sample cut out at 45°, it was believed that the R_2/R_1 ratio should yield 1. Figure 30 shows the position of Boron 3 and 4 on the web.

This sample was evaluated from 20 to 400 K. The R_2/R_1 ratio displayed a randomness not seen previously. At temperatures below 25 K the ratio was very near 1. But, as the temperature was increased, the ratio oscillated between 1.23 and 1.27. The reason for this fluctuation was not fully understood until the sample was later etched.

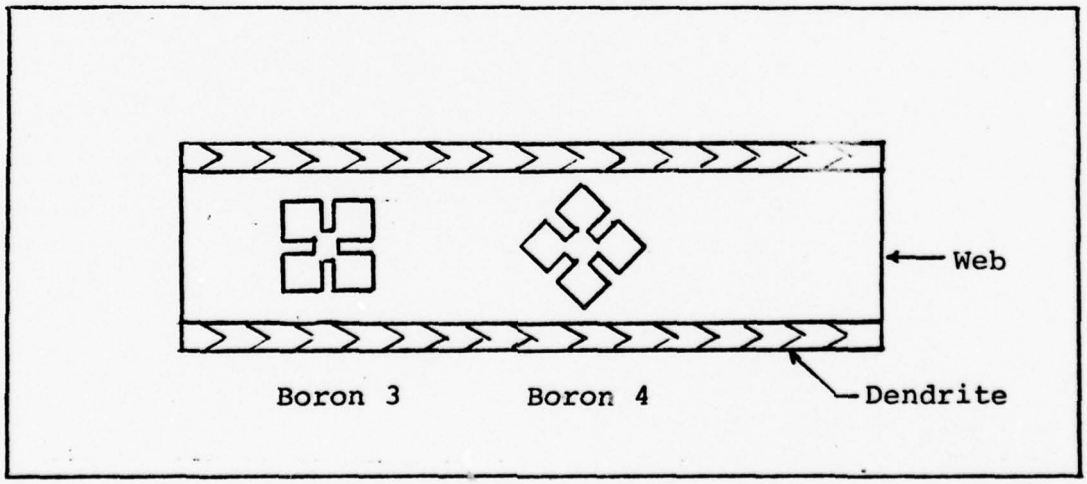

Figure 30 Boron-Doped Samples

The resistivity, mobility, and carrier concentration values are almost identical to Boron 3's results. Resistivity had a minimum at 95 K and mobility showed a maximum at 24 K. The same temperature range for concentration was used to calculate N_a, N_d, and ϵ_a. These values for Boron 3 and 4 were within 10 percent of each other.

It was suprising to note the difference in thickness of these two boron-doped samples. Their center region was less than 1 cm apart, yet their thickness was 0.0008 cm different. This value although appearing quite small plays a key role in describing the quality of the web.

Gallium 1. This sample was examined from 30 to 318 K. Its R_2/R_1 ratio varied from .54 - .89 between 30 and 95 K. Above 100 K the ratio remained between .91 and .93. Although this sample displayed the most inhomogeneities; seen from its varying R_2/R_1 ratio, the resistivity plot was very closely aligned with theory. The minimum resistivity occurred at 150 K.

This sample's mobility calculations increased with a decrease in temperature, then its values flattened out to a fairly constant region between 32 and 50 K. At the lowest temperature, 30 K, the mobility drops quite drastically, probably due to the contact's limitation or defects. The maximum mobility occurred at 38 K.

Shown on the concentration graph the lower temperature region approached a straight line. The high temperature portion above 150 K never really bent over indicating that

the carriers were being exhausted. The complete temperature set was used for the curve fitting routine except for two points: 30 K because it deviated from the straight line theory; and 220 K because there was a 20 percent difference in its value from its nearest neighbor data. From the calculation of N_a, this sample is considered heavily doped. This is undoubtably the reason for the exhaustion region never being reached.

This gallium-doped sample is suprisingly complex to analyze. It is known to have a line of dislocations running down the web parallel to its growth axis. Evidence to this fact can be seen from its wildly varying R_2/R_1 ratio. However, the resistivity, mobility, and carrier concentration calculated can be seen to approach their theoretical curves quite well. These values alone would not indicate that any defects existed.

The 318 K temperature limit was due to the capability of the Artronix controller.

Gallium 2. This sample was run from 26 to 310 K. At the lower temperatures below 36 K the measurements from switch positions 3 and 4 gave quite different readings than positions 1 and 2 respectively. This indicated that one of the contacts was not as reliable as the other three. Since, position 3 and 4 showed the most random variation in its R_2/R_1 ratio, this additional data from switch position 1 and 2 was taken for comparison. Observing the R_2/R_1 plot, the

ratio began smoothing out about 50 K and by 95 K it held at roughly 0.80.

The resistivity plot, not including a few of the bad data points at the lower temperatures, approaches the theoretical curve very well. The minimum resistivity occurred at 150 K.

The mobility behaved as expected above 36 K. Below this temperature a randomness is displayed that can only be attributed to the poor contact. There appears to be two mobility maximums at 36 and 27 K. However, at the 27 K data point the R_2/R_1 ratio indicates a contact problem existed; this data point was thrown out.

Observing the concentration plot the high temperature region appears to reach the exhaustion region, while the low temperature data bends away from the theoretical straight line. This occurs below 36 K where the R_2/R_1 ratio is low. Therefore, the values selected for calculating the impurity concentrations and the activation energy were from 36 to 310 K.

Undoped. This silicon sample was evaluated from 20 to 320 K. Again there was difficulty with one of the contacts, as seen from the data. At the lowest temperatures the R_2/R_1 ratio fluctuated between .20 and .45. At 50 K the ratio steadied out at 1.20.

The fluctuation in the R_2/R_1 ratio is displayed in the resistivity curve at the lower temperatures. Here,

resistivity bends away from the theoretical curve. The minimum value of resistivity occurred at 80 K.

The mobility graph also shows a random fluctuation at the low temperatures. As the case with resistivity this variance is due to the R_2/R_1 ratio, which may be due to the contacts. The mobility maximum occurred at 38 K; the region from 27 to 50 K was fairly flat as expected.

From the low temperature range of the concentration curve, the R_2/R_1 ratio effect can be seen. Below 30 K the plot bends away from the straight line theory. Observing the high temperature region it appears that the exhaustion region was never reached. However, after the activation energy was determined, the bending upwards can be attributed to intrinsically generated carriers.

Several different temperatures ranges were used to fit the data to equation (7). The best fit occurred when the data from 32 to 180 K was used. From N_a and N_d calculated it can be seen that this material contained nearly the same amount of donor and acceptor impurities. However, the activation energy of .0397 ev can not be fully explained. Theory tells us the activation energy is the slope of the concentration curve where the Boltzmann exponential is the dominant factor. But none of the standard donor nor acceptor impurities display this value for their activation energy. Undoped samples normally have boron impurities present due to the quartz crucible they are grown from. But a boron slope is not present (Ref 2).

Curve Fitting

The last graph for each sample shows the curve fitting results from the selected data. The boron-doped samples displayed the best results due to only one distinct impurity level being present. The least squares error in these fits was less than 4 percent in all cases.

The gallium-doped samples displayed two slopes: one has the value of ϵ_a and the other $\frac{1}{2}\epsilon_a$. The appearance of these two slopes is due to the gallium-doped samples being very slightly compensated; that is $N_a >> N_d$ (Ref 11:126). A comparison of differently compensated materials is shown in Reference 11, page 126.

The undoped sample was the most difficult to fit due to the high temperature region never bending over when the carriers are exhausted. The intrinsic carriers begin adding to conduction before the impurities are exhausted.

Etching Results

Pieces adjacent to all the samples tested were etched to observe dislocations and possibly other defects. The etchant used was two parts hydrofluoric acid to one part Chromic acid. The etchant dissolves points where defects are located faster than undamaged lattice sites.

Pieces next to Boron 1 and 2 showed defects running down through the web material parallel to the [111] planes. Also secondary twins were observed under 200X magnification. The surfaces of both samples revealed that they contained greater than 10^3 dislocations per square centimeter.

Boron 3 and 4 both showed a line of defects running down through the web parallel to the [111] planes; but no secondary twins were observed. The surfaces had greater than 10^5 dislocation per cm^2; there were areas on the web that had denser regions of dislocations, but this may be due to uneven etching effects (Ref 2).

Gallium 1 was known to have a line of defects in the center of the web parallel to the growth axis. Gallium 2, after etching, showed a dislocation density greater than $10^3/cm^2$ on its surfaces. Additionally, lines of dislocations running in random directions across the surface of the web were seen.

The "undoped" piece also showed more than 10^3 dislocations per cm^2 on its surfaces. And lines of dislocations crisscrossed the sample on both faces.

Flatness Report

The "undoped" web sample was surveyed for surface flatness on a Sloan dektak surface profile measure system. The Dektak scan shows that the sample was grown in the configuration shown in Figure 14. Regardless of the asymmetrical growth, both sides of the sample met the Air Force standard required for flatness of detector material (Ref 2). The scan is shown in appendix C.

Comparison of Results

Table IV shows a comparison of the results of all eight web samples. The explanation of the values contained in

the table and their corresponding units are as follows.

$N_a - N_d$ high temperature region of equation (7) (cm^{-3})

N_a concentration of acceptors (cm^{-3})

N_d concentration of donors (cm^{-3})

ϵ_a activation energy of acceptors (ev)

min ρ minimum resistivity obtained at that temperature (ohm-cm)

max μ. maximum mobility obtained at that temperature (cm^2/volt-sec)

R_2/R_1 steady resistance ratio at higher temperatures

ρ wrt GD resistivity is greater across or with the growth axis

30, 100, and 300 K are low, medium, and high temperature data points shown for comparison.

Comparison of Results

Table IVa

	Boron 1 run 1	Boron 1 run 2	Boron 2	Boron 3	Boron 4
$N_a - N_d$	1.09E15	1.01E15	8.15E14	1.37E15	1.12E15
ϵ_a	.043	.043	.044	.043	.042
N_a	1.66E15	1.49E15	1.10E15	1.97E15	1.81E15
N_d	5.71E14	4.82E14	2.84E14	6.00E14	6.62E14
min. ρ	1.48	1.44	1.98	1.47	1.53
@ °K	95	95	90	95	95
max. μ	1.81E04	1.96E04	1.89E04	1.78E04	2.01E04
@ °K	36	36	32	26	24
R_2/R_1 steady	1.05	.95	1.02	1.24	1.25-1.27
ρ wrt GD*	gw**	gw	ga†	ga	-
30 K					
ρ	1.35E04	1.29E04	2.60E04	1.92E04	1.99E04
μ	1.49E04	1.74E04	1.84E04	1.72E04	1.92E04
con	3.10E10	2.77E10	1.28E10	1.89E10	1.64E10
R_2/R_1	.217	4.630	1.196	1.314	1.231
100 K					
ρ	1.49	1.47	2.00	1.47	1.53
μ	5.56E03	5.64E03	5.13E03	4.51E03	5.13E03
con	7.81E14	7.55E14	6.12E14	9.42E14	7.98E14
R_2/R_1	1.055	.949	1.018	1.245	1.626
300 K					
ρ	-	12.49	17.28	11.25	11.64
μ	-	3.84E02	3.85E02	3.61E02	4.18E02
con	-	1.30E15	9.38E14	1.54E15	1.28E15
R_2/R_1	-	.952	1.017	1.231	1.264

* resistivity with respect to growth direction
** greater with growth direction
† greater across growth direction

Comparison of Results

Table IVb

	Gallium 1	Gallium 2	"Undoped"
N_a-N_d	1.21E16	7.25E14	1.47E14
ε_a	.065	.063	.040
N_a	1.26E16	7.95E15	4.77E14
N_d	4.74E14	6.96E14	3.30E14
min. ρ	.88	.81	6.01
@ °K	150	150	80
max. μ	7.75E03	1.46E04	2.89E04
@ °K	38	36	38
R_2/R_1 steady	.91-.93	.80	1.21
ρ wrt GD	ga	ga	gw
30 K			
ρ	2.81E07	1.02E07	2.15E04
μ	5.59E03	4.78E03	2.82E04
con	3.98E07	1.25E08	1.03E10
R_2/R_1	.594	.702	.704
100 K			
ρ	1.59	1.45	6.86
μ	2.87E03	4.84E03	7.03E03
con	1.37E15	8.92E14	1.29E14
R_2/R_1	.908	.794	1.211
300 K			
ρ	2.45	2.27	76.87
μ	2.14E02	3.52E02	4.27E02
con	1.18E16	7.82E15	1.90E14
R_2/R_1	.915	.798	1.211

VIII. Conclusion

From the start of this investigation, one of the prime objectives was to analyze carefully the electrical transport properties of web-dendrite silicon; to determine the quality of the material's homogeneity. The van der Pauw measurement technique provided the means to determine this property through the R_2/R_1 ratio. As stated previously uniformity in a sample should yield an R_2/R_1 ratio of 1.

R_2/R_1 Ratio

If the R_2/R_1 ratio is greater than 1, it can safely be assumed that, if this is due solely to the characteristics of dendritic-web growth, that this ratio should be greater than 1 at all temperatures. The converse should also be true if the ratio were less than 1.

The results do not confirm this assumption. At low temperatures, the resistance measured across the web, of every sample tested, was greater than the resistance measured parallel to the growth axis. However, at higher temperatures where the R_2/R_1 ratio was fairly constant, this was not always the case. Examining the results obtained from Boron 1 and 2, both from the same growth run, different R_2/R_1 ratios with respect to the growth axis were calculated (see table IVa). At the higher temperatures Boron 1's results indicate that the resistivity is greater measured parallel

to the growth axis. Boron 2's results displayed just the reverse.

These results are most likely due to different dislocations/defects that propagated into each sample. Both samples revealed secondary twins under magnification, and dislocation lines running parallel to the growth axis. Since it is known that dislocations play some part in the electrical transport properties, it can be surmised that their effect is greater at lower temperatures. Dislocations, although their numbers are far less than impurity concentrations, contain dangling bonds that influence the resistivity and mobility in a crystal (Ref 8:33). Apparently, these dangling bonds have greater effect as the extrinsic carrier density decreases at lower temperatures.

A second anomaly comes to light when comparing Boron 3 and 4. Boron 4's design should eliminate any R_2/R_1 ratio variation from 1, due to any pecularities of the growth technique. But, it did not; the resistance ratio displayed a randomness that could only be explained by dislocation/defect analysis. The difference in the thickness of these samples also shows that they were not the best web-dendrite material grown. In all the samples, thickness variation could be visibly seen in the web. During sample preparation these areas were avoided where possible.

The gallium-doped sample's calculated resistance ratio showed greater consistancy than the boron-doped material.

The resistivity measured across the growth axis was greater than that measured parallel to it, at all temperatures examined. However, again both samples were known, prior to testing, to contain traces of linage. The linage, stated from Westinghouse, ran parallel to the growth axis.

These results experimentally confirm Matare's work that the resistivity measured across a line of dislocations is greater than measured parallel to them.

In summary, no definitive conclusions can be made in regard to web-dendrite silicon as a potential detector material. All samples displayed qualities that would eliminate them for device fabrication. But, it is not fully known if the dislocations and defects are characteristic of dendritic-web growth. Reference 7 indicates that good quality web silicon was grown and tested to meet required standards for position-sensitive detectors. Unfortunately, the samples investigated in this thesis were not of the quality to meet Air Force needs as detector grade material.

From the electrical transport properties results on Boron 3 and the Dektak scan report, it can be seen that the potential may exist for this material in detector use. Above 30 K Boron 3's resistivity ratio was nearly acceptable for detector operation. The Dektak scan shows that even poorly grown samples meet the required flatness criteria for detectors. The cost of producing web is far less expensive than other growth methods, so further studies are warranted.

Further Observations

Resistivity. The boron-doped statistics show, that for impurity concentrations near 1.0×10^{15} cm^{-3}, the minimum resistivity occurs at 95 K. For gallium-doped samples this minimum was seen to occur at 150 K. Since the resistivity calculated from the van der Pauw technique is independent of direction in the web, (see eq. 16) these same results would be expected in other similarly doped samples.

Mobility. The mobility results do not yield the same type of generality as resistivity does. But, mobility calculated from the van der Pauw technique is not independent of direction. The relative direction of mobility is determined from use of Switch position 5 or 6; see Figure 24.

Recommendations

Position-sensitive surface-barrier detection fabrication from web silicon has been tested. The results state that web material is well suited due to its long lengths, flexibility, high surface lifetimes, and uniformity of resistivity (Ref 7:247). This would indicate that higher quality web silicon may exist for further investigations.

Additionally, laser annealling of the current samples may improve their quality sufficiently to warrant re-testing.

Lastly, recommended to me by Dr. Joseph Lang of Thomas C. More College in Fort Mitchell, Kentucky; was the collection of more data in the lower temperature range. More precise curve fitting would result if data were evenly

spaced along the abscissa. Weighting the data by $1/kT$ was tried, to give the lower temperature points more weight. However, the data at lower temperatures is less accurate, and the results obtained from weighting were not as accurate. The following temperature steps are recommended to improve analysis techniques.

20 - 50 K	1 degree steps
50 - 70 K	2 degree steps
70 - 100 K	5 degree steps
100 - 200 K	10 degree steps
200 - 400 K	20 degree steps

Bibliography

1. Baleshta, T. M. and J. D. Keys. "Single Electrometer Method of measuring Transport Properties of High-Resistivity Semiconductors," American Journal of Physics, 36: 23-26 (Jan 1968).

2. Chandler, Thomas C. Lieutenant, United States Air Force (Personnal Communications), Air Force Materials Laboratory, Wright-Patterson AFB, Ohio (Aug 1978).

3. Dermatis, S. N. and J. W. Faust Jr. "Semiconductor Sheets for the Manufacture of Semiconductor Devices," Communication and Electronics, published by The Institute of Electrical and Electronics Engineers Inc. (Mar 1963).

4. Dobbs, B. C., P. M. Hemenger, and S. R. Smith. "Ohmic Contacts on High-Purity p-type Silicon," Journal of Electronic Materials, 6 (6): 705-714 (April 1977).

5. Faust, J. W. Jr. Panel Discussion: Web-Dendrite AFML-Contract F33615-77-C-5003, Air Force Materials Laboratory, Wright-Patterson AFB, Ohio (July 28, 1977).

6. Hemenger, P. M. "Measurement of High Resistivity Semi-Conductors Using the van der Pauw Method," Review of Scientific Instruments 44 (6): 698-700 (June 1973).

7. Ludwig, E. J., W. M. Gibson, and J. S. Hood. "Utilizatio of Web Silicon for Position-Sensitive Detectors," IEEE Transactions on Nuclear Science, published by The Institute of Electrical and Electronics Engineers Inc. (Feb 1965).

8. Matare, Herbert F. Defect Electronics in Semiconductors. New York: John Wiley and Sons, Inc. 1971.

9. M^{c}Kelvey, J. P. Solid State and Semiconductor Physics. New York: Harper and Row, 1966.

10. O'Hara, S. and G. H. Schwuttke. "Dislocation Reactions in Silicon Web-Dendrite Crystals," Journal of Applied Physics, 36 (8): 2475-2479 (Aug 1965).

11. Putley, E. H. The Hall Effect and Semi-Conductor Physics. New York: Dover Publications, Inc. 1968.

12. Seidensticker, R. G. "Dendrite Web Silicon for Solar Cell Application," Journal of Crystal Growth 39: 17-22 (Jan 1977).

13. van der Pauw, L. J. "Method of Measuring Specific Resistivity and Hall Effects of Discs of Arbitrary Shape," Phillips Research Reports 13: 1-9 (Feb 1958).

14. van der Pauw, L. J. "A Method of Measuring the Resistivity and Hall Coefficient on Lamellae of Arbitrary Shape," Phillips Technical Review 20: 220-224 (Mar 1958).

Appendix A

For the values listed in the tables contained in this appendix, where there are two sets of values at one temperature, the first is from switch positions 1, 2, and 5; the second set is from switch positions 3, 4, 6 (see Fig. 24). The units for the values listed in these tables are:

Resistivity	ohm-cm
Mobility	cm^2/volt-sec
Concentration	cm^{-3}

Boron 1 run 1

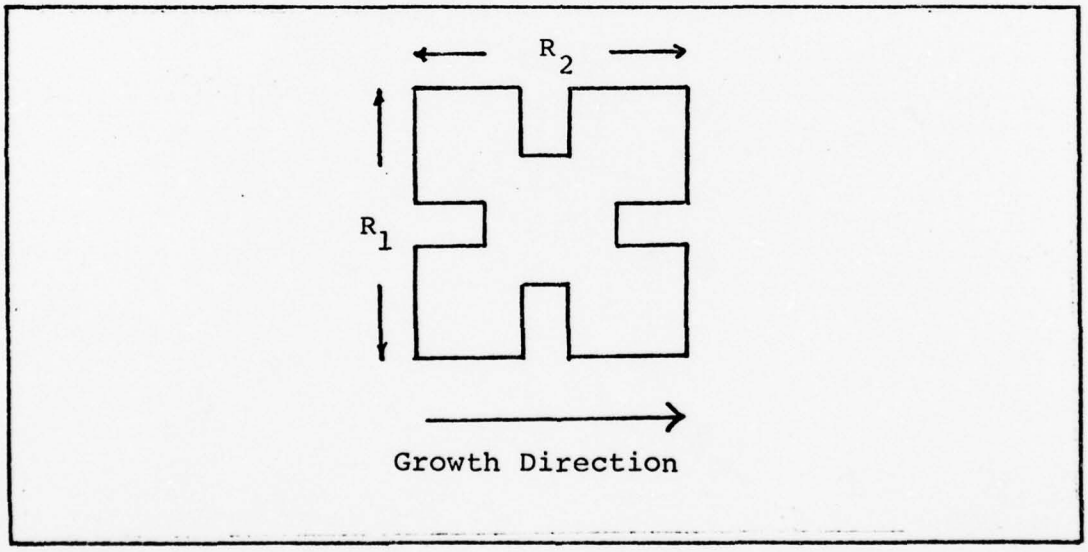

Figure A1 Resistances Relative to the Growth Axis

$N_a = 1.662 \times 10^{15}$ cm^{-3}

$N_d = 5.713 \times 10^{14}$ cm^{-3}

$\epsilon_a = .0428$ ev

thickness .022 cm

Boron 1 run 1

Table V

TEMP	1000/T	RATIO	RESISTIVITY	MOBILITY	CONCENTRATION
29	34.483	.165	2.152E+04	1.392E+04	2.083E+10
29	34.483	.188	2.234E+04	1.406E+04	1.987E+10
30	33.333	.217	1.351E+04	1.492E+04	3.096E+10
30	33.333	.242	1.358E+04	1.514E+04	3.035E+10
32	31.250	.343	5.879E+03	1.646E+04	6.451E+10
32	31.250	.362	5.935E+03	1.627E+04	6.464E+10
34	29.412	.505	2.661E+03	1.737E+04	1.351E+11
34	29.412	.523	2.685E+03	1.718E+04	1.354E+11
36	27.778	.647	1.330E+03	1.807E+04	2.598E+11
36	27.778	.676	1.356E+03	1.777E+04	2.590E+11
38	26.316	.801	6.692E+02	1.739E+04	5.365E+11
38	26.316	.802	6.561E+02	1.769E+04	5.379E+11
40	25.000	.900	3.427E+02	1.722E+04	1.058E+12
40	25.000	.906	3.348E+02	1.747E+04	1.056E+12
45	22.222	1.015	8.072E+01	1.596E+04	4.845E+12
45	22.222	1.015	7.878E+01	1.647E+04	4.811E+12
50	20.000	1.044	2.477E+01	1.486E+04	1.696E+13
50	20.000	1.046	2.473E+01	1.495E+04	1.698E+13
55	18.182	1.048	9.763E+00	1.355E+04	4.720E+13
55	18.182	1.053	9.656E+00	1.380E+04	4.685E+13
55	18.182	1.053	1.049E+00	1.365E+04	4.358E+13
55	18.182	1.044	1.055E+00	1.339E+04	4.416E+13
60	16.667	1.049	5.347E+00	1.212E+04	9.630E+13
60	16.667	1.057	5.335E+00	1.226E+04	9.542E+13
65	15.385	1.055	3.176E+00	1.083E+04	1.814E+14
65	15.385	1.052	3.174E+00	1.078E+04	1.825E+14
70	14.286	1.061	2.335E+00	9.630E+03	2.776E+14
70	14.286	1.053	2.332E+00	9.622E+03	2.781E+14
75	13.333	1.053	1.913E+00	8.622E+03	3.784E+14
75	13.333	1.056	1.913E+00	8.597E+03	3.795E+14

TEMP	1000/T	RATIO	RESISTIVITY	MOBILITY	CONCENTRATION
77.3	12.928	1.053	1.763E+00	8.061E+03	4.391E+14
77.3	12.928	1.050	1.771E+00	8.153E+03	4.324E+14
80	12.500	1.073	1.665E+00	7.702E+03	4.868E+14
80	12.500	1.041	1.663E+00	7.643E+03	4.910E+14
85	11.765	1.060	1.535E+00	6.919E+03	5.864E+14
85	11.765	1.040	1.539E+00	7.010E+03	5.788E+14
90	11.111	1.048	1.487E+00	6.352E+03	6.610E+14
90	11.111	1.059	1.491E+00	6.408E+03	6.532E+14
95	10.526	1.062	1.476E+00	5.789E+03	7.306E+14
95	10.526	1.049	1.483E+00	5.766E+03	7.303E+14
100	10.000	1.048	1.488E+00	5.324E+03	7.877E+14
100	10.000	1.055	1.491E+00	5.362E+03	7.806E+14
110	9.091	1.061	1.572E+00	4.487E+03	8.850E+14
110	9.091	1.043	1.583E+00	4.478E+03	8.806E+14
120	8.333	1.049	1.725E+00	3.812E+03	9.494E+14
120	8.333	1.049	1.727E+00	3.827E+03	9.445E+14
130	7.692	1.056	1.950E+00	3.312E+03	9.664E+14
130	7.692	1.052	1.953E+00	3.297E+03	9.697E+14
140	7.143	1.056	2.184E+00	2.842E+03	1.006E+15
140	7.143	1.054	2.182E+00	2.824E+03	1.013E+15
160	6.250	1.055	2.791E+00	2.118E+03	1.056E+15
160	6.250	1.059	2.795E+00	2.062E+03	1.083E+15

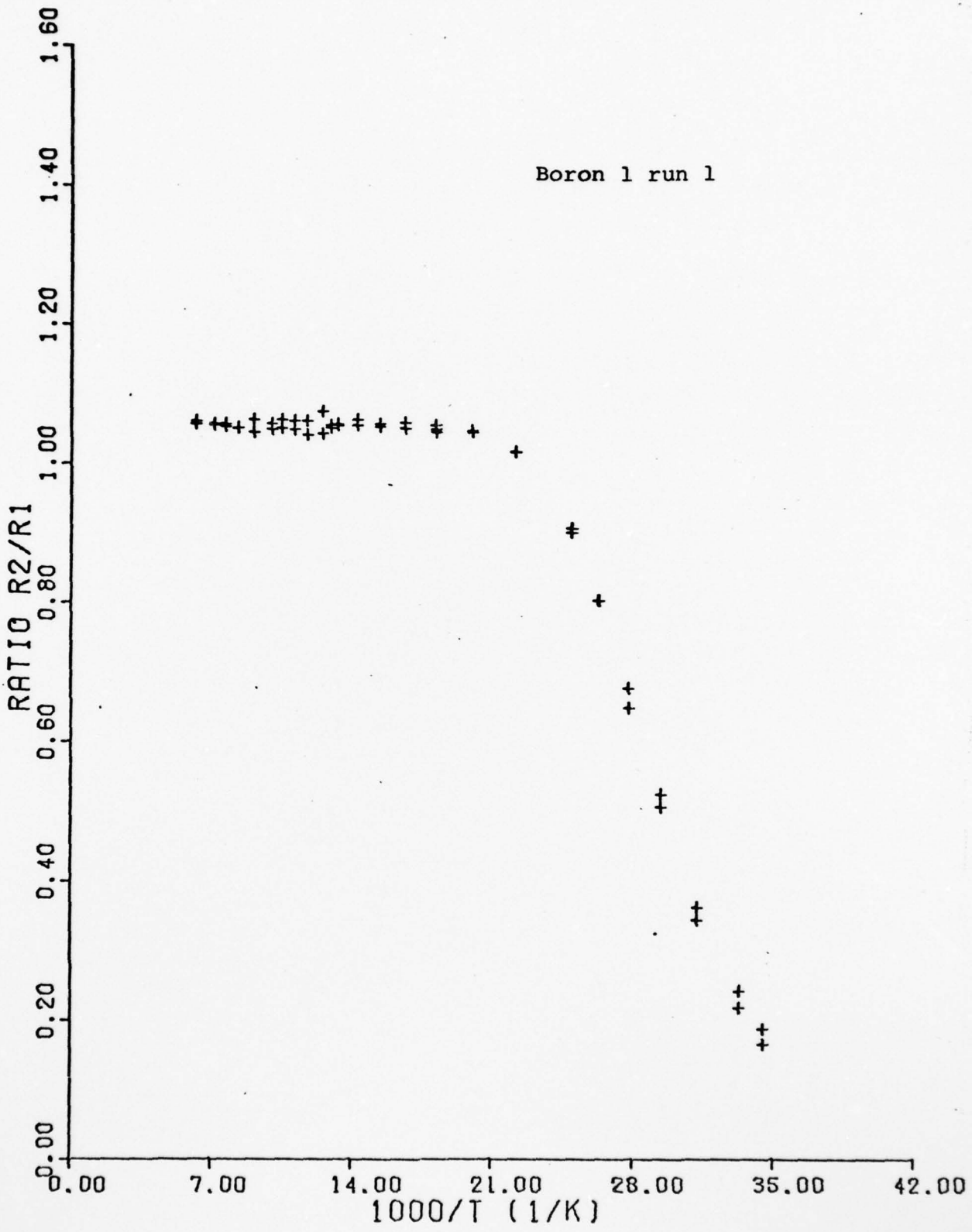

Figure A2 Resistivity Ratio versus 1000/T

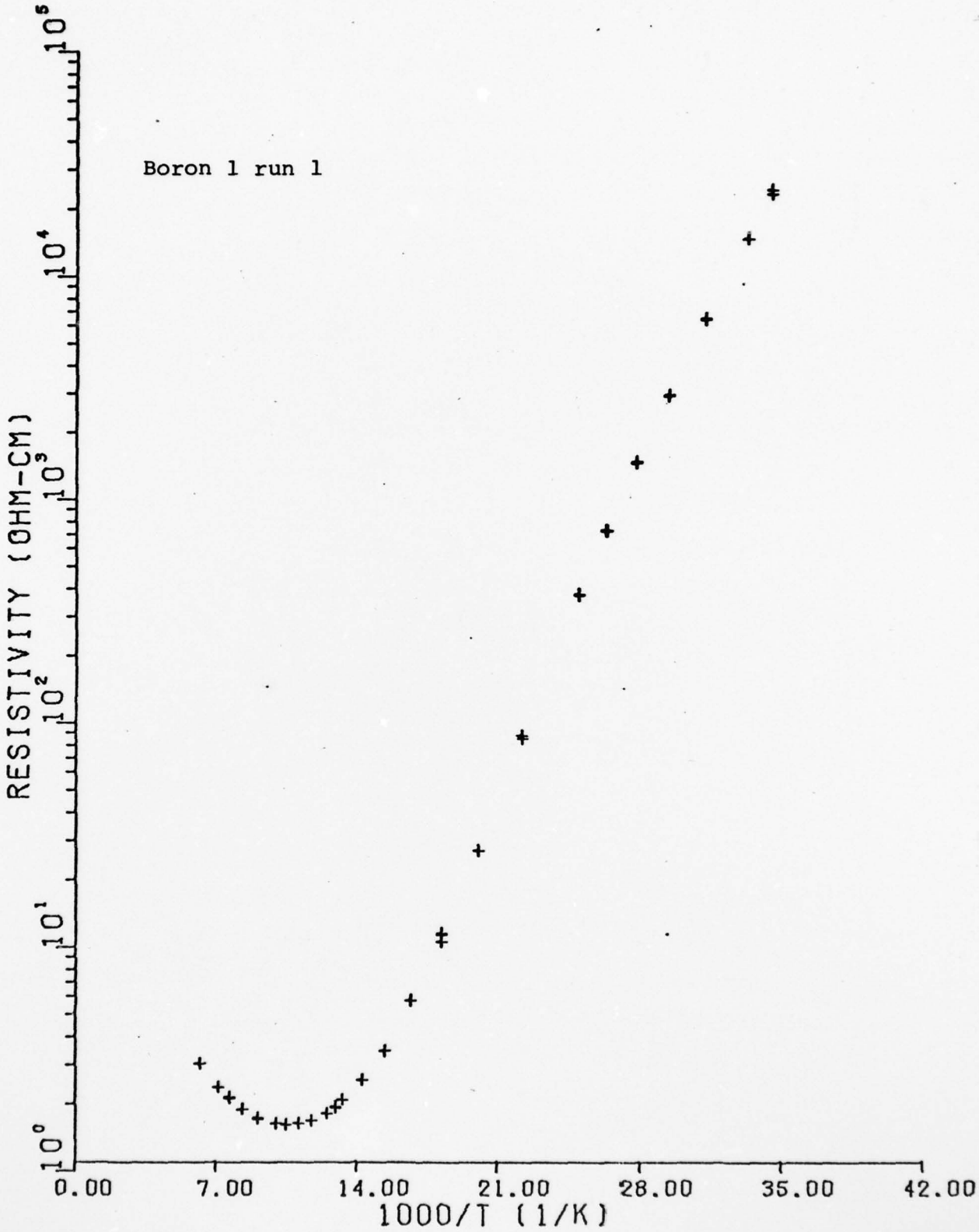

Figure A3 Resistivity versus 1000/T

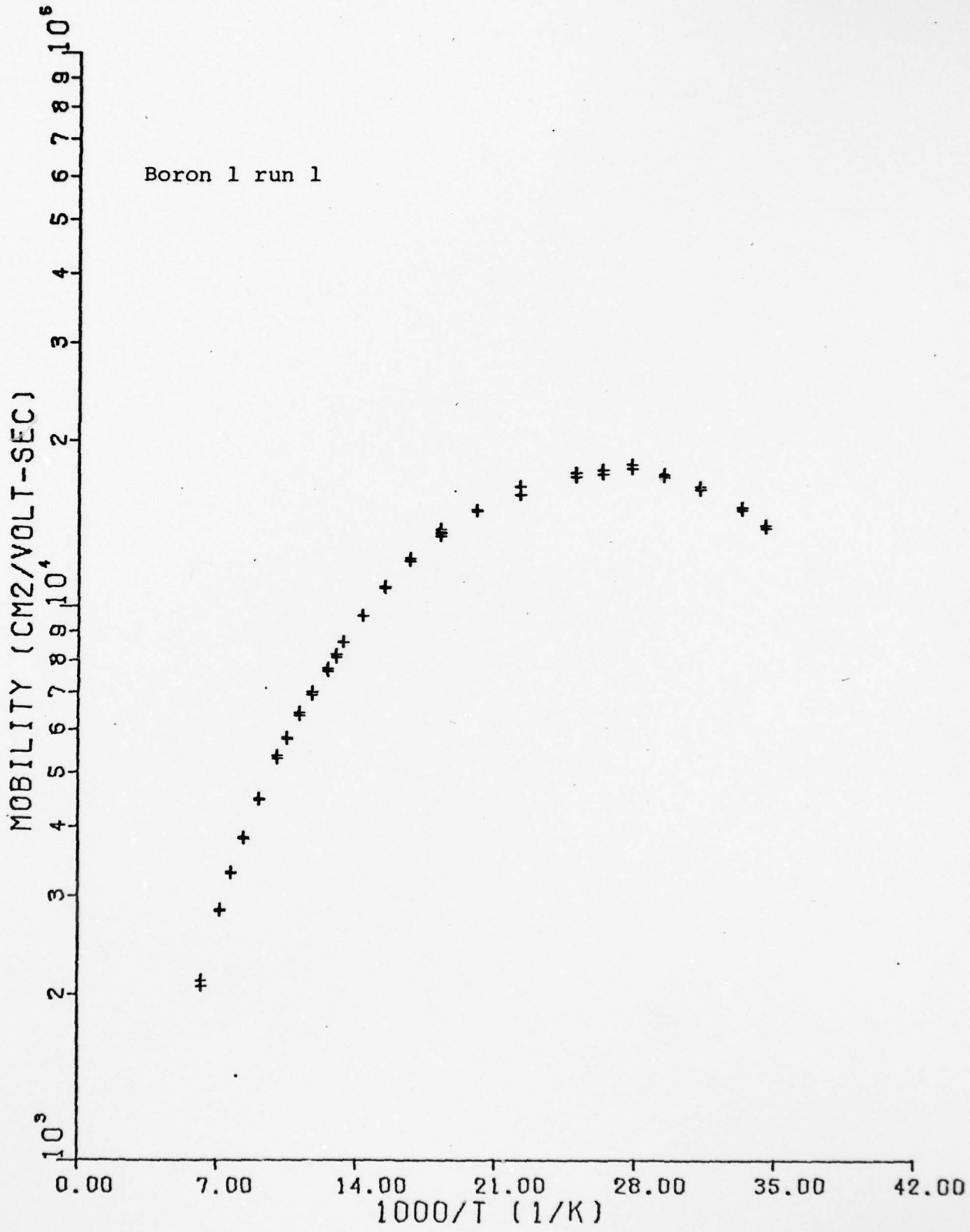

Figure A4 Mobility versus 1000/T

AD-A064 933 AIR FORCE INST OF TECH WRIGHT-PATTERSON AFB OHIO SCH--ETC F/G 20/12
INVESTIGATION OF WEB-DENDRITE SILICON.(U)
DEC 78 T J SETTECERRI

UNCLASSIFIED AFIT/GEO/PH/78D-4 NL

2 OF 2
AD
A064933

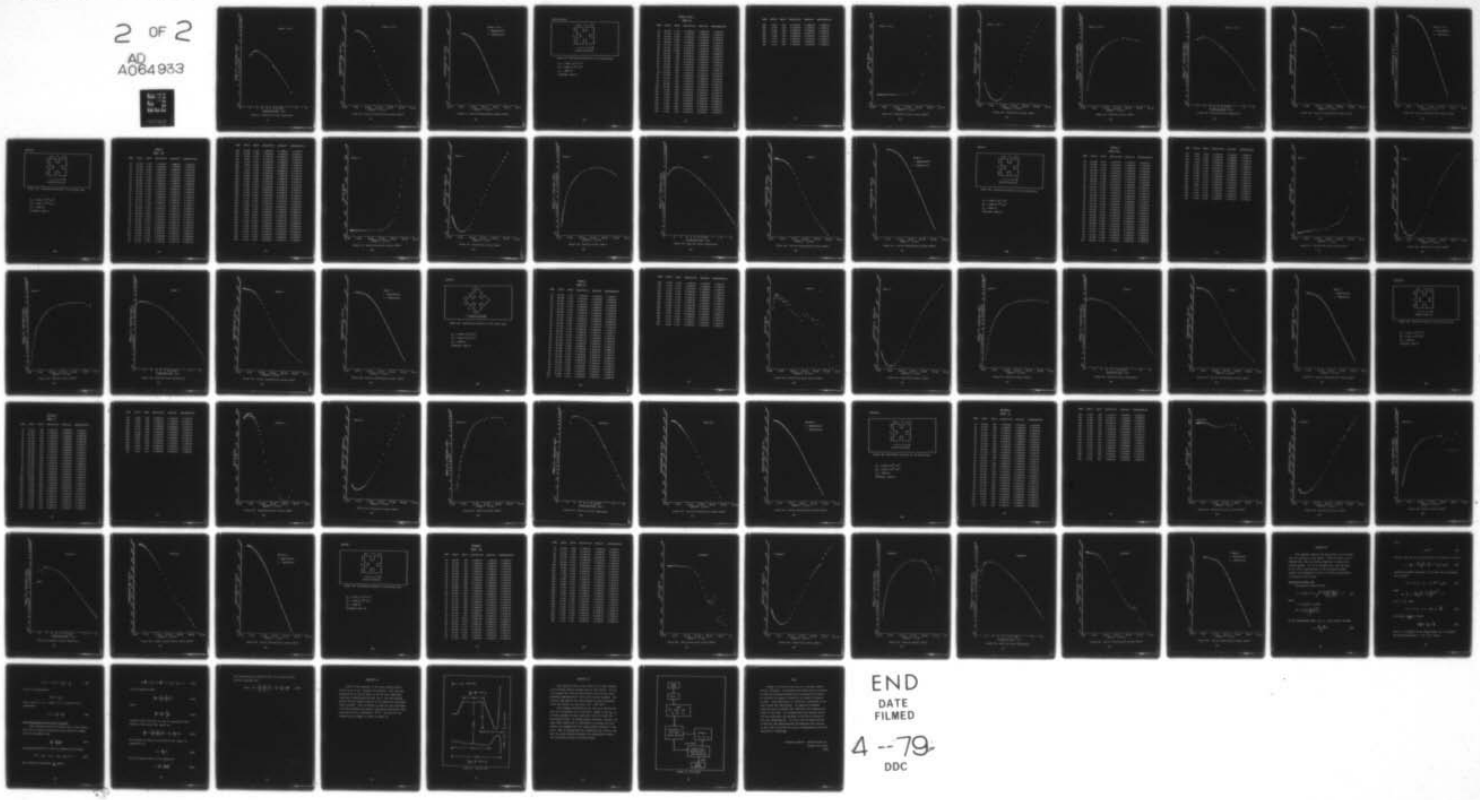

END
DATE
FILMED
4 -79
DDC

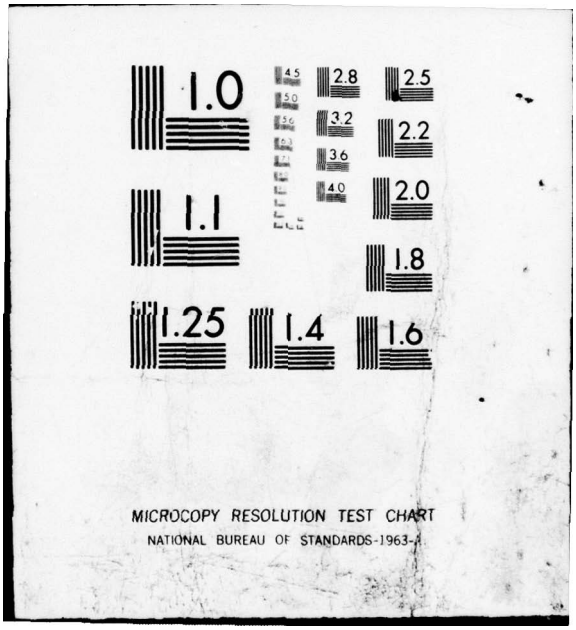
1.0
1.1
1.25
1.4
1.6
1.8
2.0
2.2
2.5
2.8
3.2
3.6
4.0
4.5
5.0
MICROCOPY RESOLUTION TEST CHART
NATIONAL BUREAU OF STANDARDS-1963-A

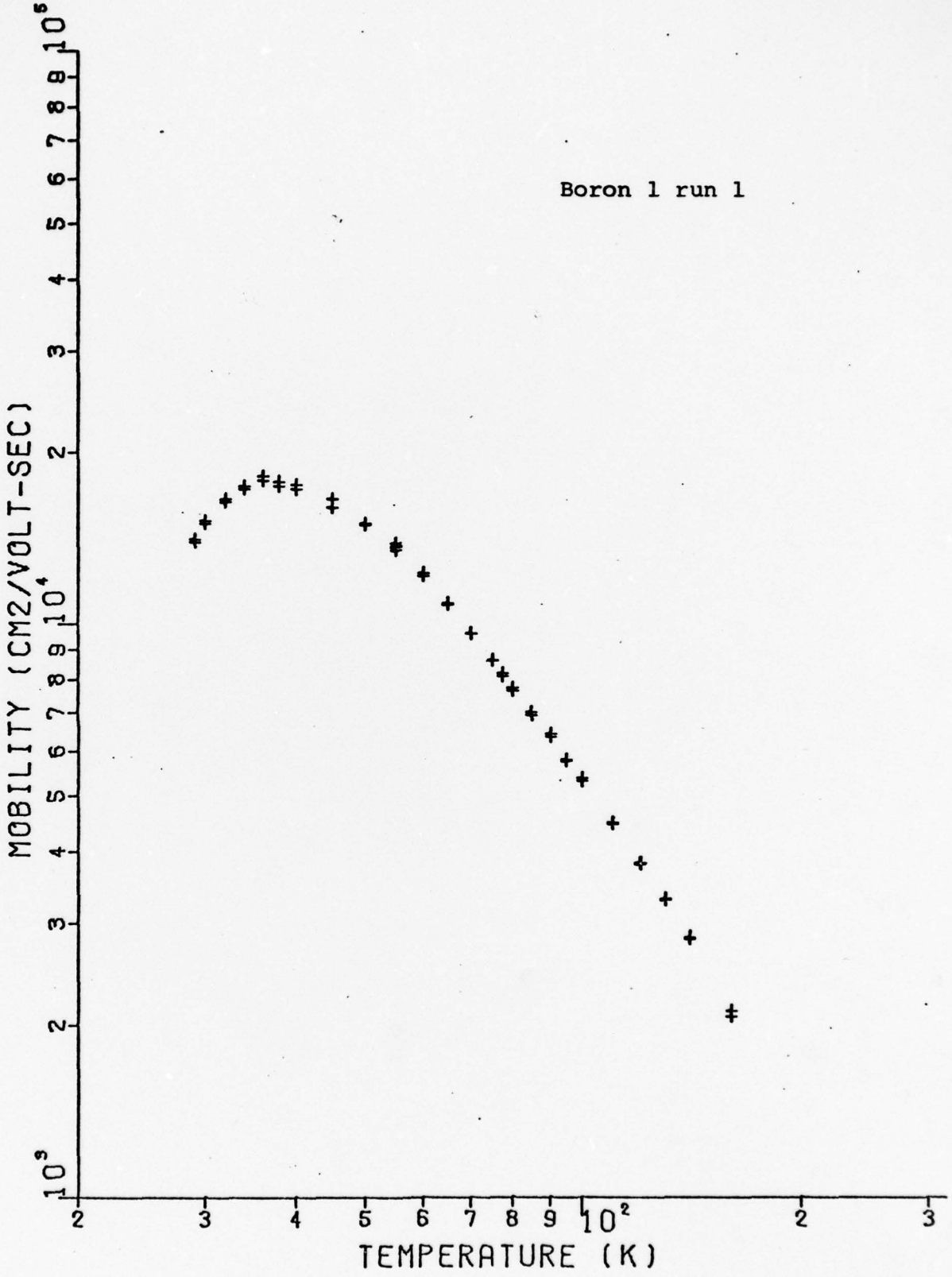

Figure A5 Mobility versus Temperature

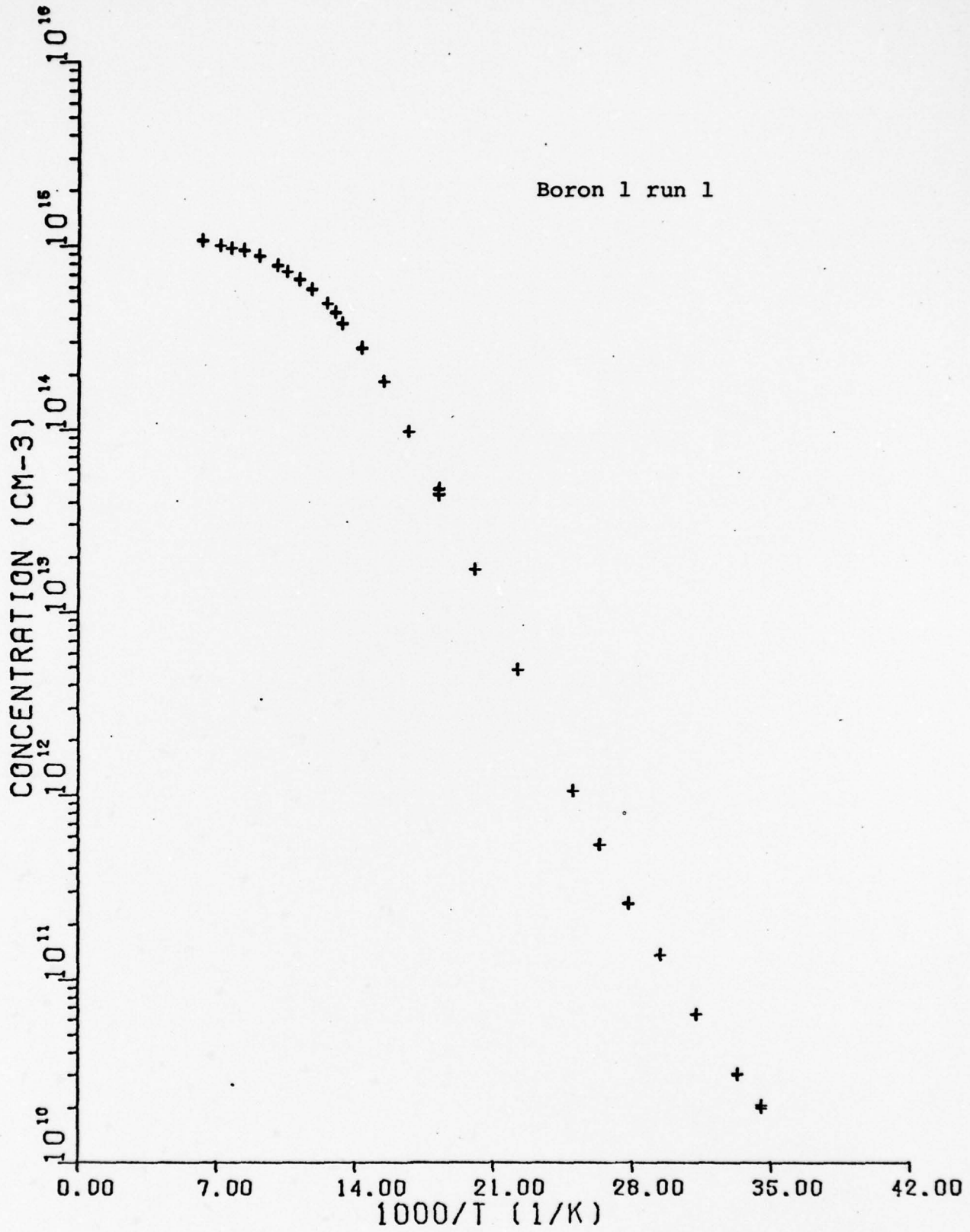

Figure A6 Carrier Concentration versus 1000/T

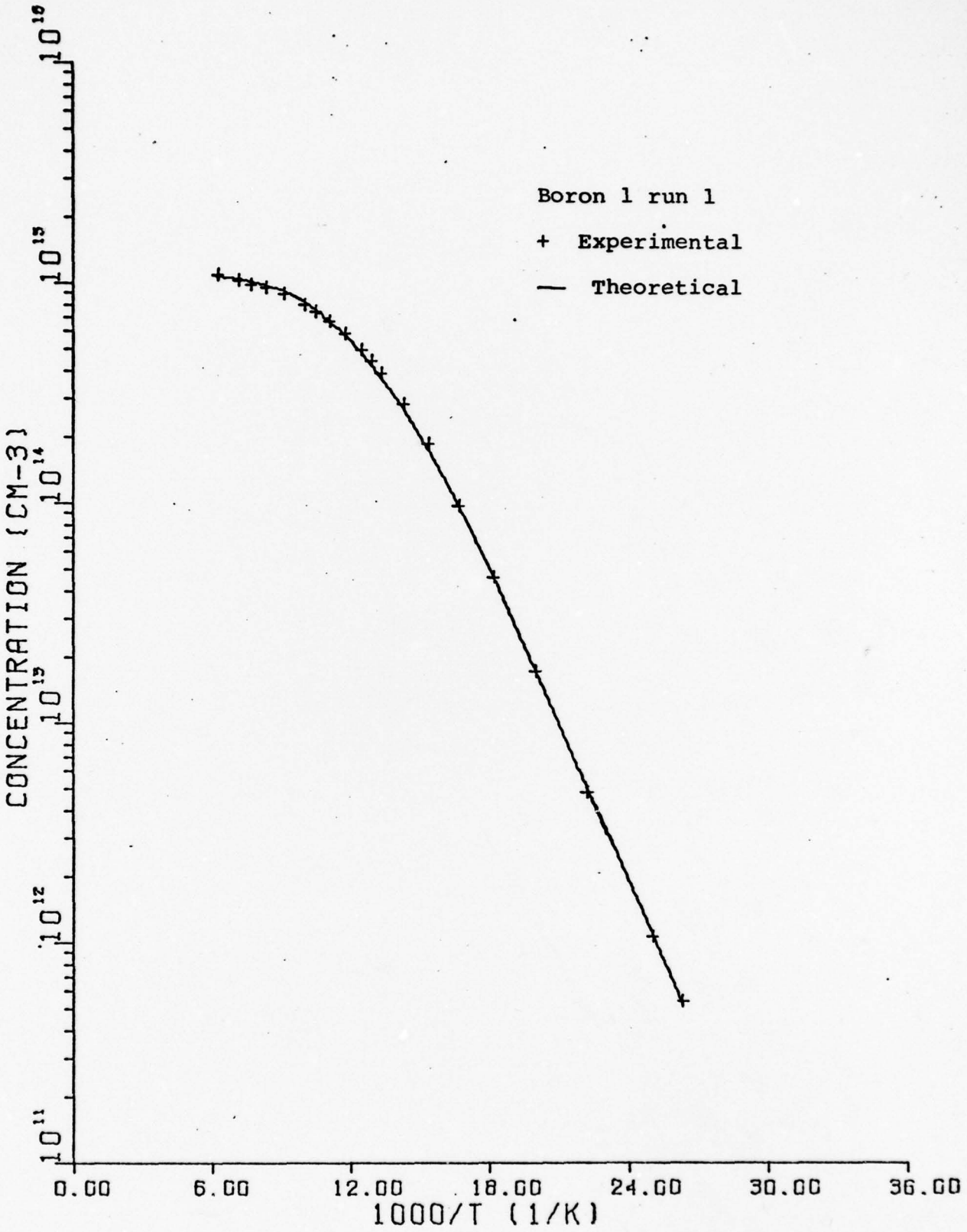

Figure A7 Carrier Concentration versus 1000/T

Boron 1 run 2

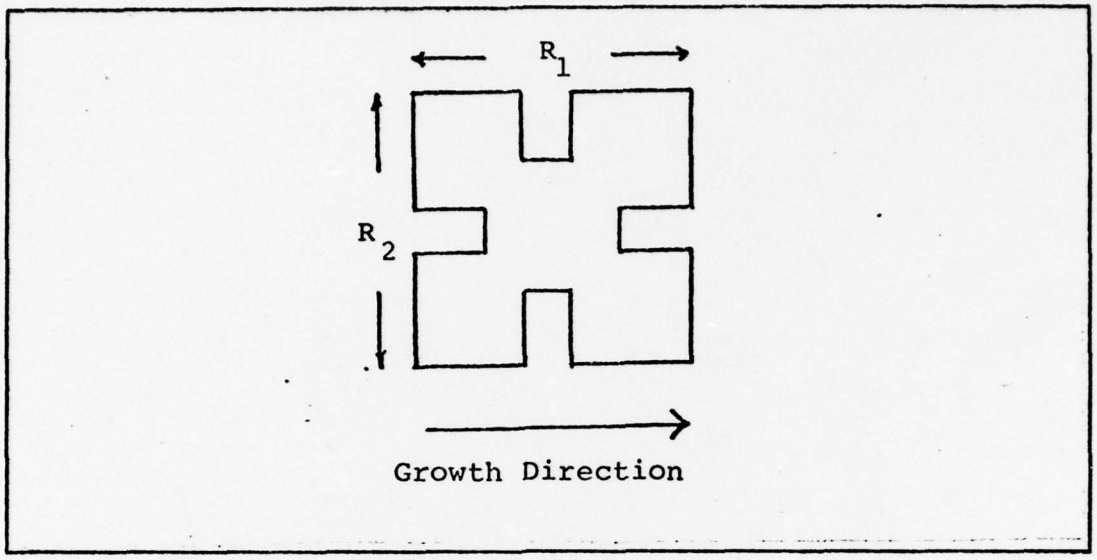

Figure A8 Resistances Relative to the Growth Axis

$N_a = 1.490 \times 10^{15}$ cm^{-3}

$N_d = 4.882 \times 10^{14}$ cm^{-3}

$\epsilon_a = .0426$ ev

thickness .022 cm

Boron 1 run 2

Table VI

TEMP	1000/T	RATIO	RESISTIVITY	MOBILITY	CONCENTRATION
28	35.714	7.971	3.387E+04	1.549E+04	1.190E+10
29	34.483	6.196	2.122E+04	1.572E+04	1.871E+10
30	33.333	4.630	1.293E+04	1.744E+04	2.768E+10
32	31.250	2.844	5.734E+03	1.751E+04	6.217E+10
34	29.412	1.937	2.584E+03	1.845E+04	1.309E+11
36	27.778	1.459	1.144E+03	1.937E+04	2.817E+11
38	26.316	1.194	5.560E+02	1.933E+04	5.808E+11
40	25.000	1.084	2.823E+02	1.895E+04	1.167E+12
45	22.222	.982	6.467E+01	1.756E+04	5.498E+12
50	20.000	.956	2.033E+01	1.607E+04	1.910E+13
55	18.182	.956	8.412E+00	1.449E+04	5.122E+13
60	16.667	.947	4.506E+00	1.306E+04	1.060E+14
65	15.385	.949	2.930E+00	1.164E+04	1.830E+14
70	14.286	.950	2.207E+00	1.041E+04	2.717E+14
75	13.333	.947	1.833E+00	9.287E+03	3.668E+14
77.3	12.928	.957	1.684E+00	8.754E+03	4.233E+14
80	12.500	.953	1.606E+00	8.295E+03	4.686E+14
85	11.765	.947	1.504E+00	7.490E+03	5.541E+14
90	11.111	.952	1.456E+00	6.792E+03	6.310E+14
95	10.526	.953	1.437E+00	6.268E+03	6.931E+14
100	10.000	.949	1.465E+00	5.644E+03	7.549E+14
110	9.091	.958	1.558E+00	4.857E+03	8.249E+14
120	8.333	.950	1.686E+00	4.236E+03	8.738E+14
130	7.692	.943	1.925E+00	3.547E+03	9.143E+14
140	7.143	.959	2.143E+00	3.00eE+03	9.690E+14
150	6.667	.945	2.429E+00	2.604E+03	9.869E+14
160	6.250	.951	2.812E+00	2.274E+03	9.762E+14
170	5.882	.949	3.196E+00	1.977E+03	9.878E+14
180	5.556	.950	3.612E+00	1.687E+03	1.025E+15
180	5.556	.953	3.567E+00	1.441E+03	1.215E+15

TEMP	1000/T	RATIO	RESISTIVITY	MOBILITY	CONCENTRATION
190	5.263	.944	4.115E+00	1.298E+03	1.168E+15
200	5.000	.942	4.633E+00	1.153E+03	1.168E+15
220	4.545	.944	5.843E+00	8.878E+02	1.203E+15
240	4.167	.944	7.261E+00	6.825E+02	1.260E+15
260	3.846	.951	8.858E+00	5.658E+02	1.245E+15
280	3.571	.954	1.069E+01	4.615E+02	1.265E+15
300	3.333	.952	1.249E+01	3.843E+02	1.300E+15
320	3.125	.952	1.455E+01	3.434E+02	1.249E+15

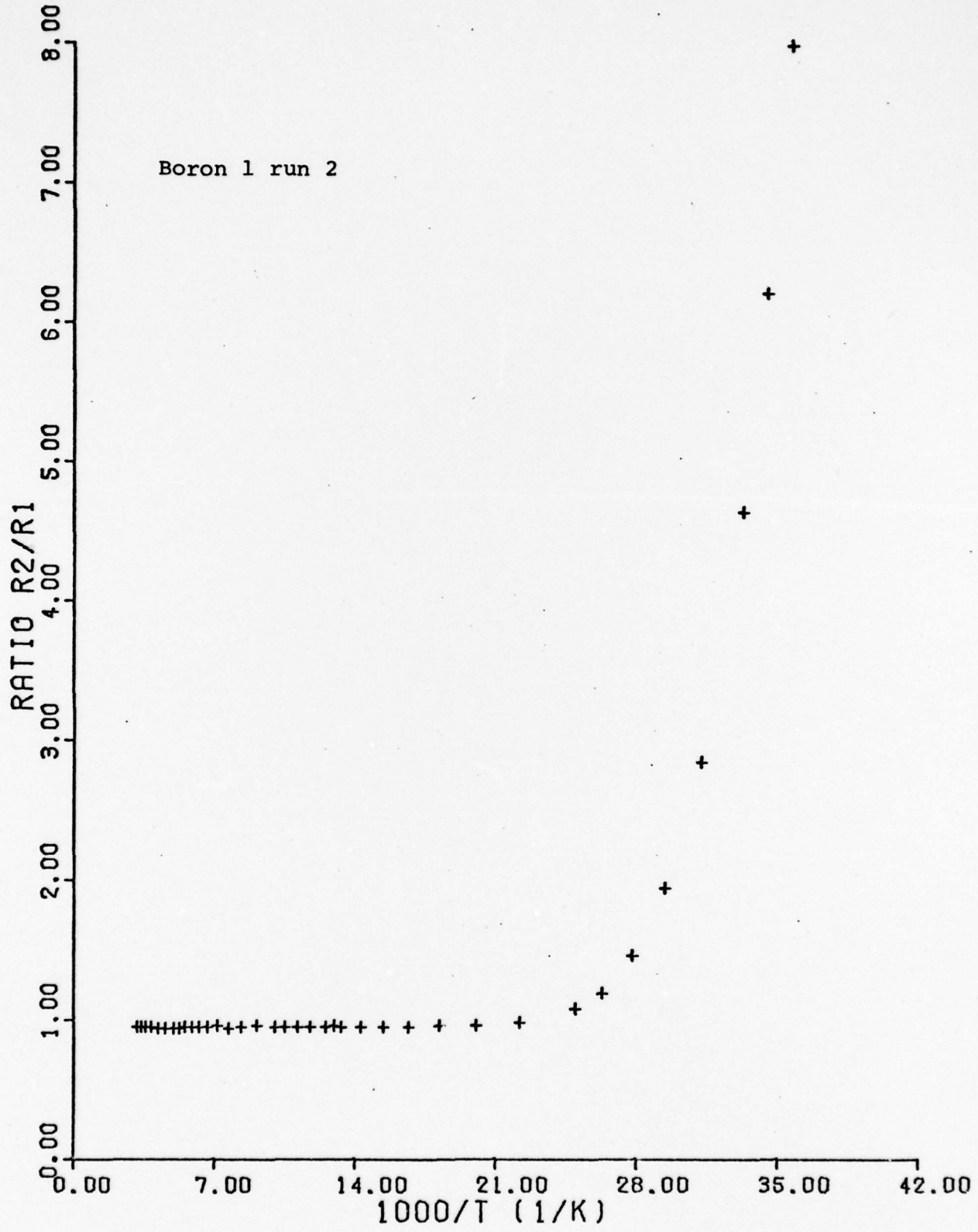

Figure A9 Resistivity Ratio versus 1000/T

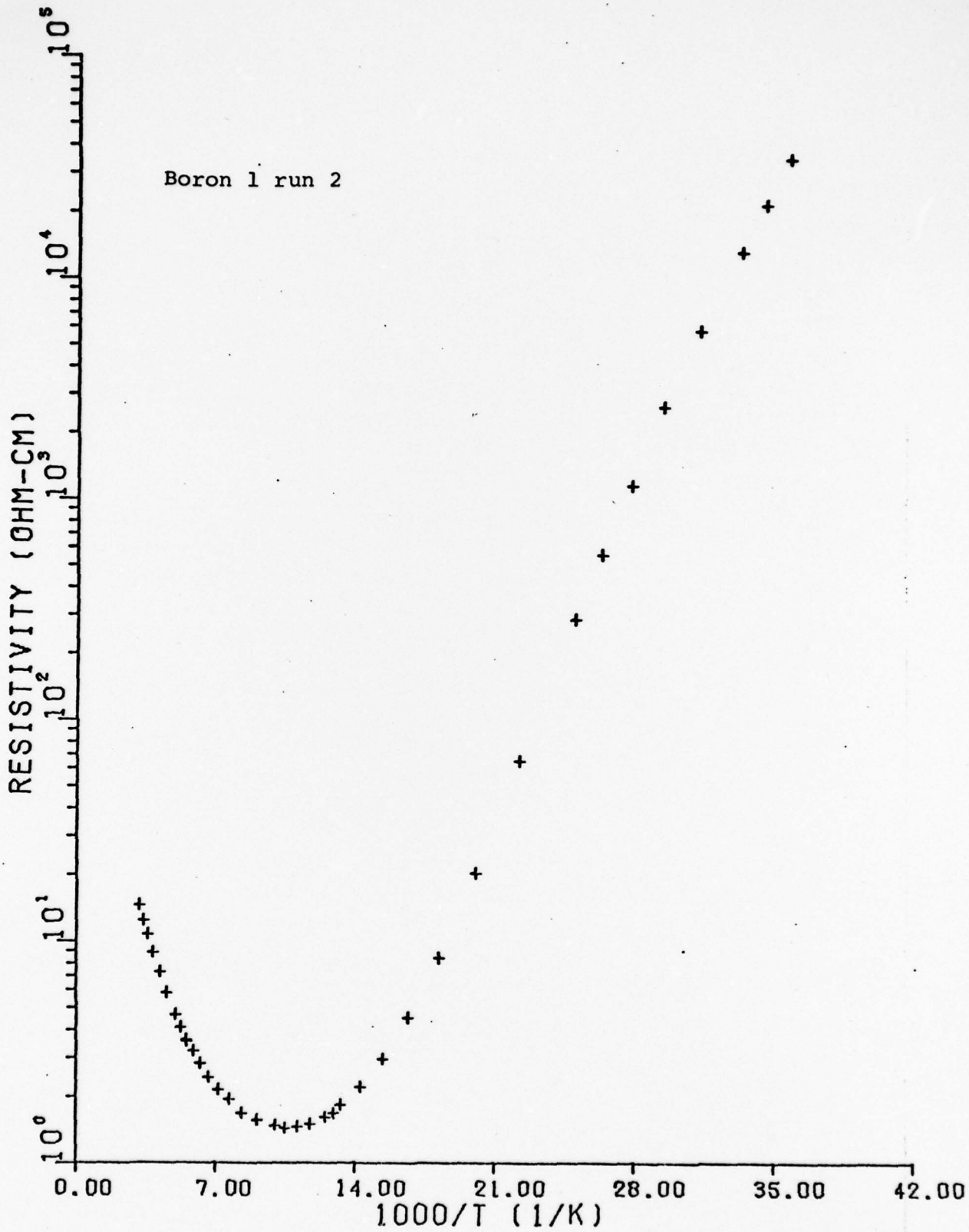

Figure A10 Resistivity versus 1000/T

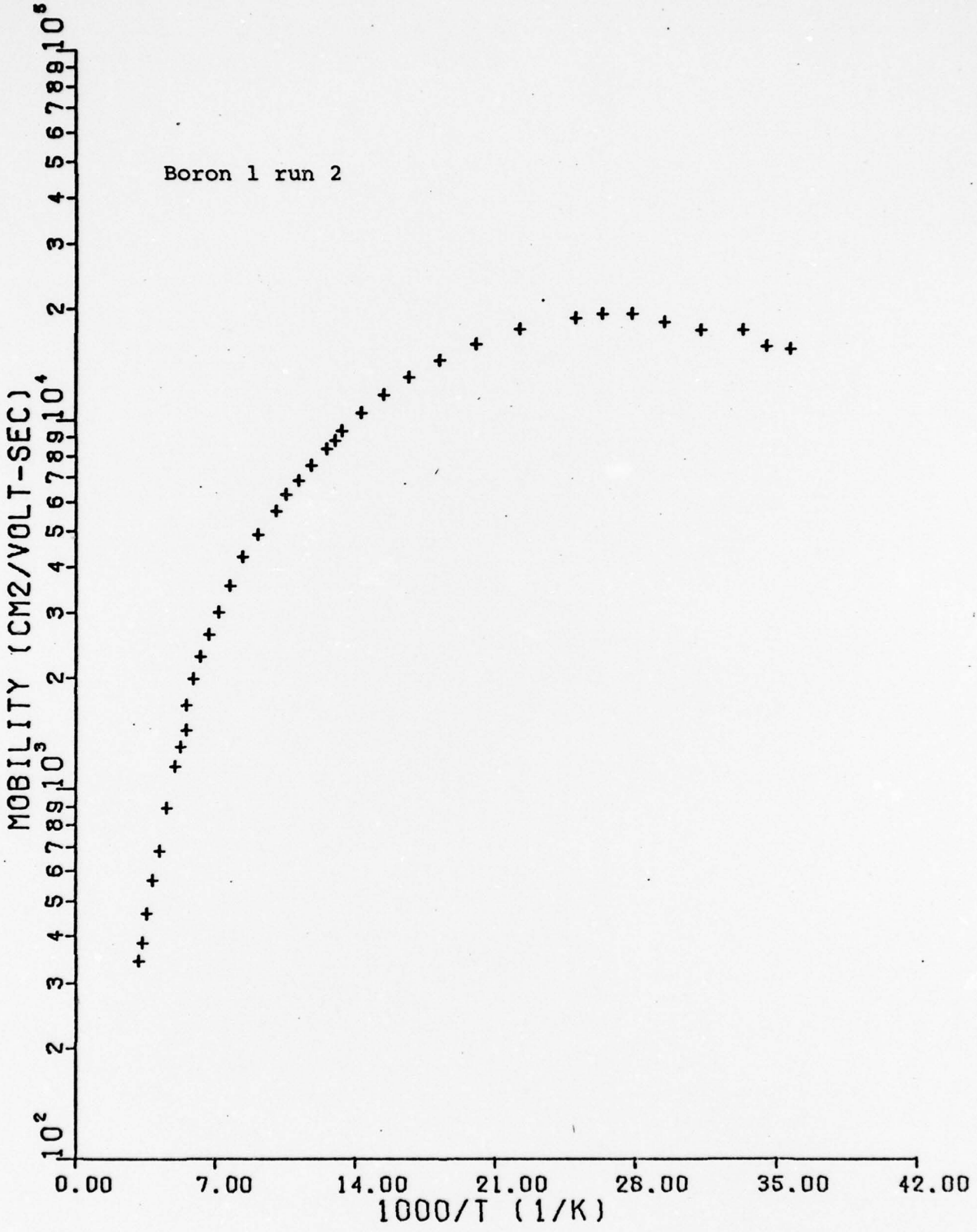

Figure A11 Mobility versus 1000/T

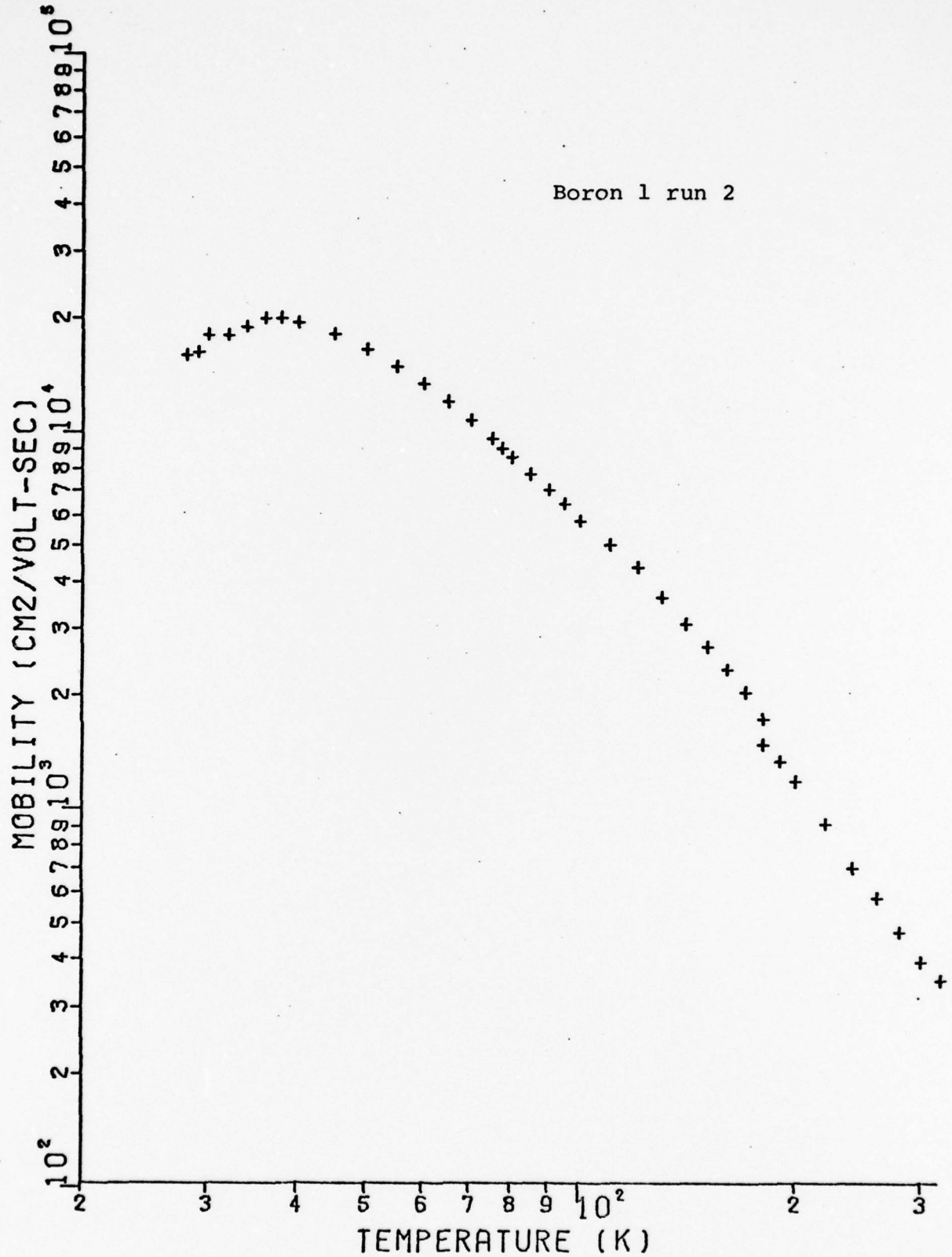

Figure A12 Mobility versus Temperature

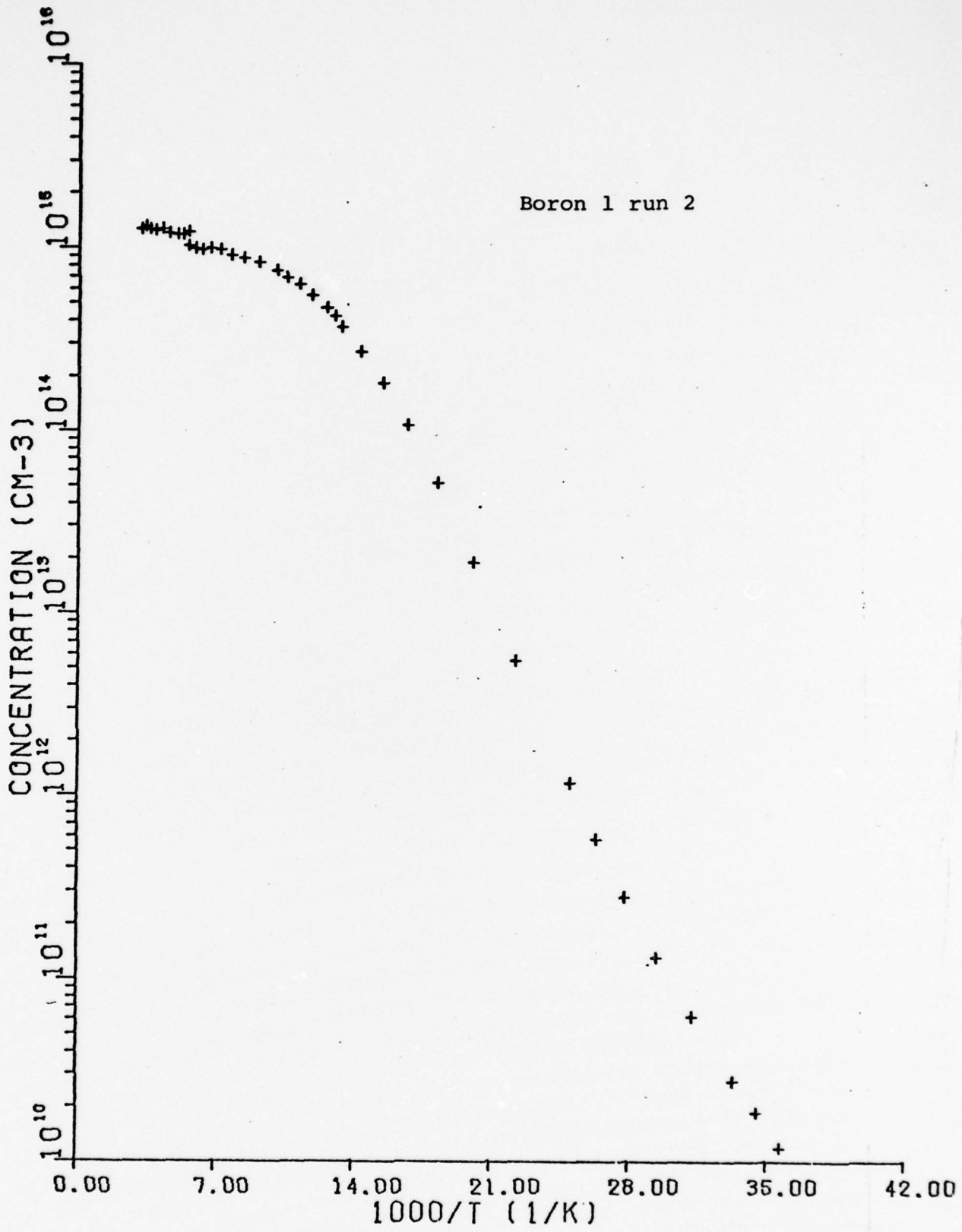

Figure A13 Carrier Concentration versus 1000/T

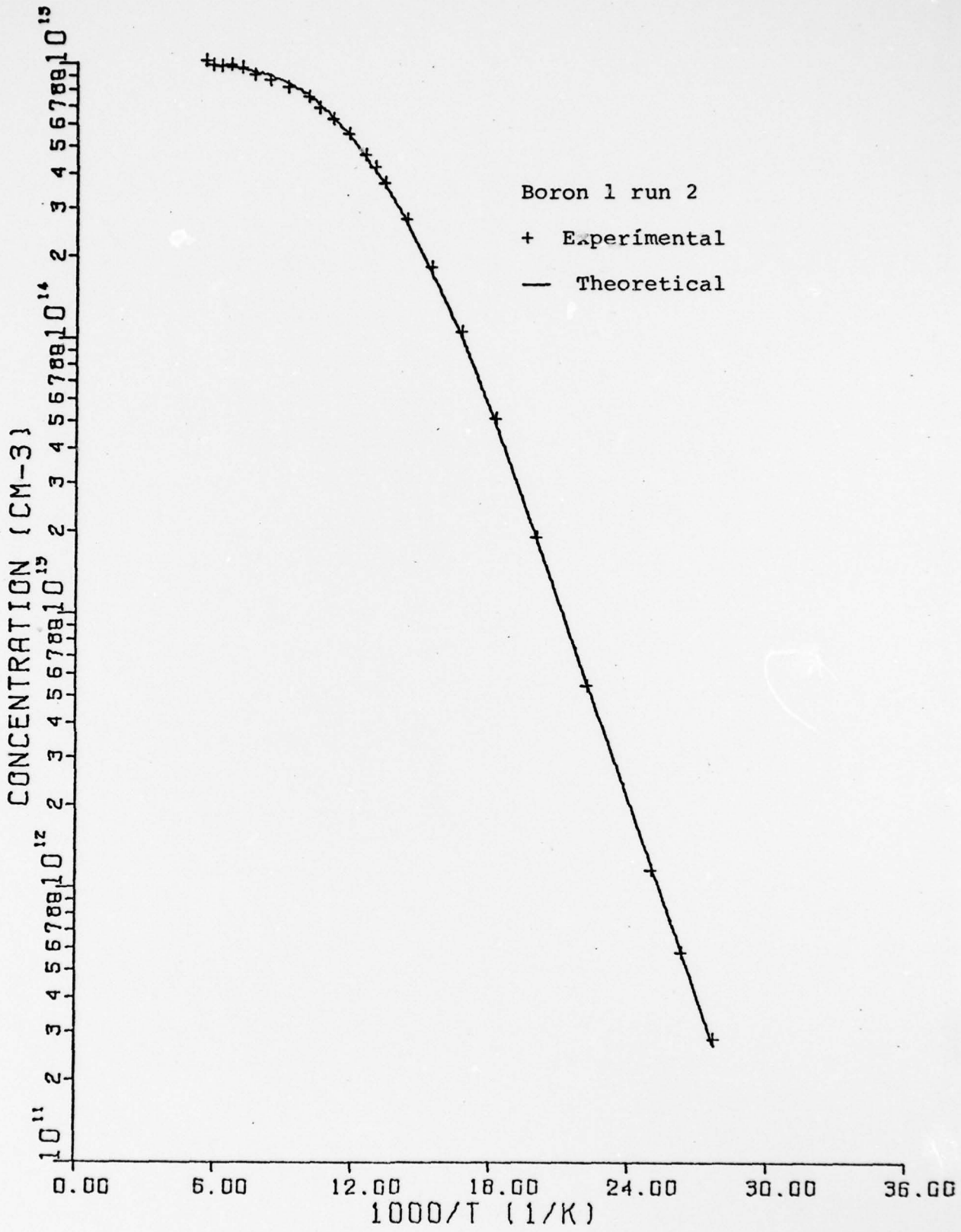

Figure A14 Carrier Concentration versus 1000/T

Boron 2

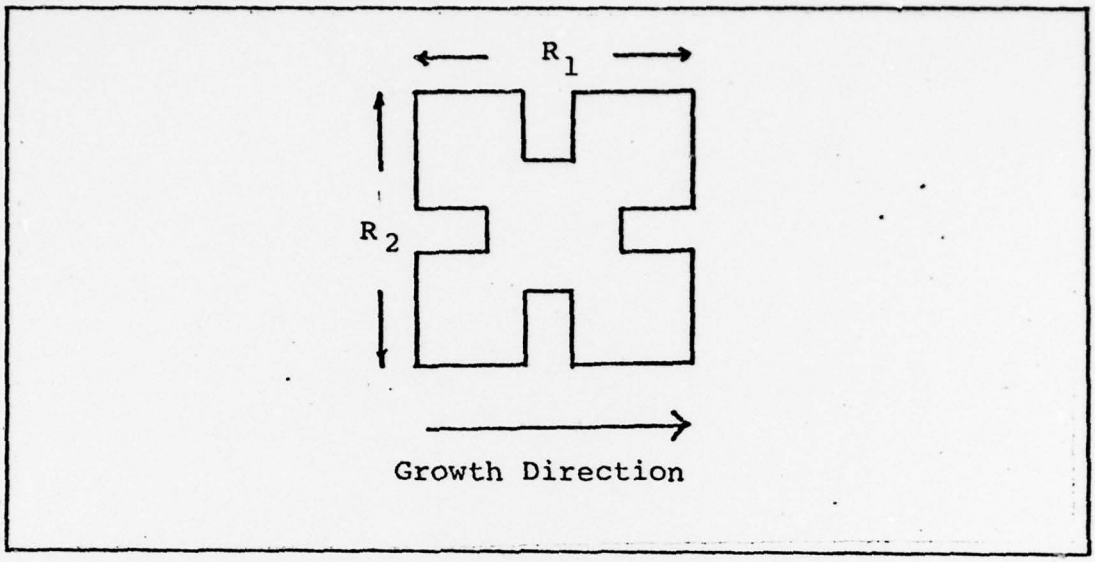

Figure A15 Resistances Relative to the Growth Axis

$N_a = 1.099 \times 10^{15}$ cm^{-3}

$N_d = 2.841 \times 10^{14}$ cm^{-3}

$\epsilon_a = .0443$ ev

thickness .022 cm

Boron 2

Table VII

TEMP	1000/T	RATIO	RESISTIVITY	MOBILITY	CONCENTRATION
22	45.455	3.524	3.235E+06	1.048E+04	1.842E+08
22	45.455	3.340	3.382E+06	1.135E+04	1.627E+08
23	43.478	2.833	1.464E+06	1.226E+04	3.477E+08
23	43.478	2.635	1.691E+06	1.211E+04	3.047E+08
24	41.667	2.304	7.655E+05	1.367E+04	5.964E+08
24	41.667	2.269	8.846E+05	1.413E+04	4.994E+08
25	40.000	1.885	4.654E+05	1.483E+04	9.044E+08
26	38.462	1.678	2.495E+05	1.670E+04	1.498E+09
27	37.037	1.465	1.327E+05	1.721E+04	2.734E+09
28	35.714	1.359	7.871E+04	1.809E+04	4.384E+09
29	34.483	1.259	4.461E+04	1.836E+04	7.621E+09
30	33.333	1.169	2.599E+04	1.844E+04	1.275E+10
32	31.250	1.103	1.005E+04	1.897E+04	3.275E+10
34	29.412	1.071	3.951E+03	1.888E+04	8.366E+10
36	27.778	1.048	1.605E+03	1.839E+04	2.116E+11
38	26.316	1.042	7.311E+02	1.798E+04	4.748E+11
40	25.000	1.031	3.603E+02	1.738E+04	9.966E+11
45	22.222	1.021	7.561E+01	1.600E+04	5.160E+12
50	20.000	1.023	2.337E+01	1.483E+04	1.802E+13
55	18.182	1.020	1.007E+01	1.316E+04	4.711E+13
60	16.667	1.020	5.596E+00	1.178E+04	9.473E+13
65	15.385	1.017	3.756E+00	1.045E+04	1.590E+14
70	14.286	1.017	2.865E+00	9.366E+03	2.334E+14
75	13.333	1.020	2.402E+00	8.227E+03	3.159E+14
77.3	12.928	1.020	2.266E+00	7.812E+03	3.527E+14
80	12.500	1.018	2.157E+00	7.431E+03	3.894E+14
85	11.765	1.022	2.026E+00	6.714E+03	4.566E+14
90	11.111	1.021	1.978E+00	6.047E+03	5.220E+14
95	10.526	1.018	1.971E+00	5.547E+03	5.709E+14

TEMP	1000/T	RATIO	RESISTIVITY	MOBILITY	CONCENTRATION
100	10.000	1.019	1.995E+00	5.116E+03	6.115E+14
100	10.000	1.018	1.990E+00	5.147E+03	6.096E+14
110	9.091	1.021	2.135E+00	4.305E+03	6.790E+14
110	9.091	1.017	2.132E+00	4.271E+03	6.856E+14
120	8.333	1.013	2.344E+00	3.665E+03	7.270E+14
130	7.692	1.019	2.623E+00	3.119E+03	7.630E+14
140	7.143	1.019	2.968E+00	2.637E+03	7.975E+14
150	6.667	1.020	3.371E+00	2.298E+03	8.059E+14
160	6.250	1.018	3.844E+00	1.962E+03	8.275E+14
170	5.882	1.019	4.378E+00	1.736E+03	8.312E+14
180	5.556	1.016	4.968E+00	1.469E+03	8.553E+14
190	5.263	1.018	5.631E+00	1.305E+03	8.491E+14
200	5.000	1.019	6.371E+00	1.137E+03	8.617E+14
210	4.762	1.015	7.165E+00	9.951E+02	8.755E+14
220	4.545	1.017	8.045E+00	8.797E+02	8.820E+14
230	4.348	1.020	8.997E+00	7.832E+02	8.859E+14
230	4.348	1.019	9.061E+00	7.891E+02	8.730E+14
240	4.167	1.016	1.001E+01	6.971E+02	8.945E+14
240	4.167	1.020	1.007E+01	7.018E+02	8.832E+14
250	4.000	1.017	1.109E+01	6.151E+02	9.149E+14
250	4.000	1.016	1.116E+01	6.286E+02	8.902E+14
260	3.846	1.019	1.225E+01	5.336E+02	9.550E+14
260	3.846	1.018	1.228E+01	5.600E+02	9.080E+14
270	3.704	1.013	1.345E+01	5.112E+02	9.080E+14
280	3.571	1.017	1.471E+01	4.637E+02	9.153E+14
290	3.448	1.014	1.597E+01	4.220E+02	9.265E+14
300	3.333	1.017	1.728E+01	3.852E+02	9.380E+14
310	3.226	1.016	1.872E+01	3.452E+02	9.658E+14
320	3.125	1.019	2.015E+01	3.234E+02	9.578E+14
330	3.030	1.017	2.172E+01	2.975E+02	9.659E+14
340	2.941	1.019	2.328E+01	2.764E+02	9.700E+14
360	2.778	1.022	3.011E+01	1.949E+02	1.064E+15
380	2.632	1.019	2.657E+01	2.349E+02	1.000E+15

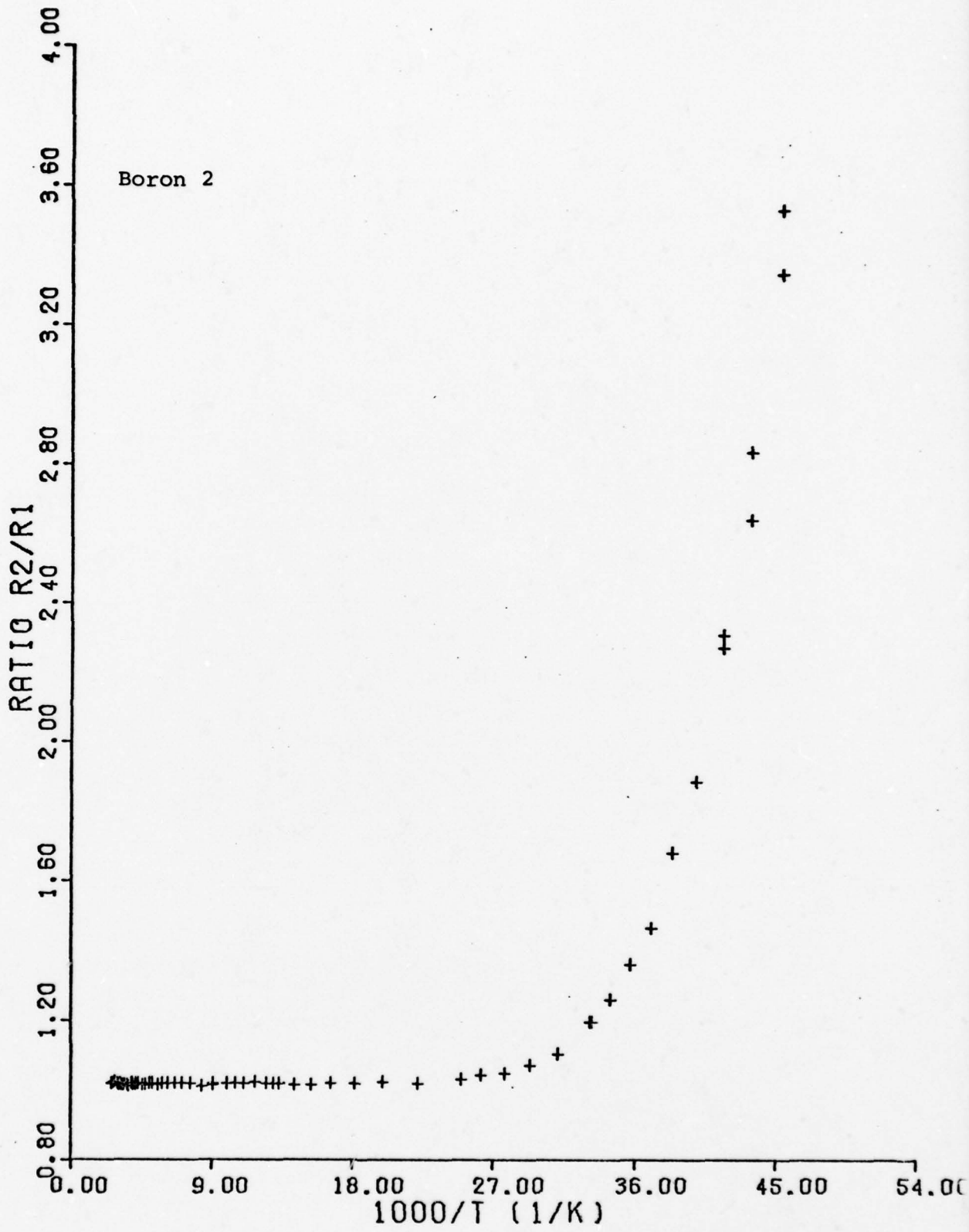

Figure A16 Resistivity Ratio versus 1000/T

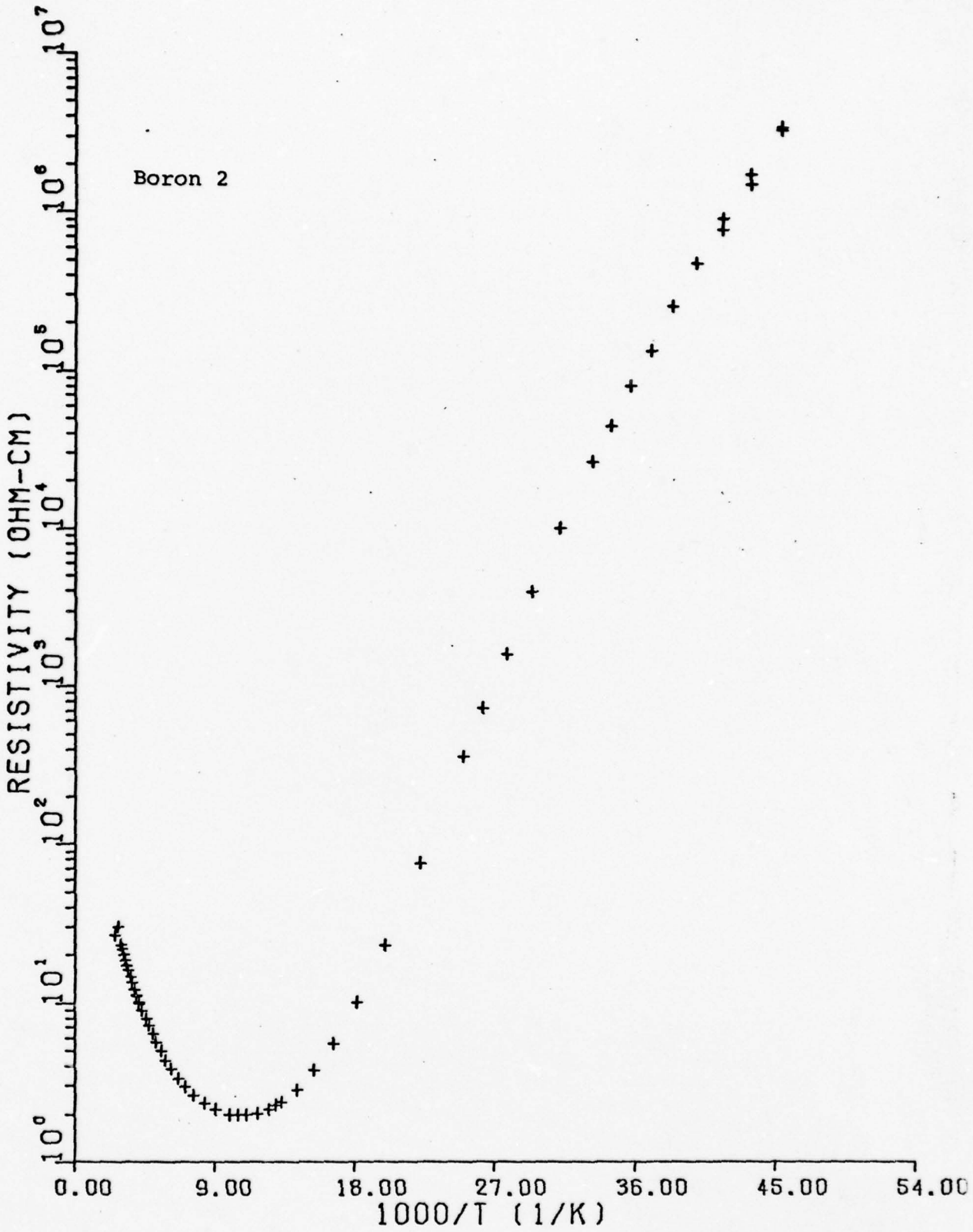

Figure A17 Resistivity versus 1000/T

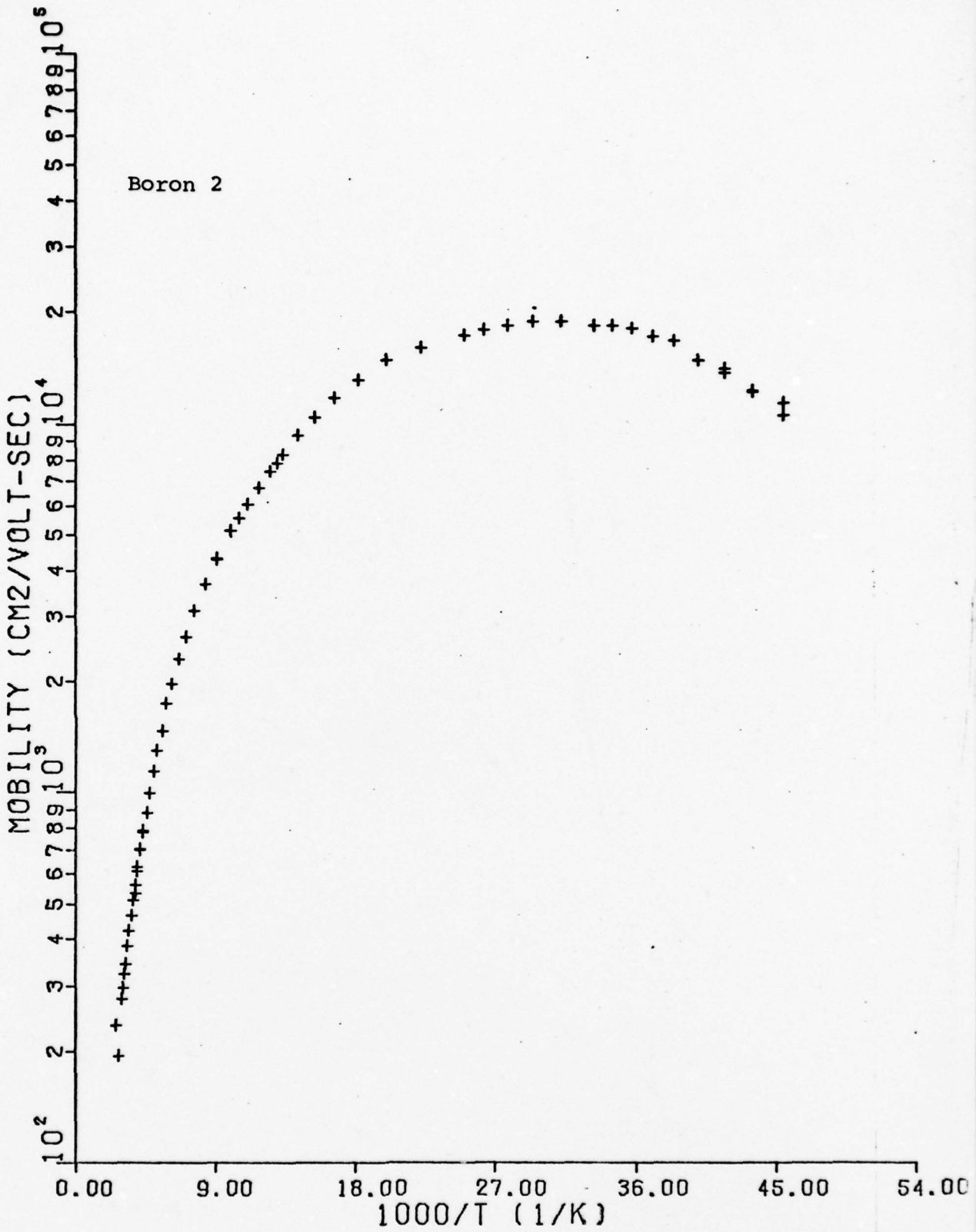

Figure A18 Mobility versus 1000/T

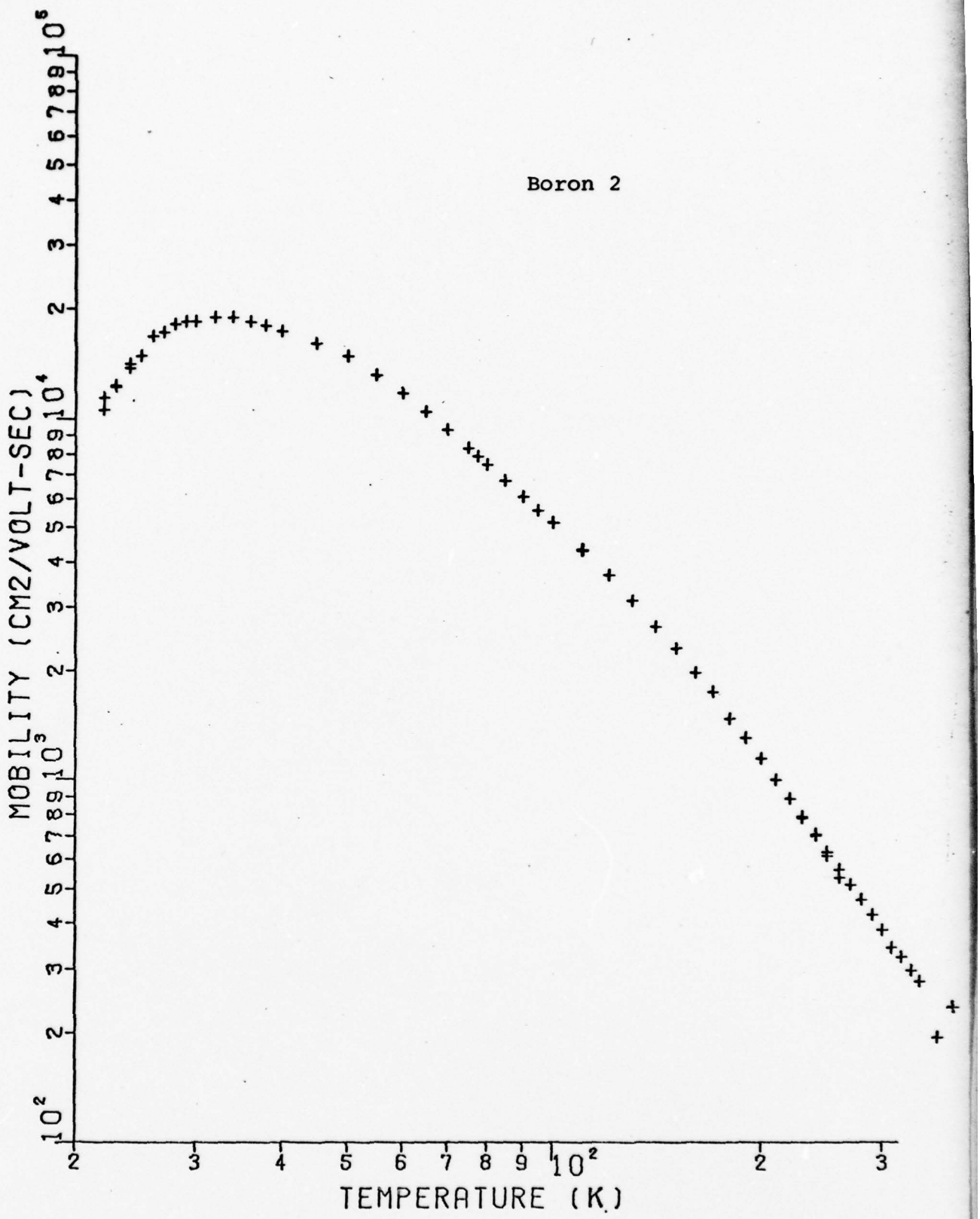

Figure A19 Mobility versus Temperature

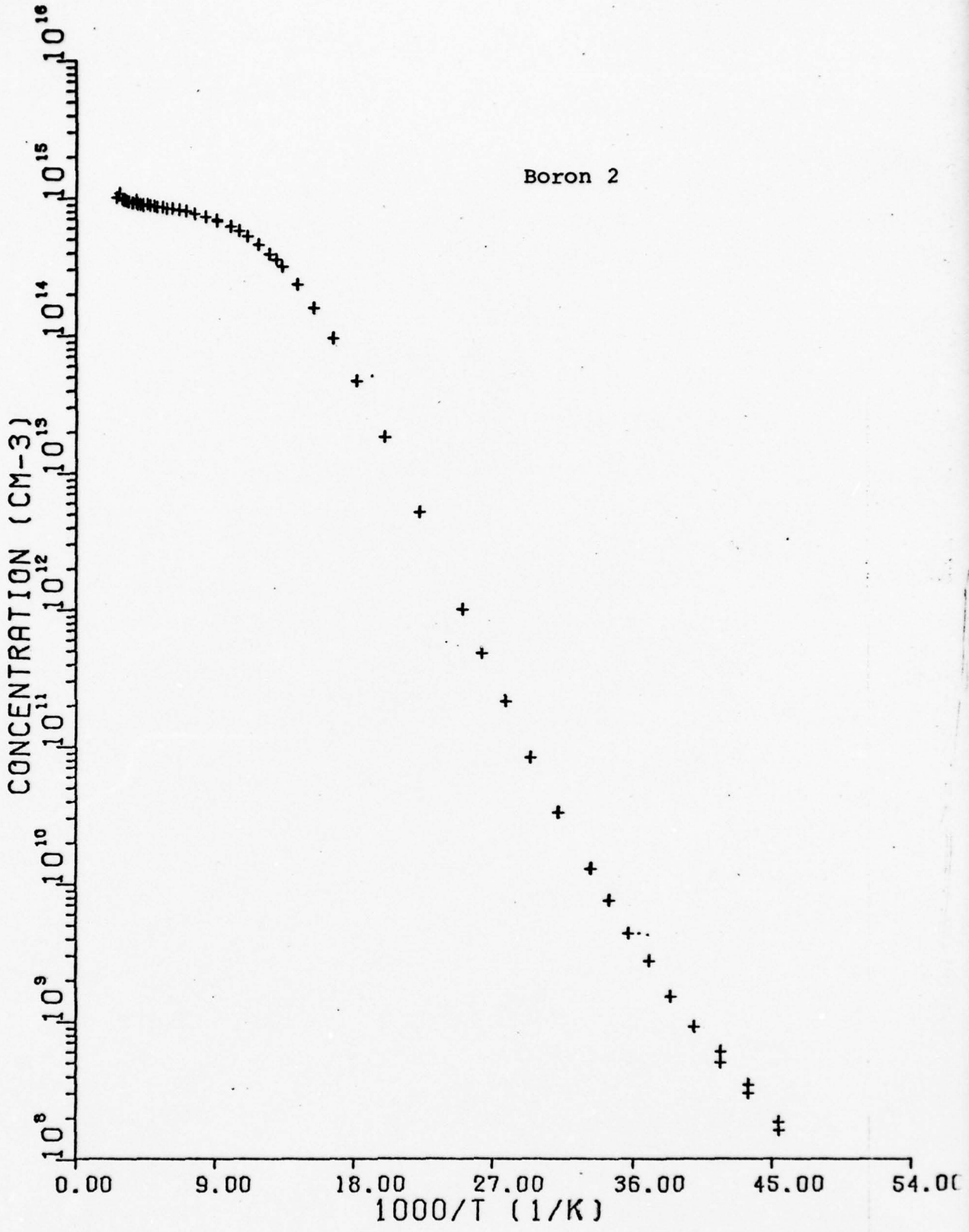

Figure A20 Carrier Concentration versus 1000/T

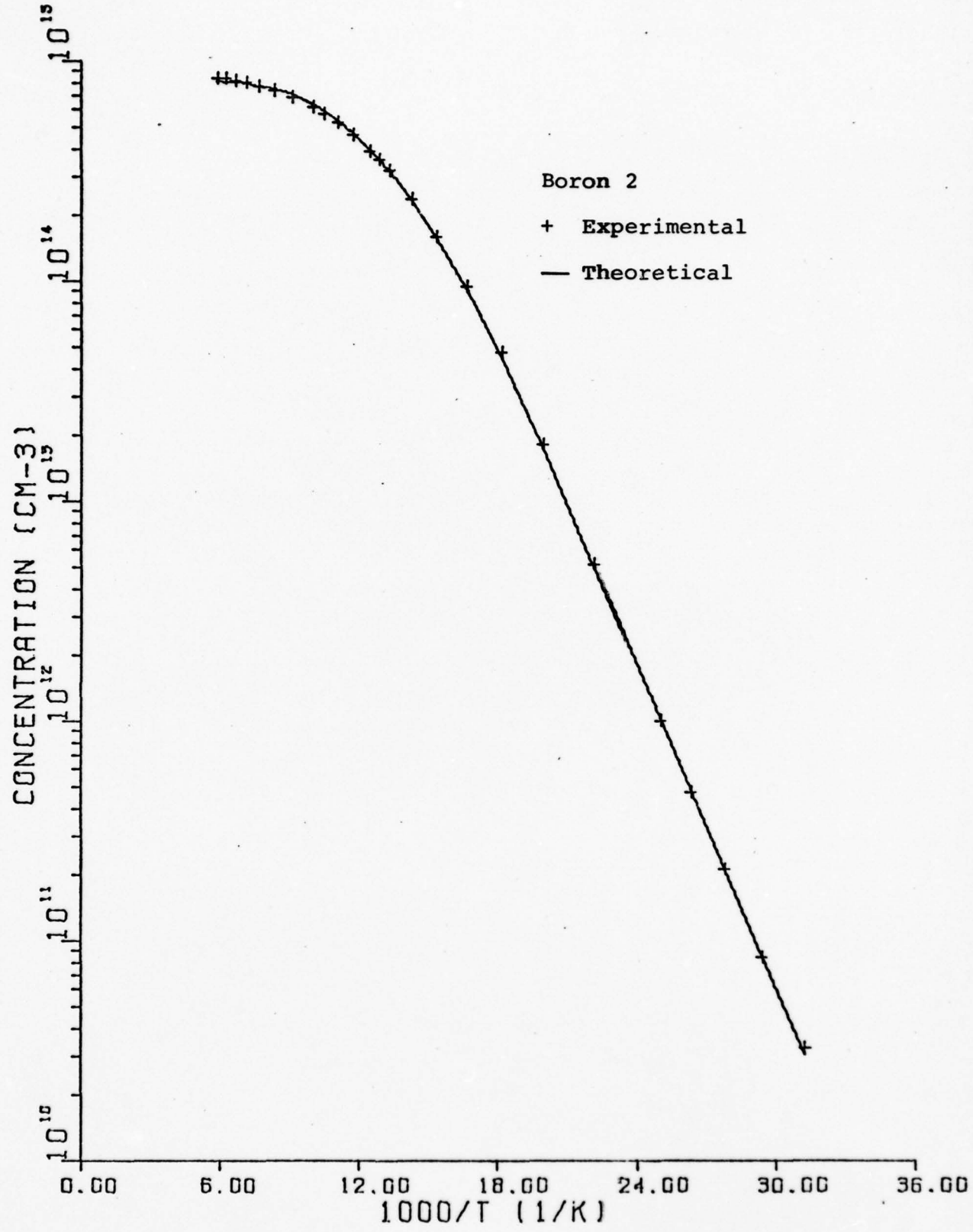

Figure A21 Carrier Concentration versus 1000/T

Boron 3

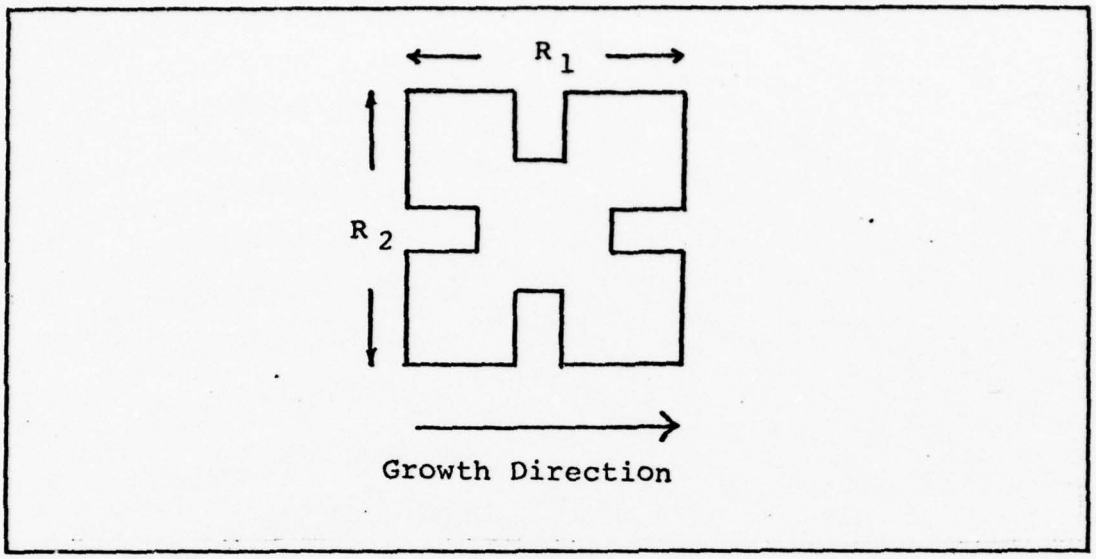

Figure A22 Resistances Relative to the Growth Axis

$N_a = 1.969 \times 10^{15}$ cm^{-3}

$N_d = 5.996 \times 10^{14}$ cm^{-3}

$\epsilon_a = .0427$ ev

thickness .0324 cm

Boron 3

Table VIII

TEMP	1000/T	RATIO	RESISTIVITY	MOBILITY	CONCENTRATION
20	50.000	1.797	4.437E+06	1.495E+04	9.412E+07
20	50.000	1.867	4.455E+06	1.360E+04	1.033E+08
21	47.619	1.201	2.611E+06	1.426E+04	1.677E+08
22	45.455	1.597	1.220E+06	1.725E+04	2.966E+08
23	43.478	1.481	6.842E+05	1.751E+04	5.210E+08
24	41.667	1.446	4.002E+05	1.771E+04	8.807E+08
25	40.000	1.389	2.336E+05	1.775E+04	1.505E+09
26	38.462	1.365	1.404E+05	1.783E+04	2.494E+09
27	37.037	1.335	8.177E+04	1.766E+04	4.324E+09
28	35.714	1.326	5.205E+04	1.760E+04	6.814E+09
29	34.483	1.321	3.077E+04	1.741E+04	1.165E+10
30	33.333	1.314	1.920E+04	1.721E+04	1.890E+10
32	31.250	1.307	7.915E+03	1.710E+04	4.718E+10
34	29.412	1.298	3.293E+03	1.652E+04	1.148E+11
36	27.778	1.273	1.453E+03	1.584E+04	2.712E+11
38	26.316	1.273	6.725E+02	1.546E+04	6.003E+11
40	25.000	1.270	3.361E+02	3.361E+02	1.241E+12
45	22.222	1.271	7.466E+01	1.375E+04	6.081E+12
50	20.000	1.263	2.303E+01	1.265E+04	2.143E+13
55	18.182	1.259	9.545E+00	1.146E+04	5.707E+13
60	16.667	1.264	5.071E+00	1.034E+04	1.190E+14
65	15.385	1.256	3.270E+00	9.240E+03	2.066E+14
70	14.286	1.258	2.411E+00	8.216E+03	3.151E+14
75	13.333	1.257	1.963E+00	7.329E+03	4.339E+14
80	12.500	1.253	1.711E+00	6.579E+03	5.545E+14
85	11.765	1.248	1.576E+00	5.956E+03	6.651E+14
90	11.111	1.251	1.495E+00	5.338E+03	7.822E+14
95	10.526	1.248	1.469E+00	4.891E+03	8.685E+14
100	10.000	1.245	1.471E+00	4.506E+03	9.420E+14

TEMP	1000/T	RATIO	RESISTIVITY	MOBILITY	CONCENTRATION
110	9.091	1.247	1.535E+00	3.807E+03	1.068E+15
120	8.333	1.244	1.663E+00	3.246E+03	1.156E+15
130	7.692	1.244	1.837E+00	2.789E+03	1.218E+15
140	7.143	1.239	2.056E+00	2.403E+03	1.263E+15
150	6.667	1.242	2.315E+00	2.088E+03	1.292E+15
160	6.250	1.240	2.613E+00	1.800E+03	1.327E+15
170	5.882	1.241	2.955E+00	1.578E+03	1.339E+15
180	5.556	1.239	3.341E+00	1.375E+03	1.359E+15
200	5.000	1.237	4.238E+00	1.052E+03	1.401E+15
220	4.545	1.235	5.306E+00	8.314E+02	1.415E+15
240	4.167	1.232	6.549E+00	6.837E+02	1.394E+15
260	3.846	1.233	7.980E+00	5.396E+02	1.450E+15
280	3.371	1.233	9.565E+00	4.390E+02	1.487E+15
300	3.333	1.231	1.125E+01	3.612E+02	1.536E+15
320	3.125	1.239	1.316E+01	3.141E+02	1.510E+15
340	2.941	1.238	1.733E+01	2.280E+02	1.579E+15
400	2.500	1.240	2.202E+01	1.811E+02	1.565E+15

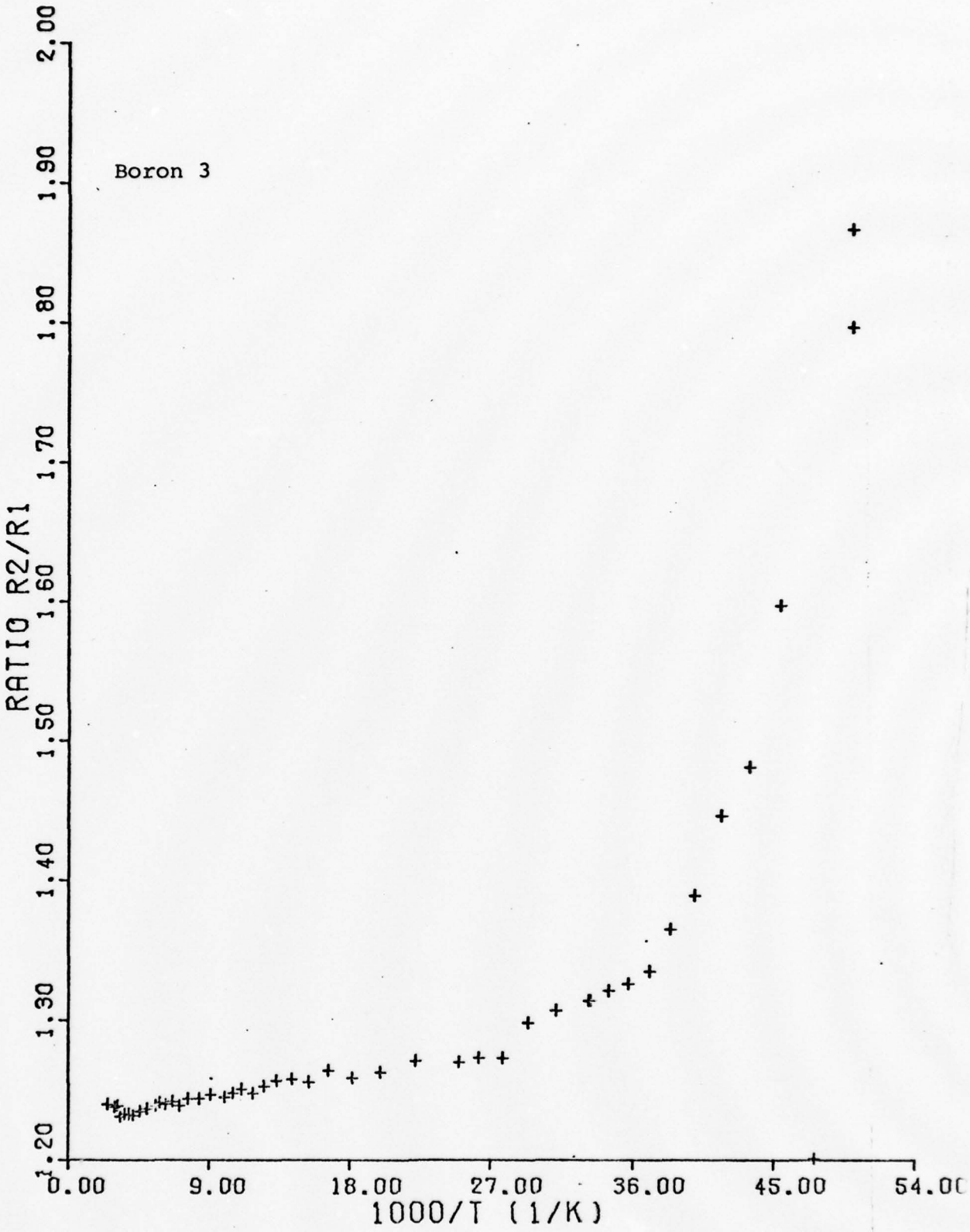

Figure A23 Resistivity Ratio versus 1000/T

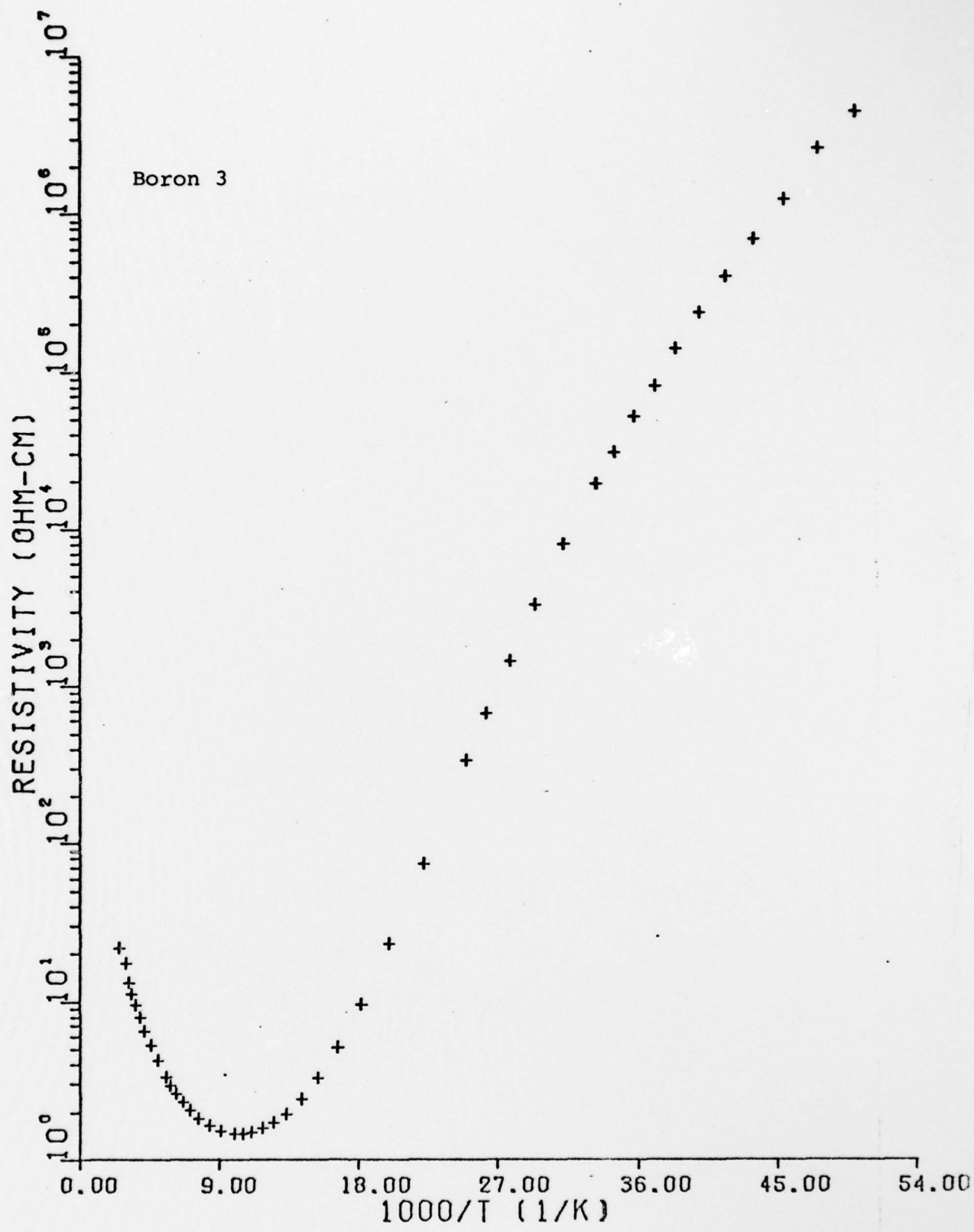

Figure A24 Resistivity versus 1000/T

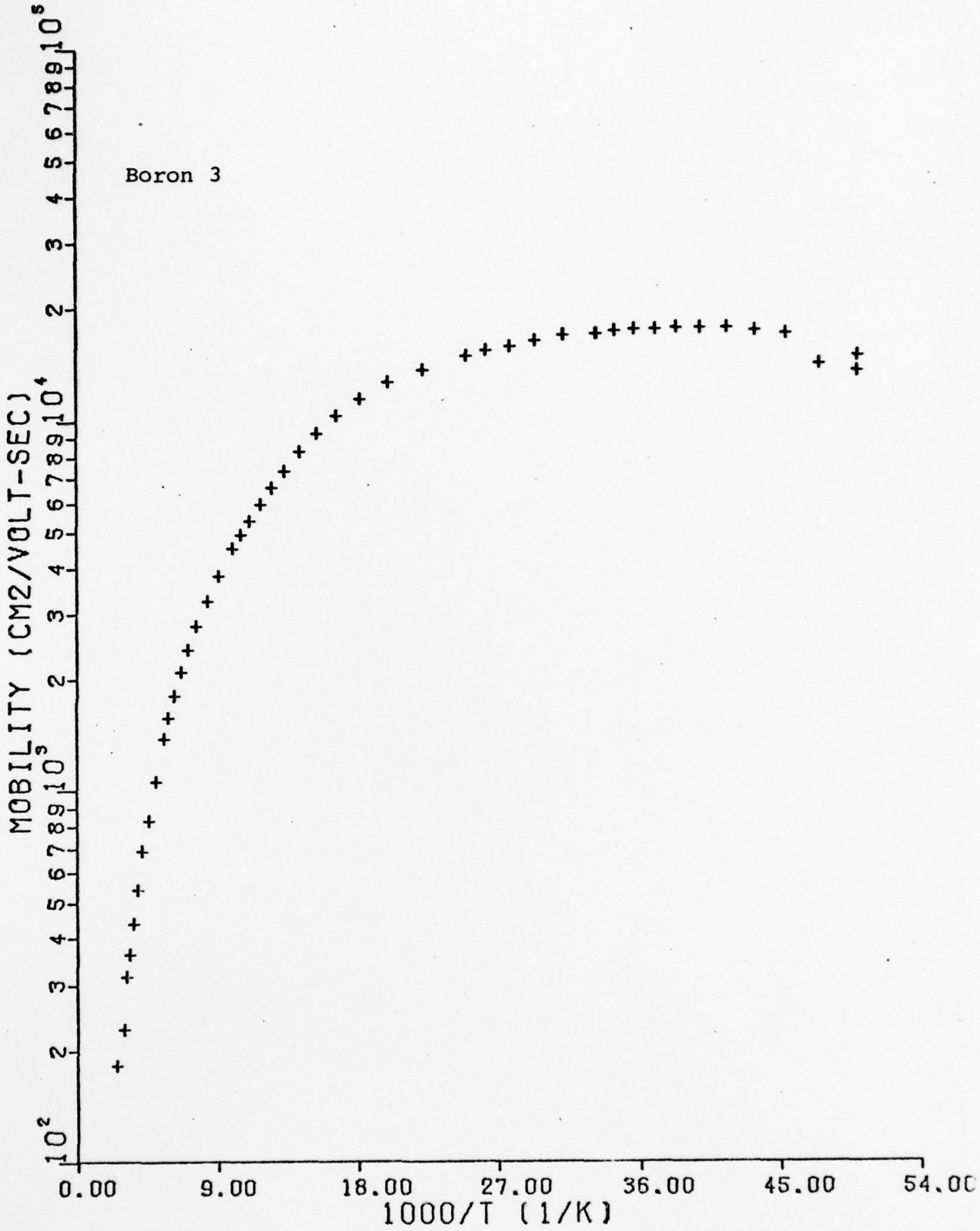

Figure A25 Mobility versus 1000/T

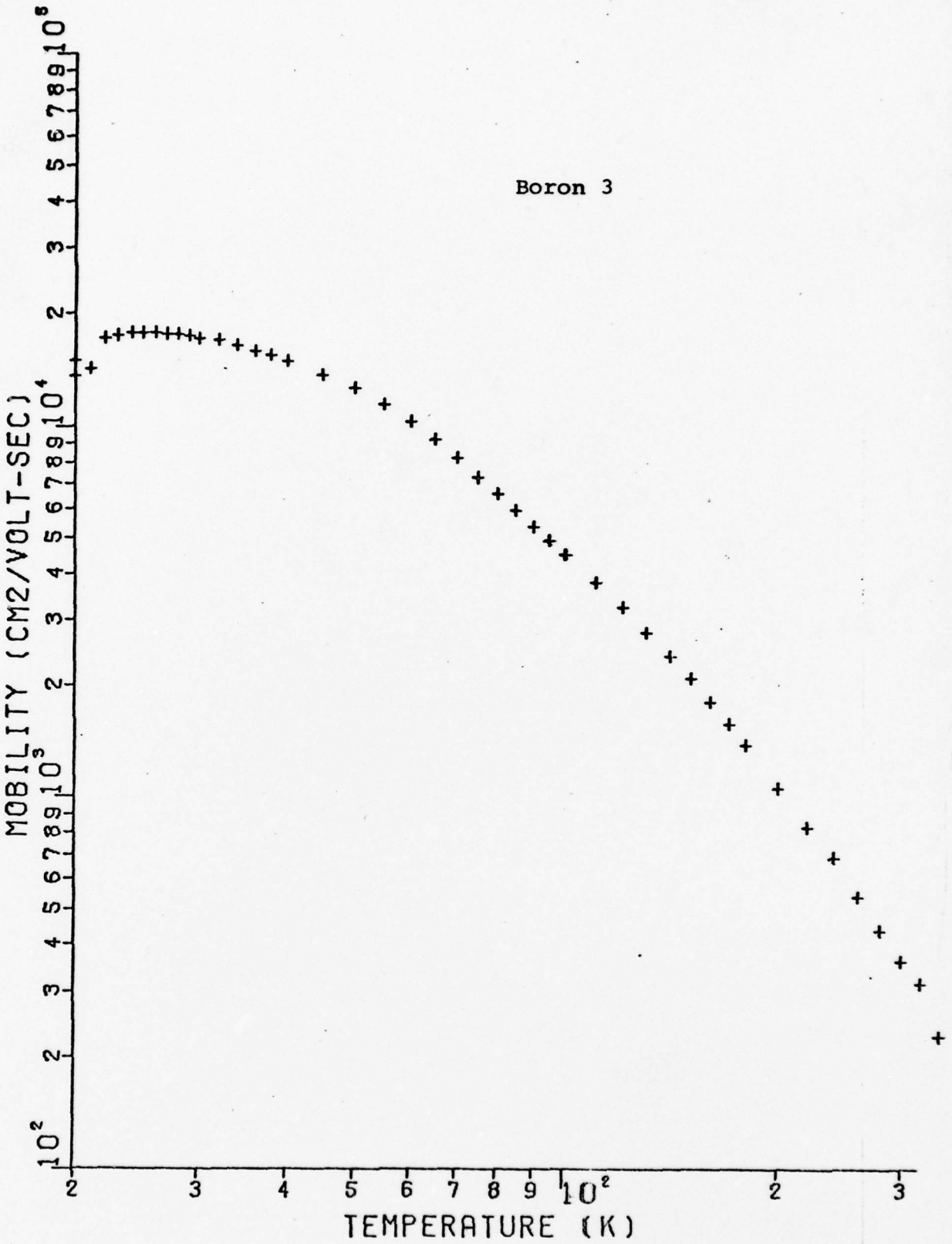

Figure A26 Mobility versus Temperature

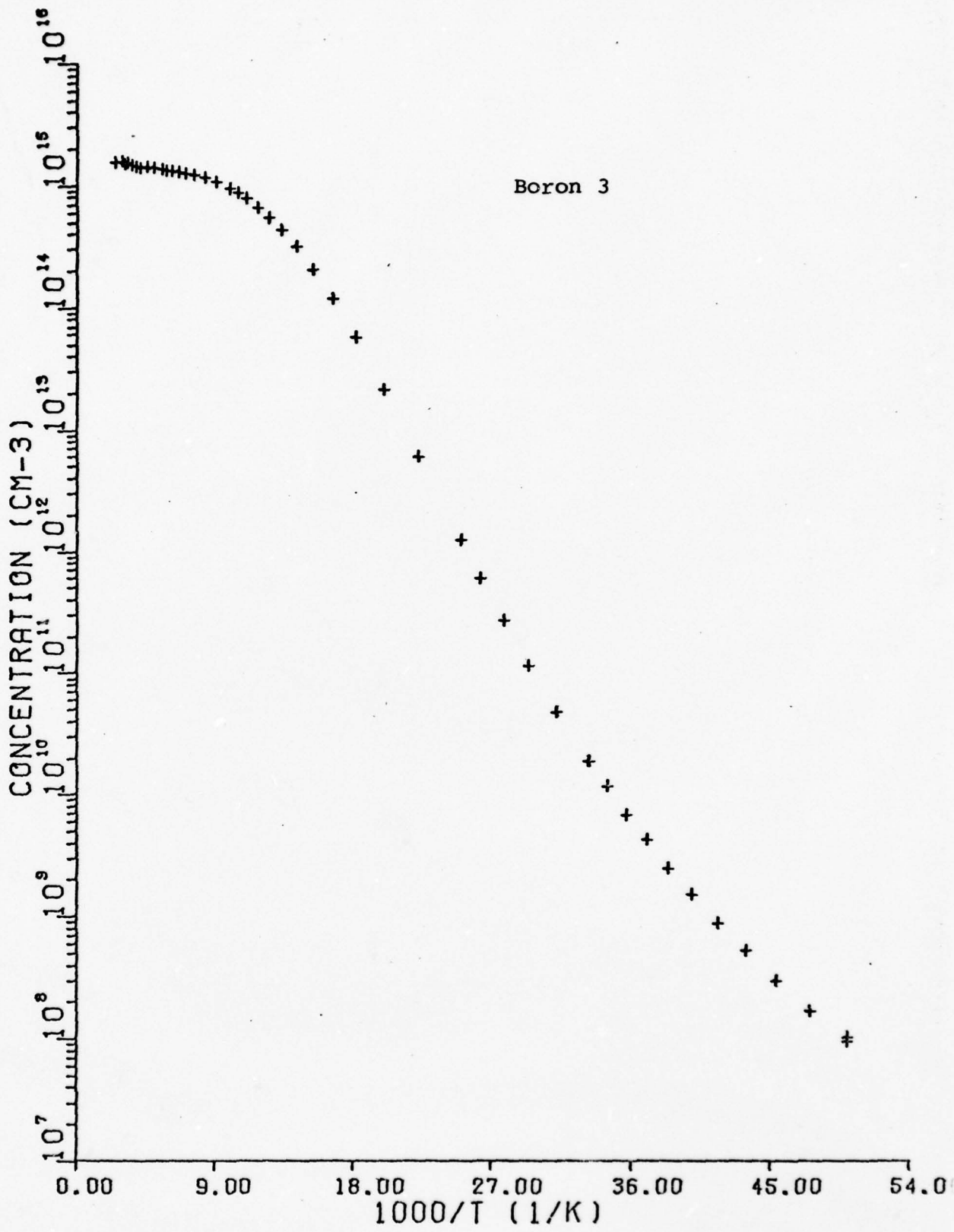

Figure A27 Carrier Concentration versus 1000/T

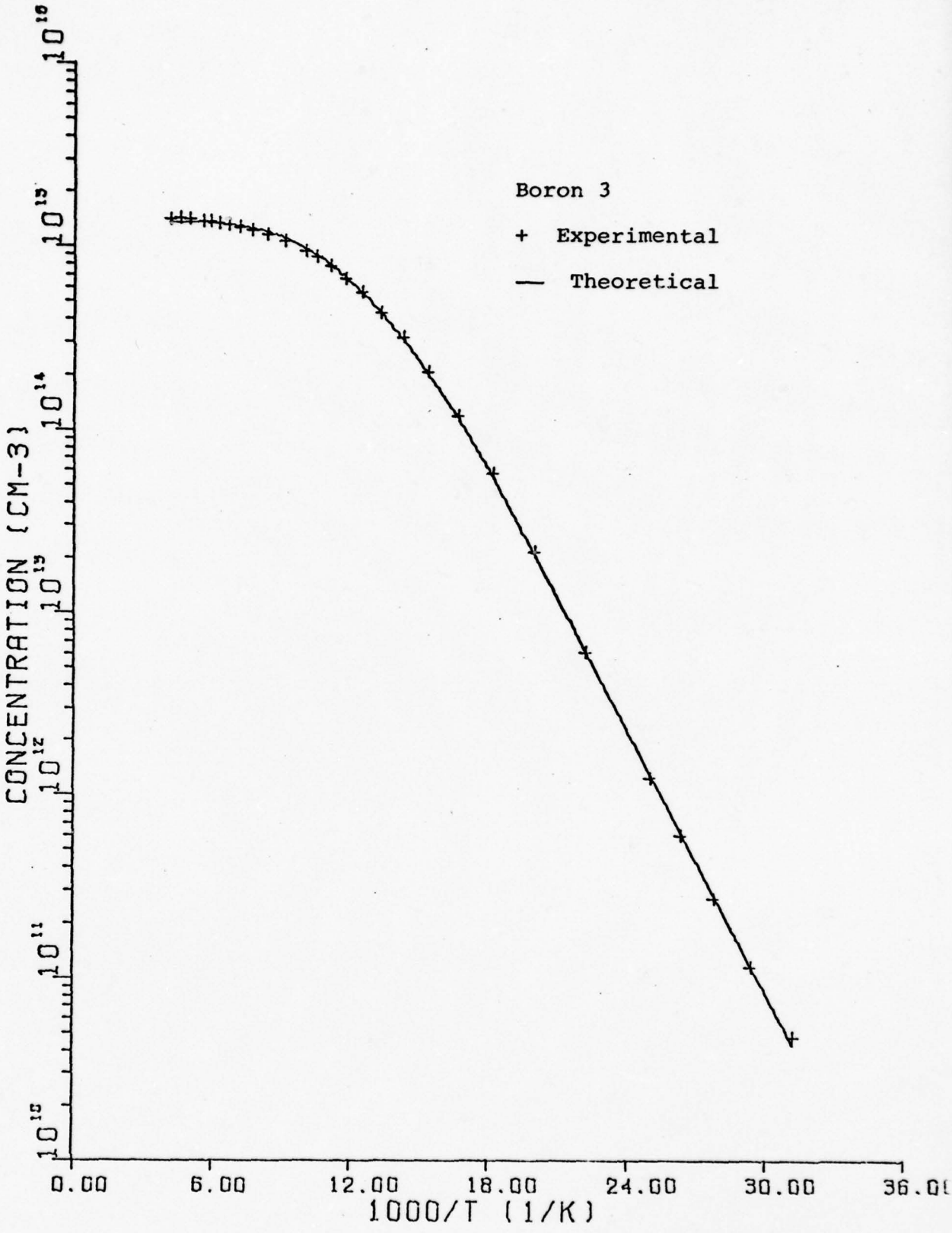

Figure A28 Carrier Concentration versus 1000/T

Boron 4

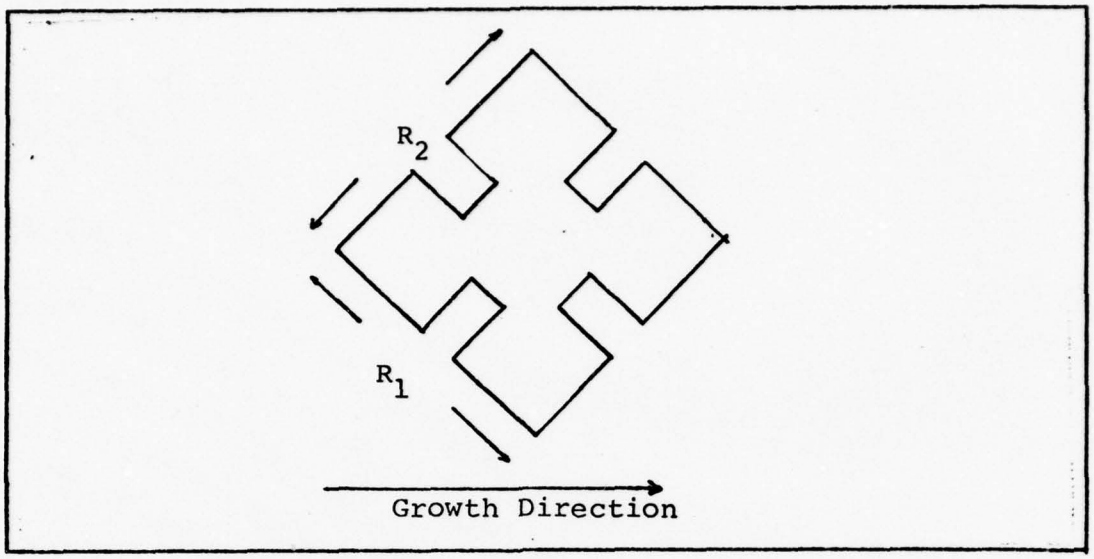

Figure A29 Resistances Relative to the Growth Axis

$N_a = 1.808 \times 10^{15}$ cm^{-3}

$N_d = 6.619 \times 10^{14}$ cm^{-3}

$\epsilon_a = .0423$ ev

thickness .0332 cm

Boron 4

Table IX

TEMP	1000/T	RATIO	RESISTIVITY	MOBILITY	CONCENTRATION
20	50.000	1.163	4.273E+06	1.873E+04	7.799E+07
20	50.000	1.143	4.275E+06	1.706E+04	8.559E+07
21	47.619	1.150	2.96E+06	1.811E+04	1.570E+08
22	45.455	1.181	1.196E+06	1.949E+04	2.679E+08
23	43.478	1.189	6.780E+05	1.940E+04	4.746E+08
24	41.667	1.217	3.968E+05	2.006E+04	7.845E+08
25	40.000	1.280	2.239E+05	2.044E+04	1.364E+09
26	38.462	1.227	1.409E+05	1.992E+04	2.223E+09
27	37.037	1.220	8.334E+04	1.989E+04	3.765E+09
28	35.714	1.229	5.263E+04	1.954E+04	6.069E+09
29	34.483	1.227	3.227E+04	1.939E+04	9.976E+09
30	33.333	1.231	1.992E+04	1.916E+04	1.635E+10
32	31.250	1.234	8.042E+03	1.886E+04	4.116E+10
34	29.412	1.239	3.326E+03	1.834E+04	1.023E+11
36	27.778	1.235	1.469E+03	1.794E+04	2.368E+11
38	26.316	1.238	6.857E+02	1.732E+04	5.256E+11
40	25.000	1.227	3.413E+02	1.681E+04	1.088E+12
45	22.222	1.235	7.654E+01	1.534E+04	5.317E+12
50	20.000	1.239	2.388E+01	1.421E+04	1.840E+13
55	18.182	1.243	9.911E+00	1.291E+04	4.880E+13
60	16.667	1.247	5.274E+00	1.166E+04	1.015E+14
65	15.385	1.255	3.401E+00	1.051E+04	1.746E+14
70	14.286	1.261	2.507E+00	9.364E+03	2.659E+14
75	13.333	1.255	2.043E+00	8.344E+03	3.662E+14
80	12.500	1.261	1.776E+00	7.455E+03	4.714E+14
85	11.765	1.261	1.634E+00	6.744E+03	5.666E+14
90	11.111	1.259	1.558E+00	6.138E+03	6.529E+14
95	10.526	1.265	1.526E+00	5.603E+03	7.302E+14
100	10.000	1.262	1.527E+00	5.125E+03	7.979E+14
110	9.091	1.266	1.594E+00	4.327E+03	9.049E+14

TEMP	1000/T	RATIO	RESISTIVITY	MOBILITY	CONCENTRATION
120	8.333	1.264	1.723E+00	3.703E+03	9.780E+14
130	7.692	1.267	1.906E+00	3.170E+03	1.033E+15
140	7.143	1.271	2.127E+00	2.743E+03	1.070E+15
150	6.667	1.271	2.396E+00	2.351E+03	1.108E+15
160	6.250	1.266	2.709E+00	2.046E+03	1.126E+15
170	5.882	1.274	3.062E+00	1.788E+03	1.140E+15
180	5.556	1.270	3.456E+00	1.562E+03	1.156E+15
200	5.000	1.273	4.387E+00	1.201E+03	1.185E+15
220	4.545	1.271	5.491E+00	9.399E+02	1.210E+15
240	4.167	1.273	6.790E+00	7.494E+02	1.227E+15
260	3.846	1.266	8.254E+00	6.114E+02	1.237E+15
280	3.571	1.269	9.883E+00	4.978E+02	1.269E+15
300	3.333	1.264	1.164E+00	4.180E+02	1.283E+15
320	3.125	1.258	1.354E+01	3.556E+02	1.296E+15
360	2.778	1.250	1.776E+01	2.634E+02	1.335E+15
400	2.500	1.247	2.254E+01	1.979E+02	1.399E+15

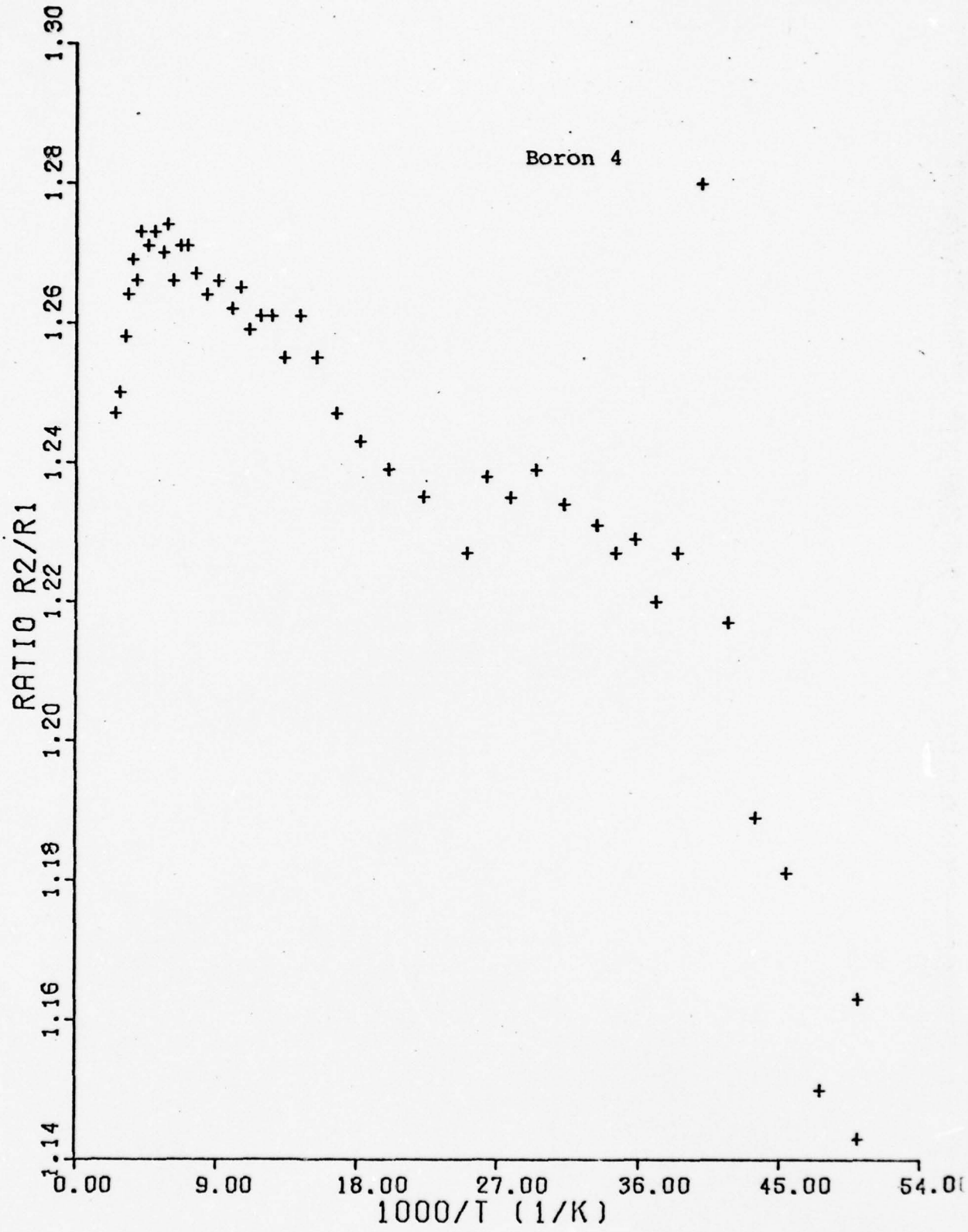

Figure A30 Resistivity Ratio versus 1000/T

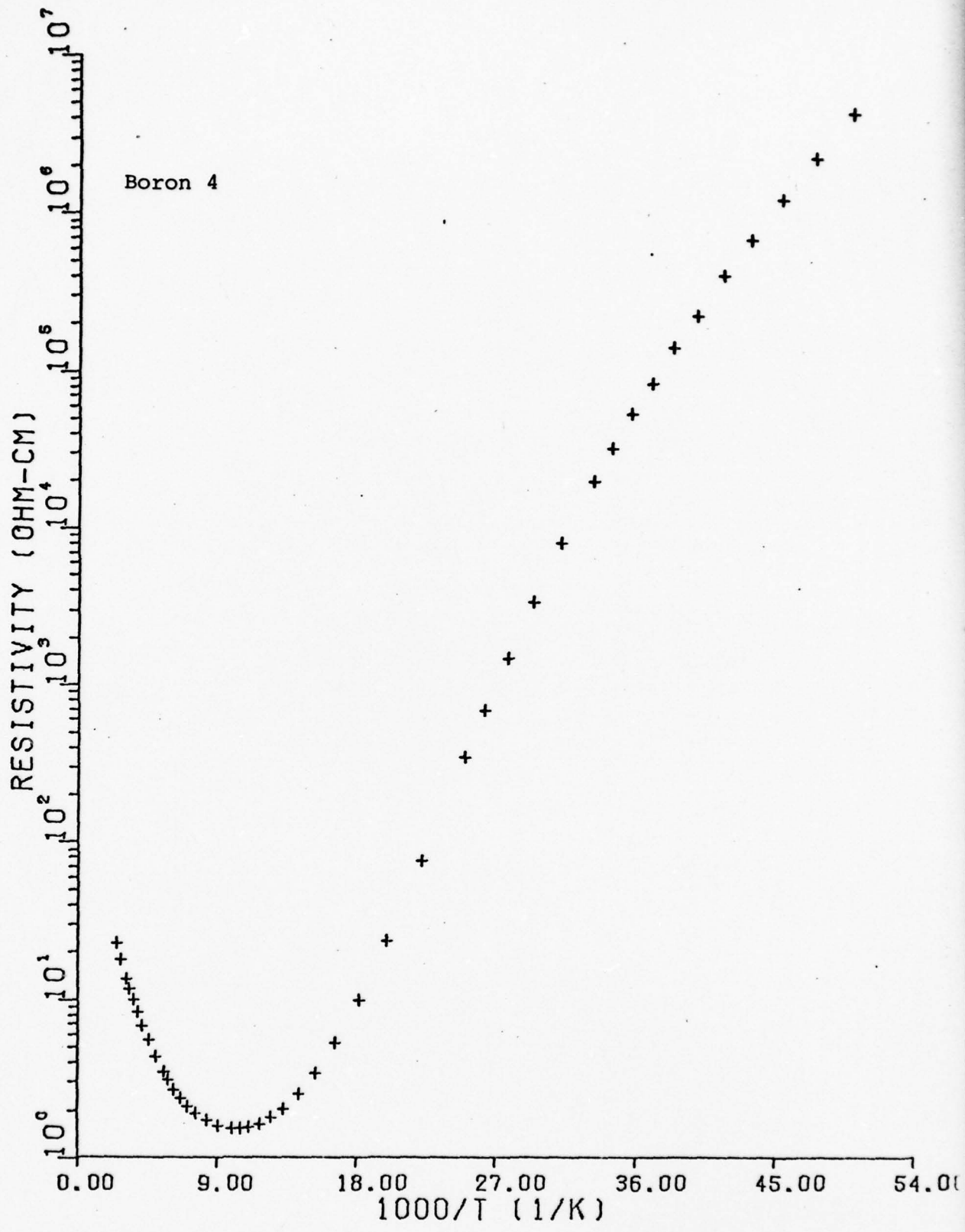

Figure A31 Resistivity versus 1000/T

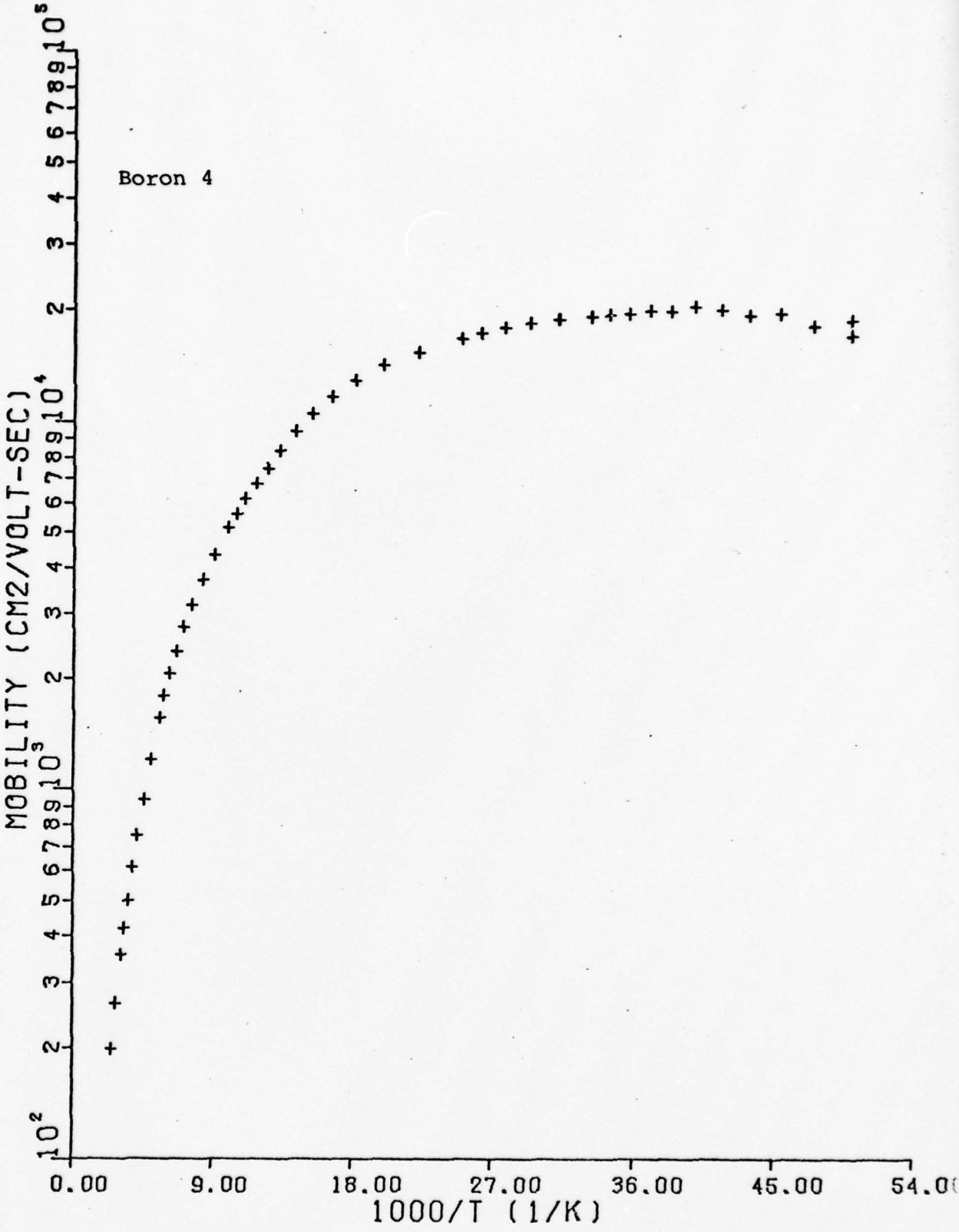

Figure A32 Mobility versus 1000/T

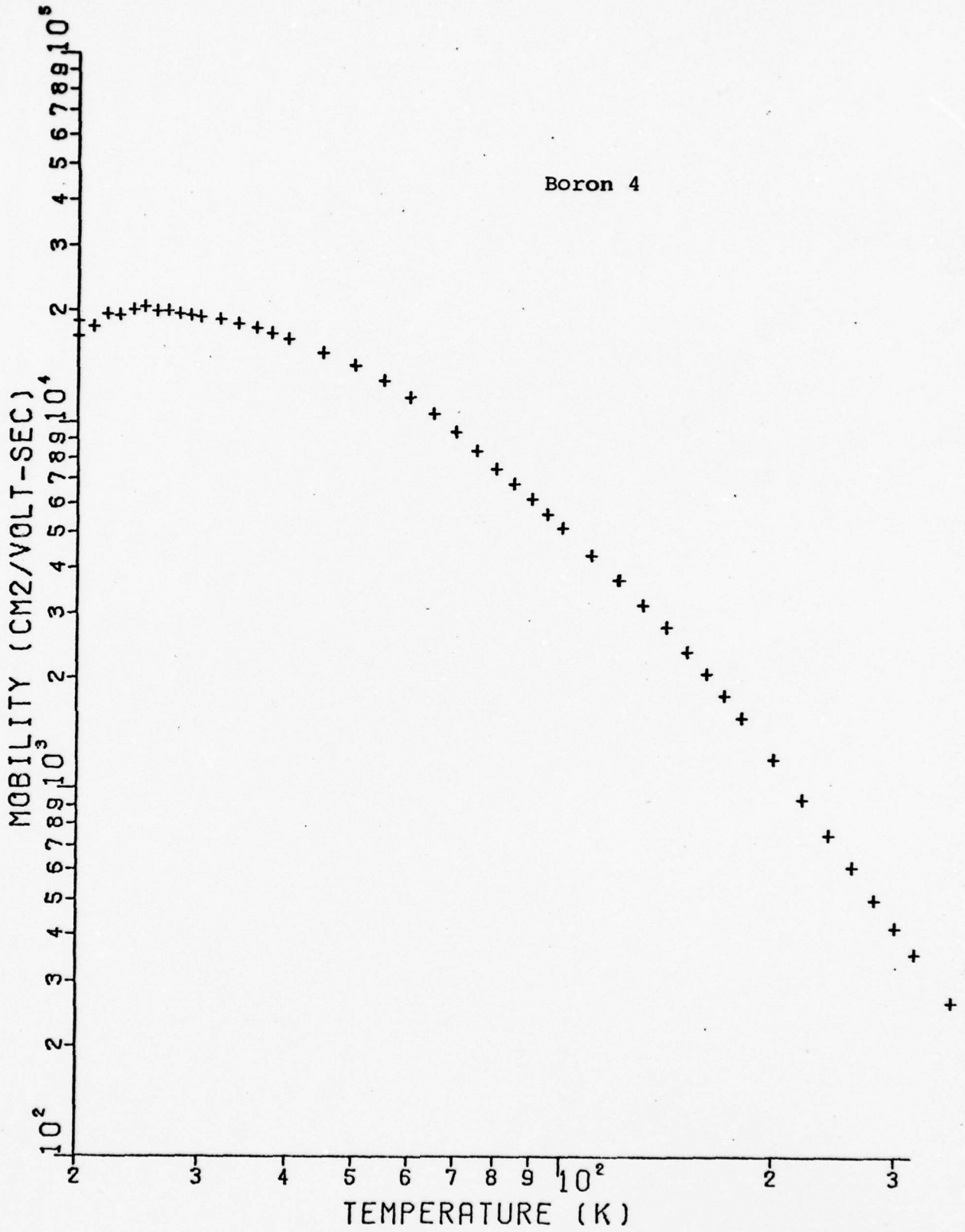

Figure A33 Mobility versus Temperature

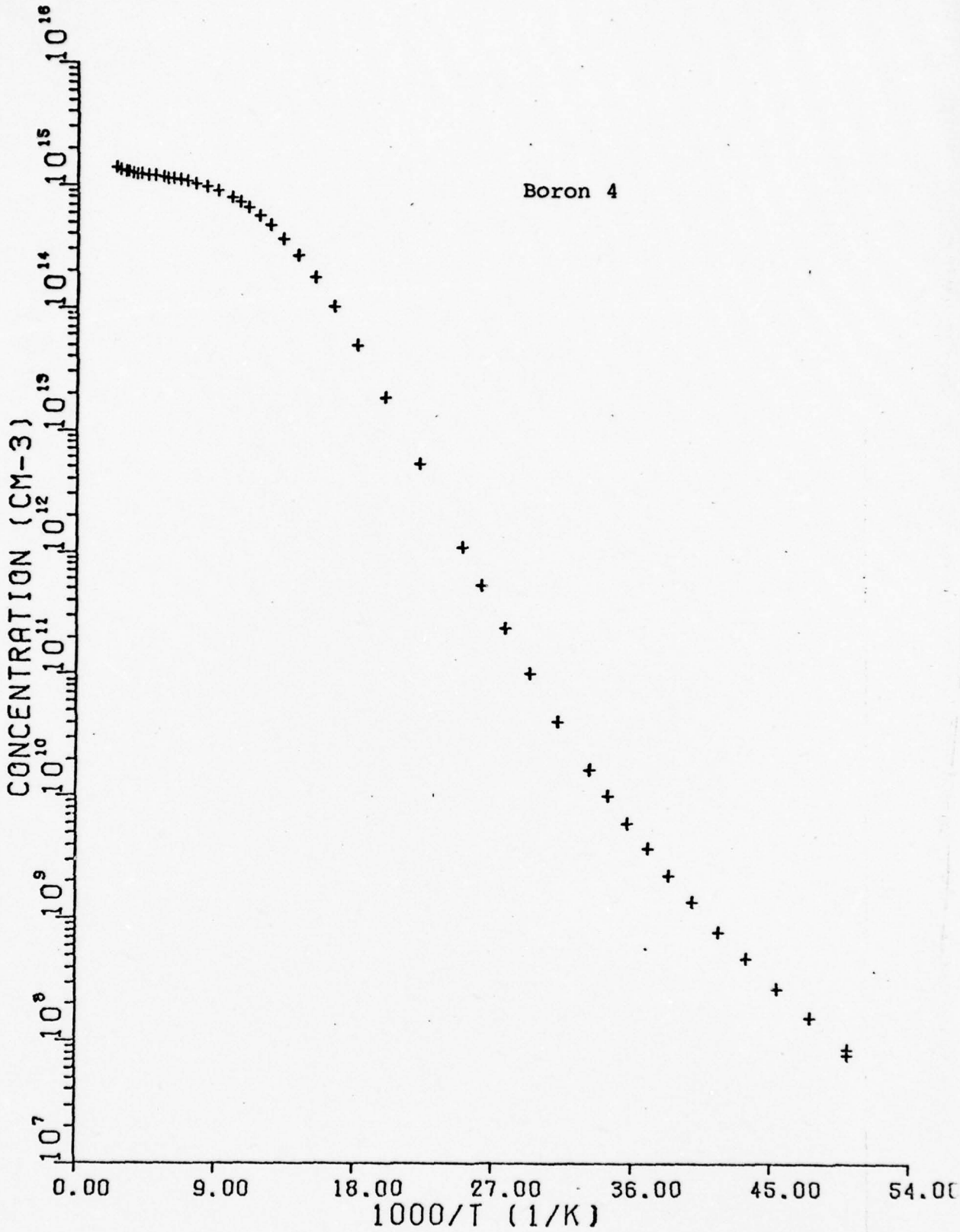

Figure A34 Carrier Concentration versus 1000/T

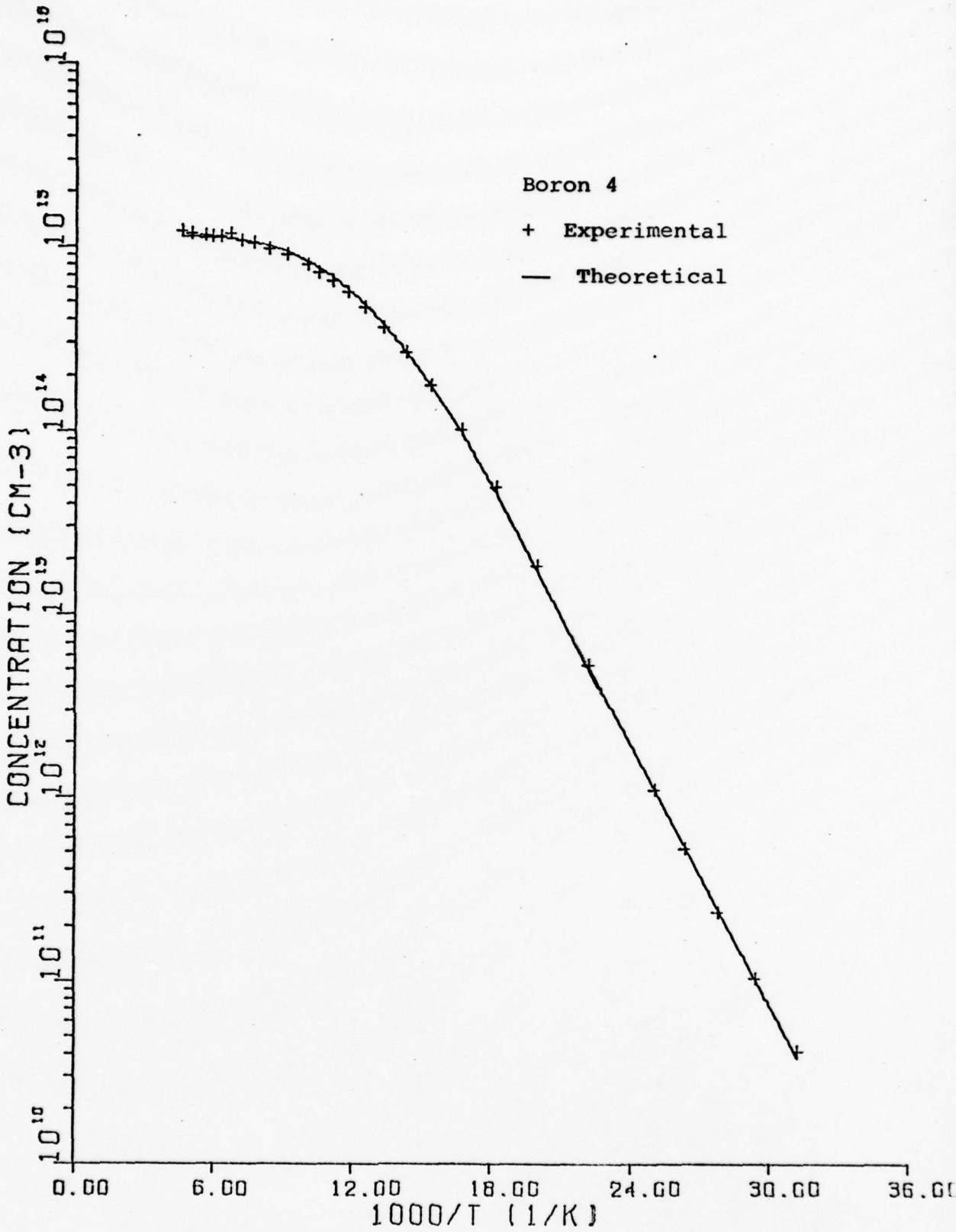

Figure A35 Carrier Concentration versus 1000/T

Gallium 1

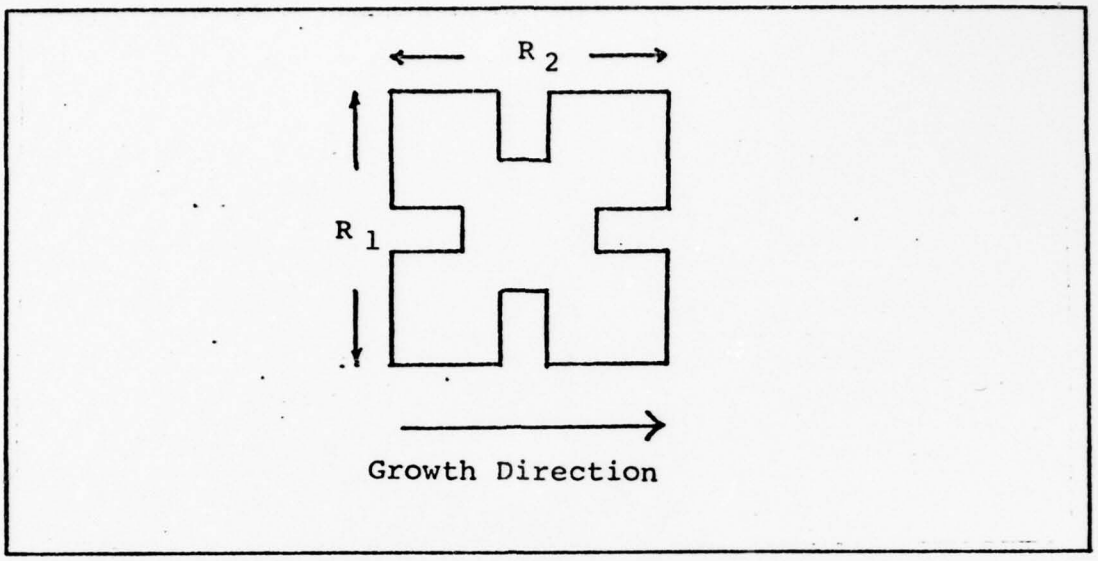

Figure A36 Resistance Relative to the Growth Axis

$N_a = 1.261 \times 10^{16}$ cm^{-3}

$N_d = 4.743 \times 10^{14}$ cm^{-3}

$\epsilon_a = .0654$ ev

thickness .020 cm

Gallium 1

Table X

TEMP	1000/T	RATIO	RESISTIVITY	MOBILITY	CONCENTRATION
30	33.333	.594	2.807E+07	5.585E+03	3.982E+07
32	31.250	.564	5.872E+06	7.407E+03	1.458E+08
34	29.412	.543	1.375E+06	7.553E+03	6.008E+08
36	27.778	.545	3.740E+05	7.645E+03	2.183E+09
38	26.316	.554	1.142E+05	7.749E+03	7.055E+09
40	25.000	.566	3.892E+04	7.648E+03	2.097E+10
45	22.222	.603	4.020E+03	7.469E+03	2.079E+11
50	20.000	.641	6.647E+02	7.061E+03	1.330E+12
55	18.182	.678	1.553E+02	6.700E+03	6.000E+12
60	16.667	.718	4.911E+01	6.256E+03	2.032E+13
65	15.385	.764	1.987E+01	5.856E+03	5.365E+13
70	14.286	.806	1.005E+01	5.176E+03	1.201E+14
75	13.333	.841	5.953E+00	4.905E+03	2.138E+14
80	12.500	.860	4.044E+00	4.413E+03	3.498E+14
85	11.765	.877	2.959E+00	4.003E+03	5.247E+14
90	11.111	.890	2.295E+00	3.550E+03	7.630E+14
95	10.526	.896	1.867E+00	3.216E+03	1.035E+15
100	10.000	.908	1.585E+00	2.867E+03	1.368E+15
105	9.524	.914	1.387E+00	2.542E+03	1.763E+15
110	9.091	.914	1.236E+00	2.297E+03	2.189E+15
115	8.696	.922	1.130E+00	2.059E+03	2.672E+15
120	8.333	.918	1.049E+00	1.871E+03	3.166E+15
125	8.000	.923	9.890E-01	1.707E+03	3.679E+15
125	8.000	.919	9.910E-01	1.777E+03	3.531E+15
130	7.692	.920	9.440E-01	1.550E+03	4.247E+15
130	7.692	.932	9.410E-01	1.585E+03	4.169E+15
140	7.143	.933	8.980E-01	1.355E+03	5.183E+15
150	6.667	.923	8.800E-01	1.116E+03	6.328E+15
160	6.250	.934	8.960E-01	9.772E+02	7.096E+15

TEMP	1000/T	RATIO	RESISTIVITY	MOBILITY	CONCENTRATION
170	5.882	.926	9.260E-01	8.235E+02	8.152E+15
180	5.556	.933	9.780E-01	7.704E+02	8.250E+15
190	5.263	.926	1.039E+00	6.438E+02	9.294E+15
200	5.000	.931	1.119E+00	5.645E+02	9.841E+15
210	4.762	.925	1.205E+00	5.032E+02	1.025E+16
220	4.545	.931	1.310E+00	3.776E+02	1.257E+16
230	4.348	.921	1.429E+00	4.091E+02	1.063E+16
250	4.000	.921	1.670E+00	3.342E+02	1.113E+16
270	3.704	.919	1.960E+00	2.751E+02	1.150E+16
280	3.571	.916	2.115E+00	2.512E+02	1.170E+16
290	3.448	.918	2.284E+00	2.286E+02	1.191E+16
300	3.333	.915	2.452E+00	2.141E+02	1.184E+16
318	3.141	.913	2.785E+00	1.891E+02	1.180E+16

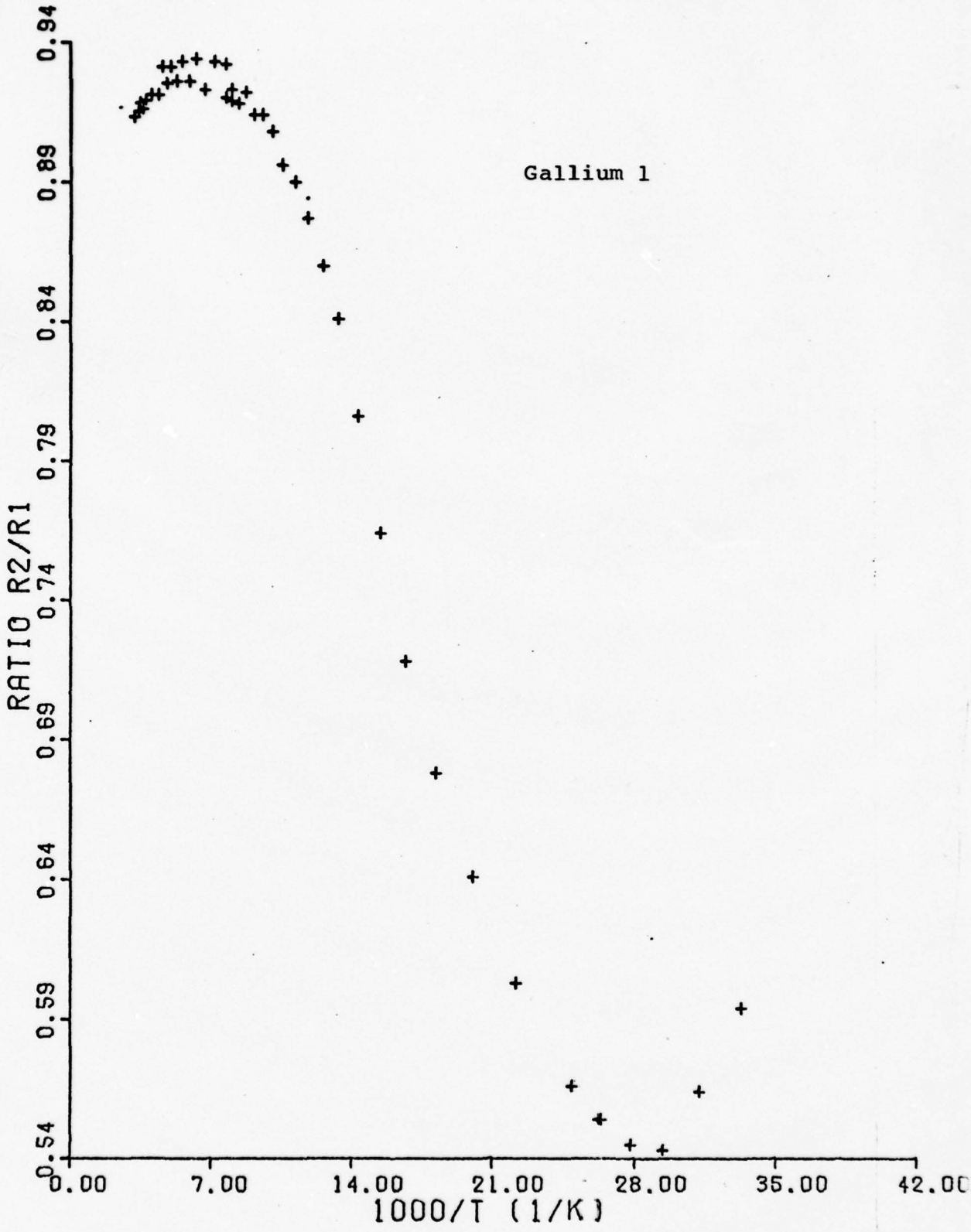

Figure A37 Resistivity Ratio versus 1000/T

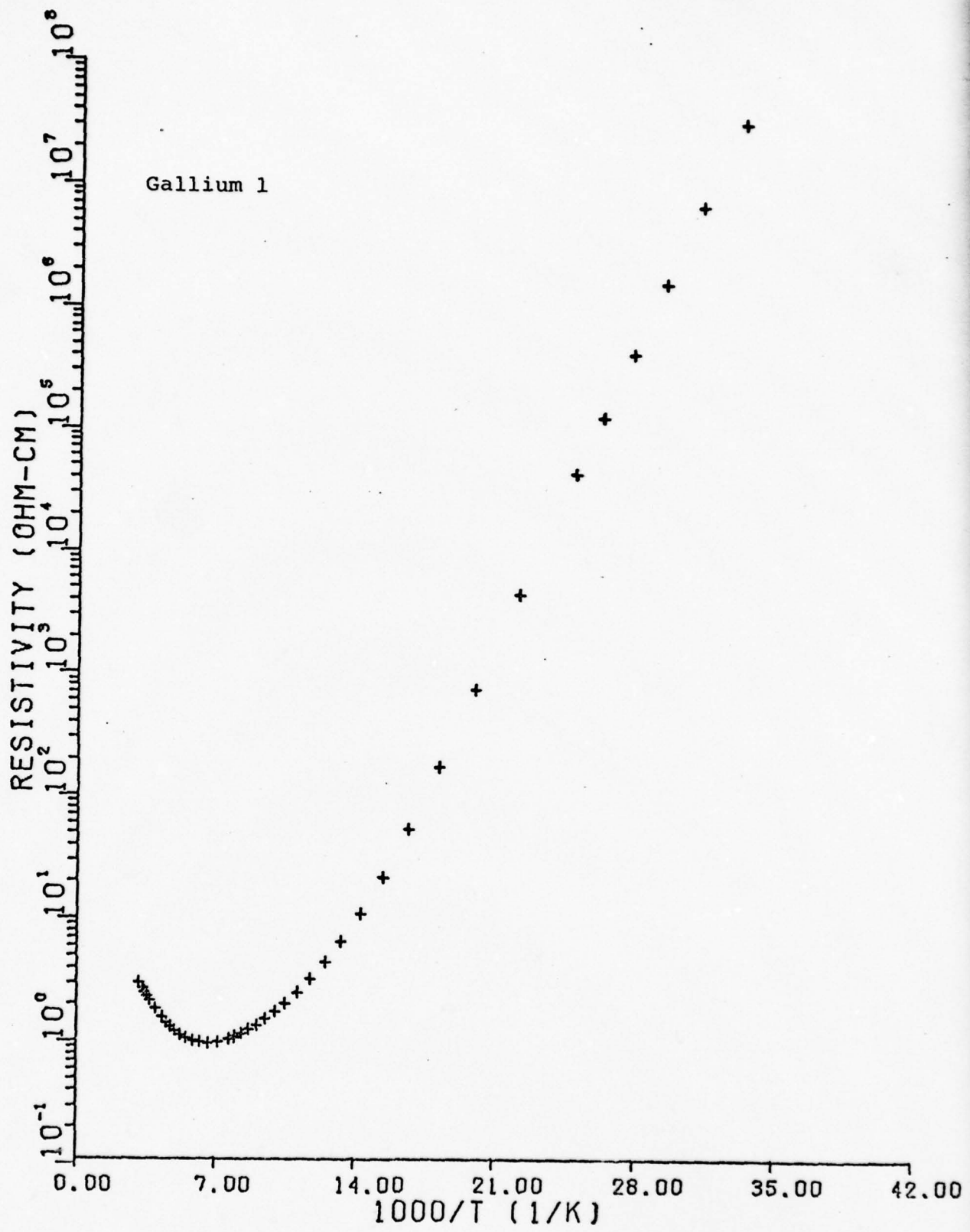

Figure A38 Resistivity versus 1000/T

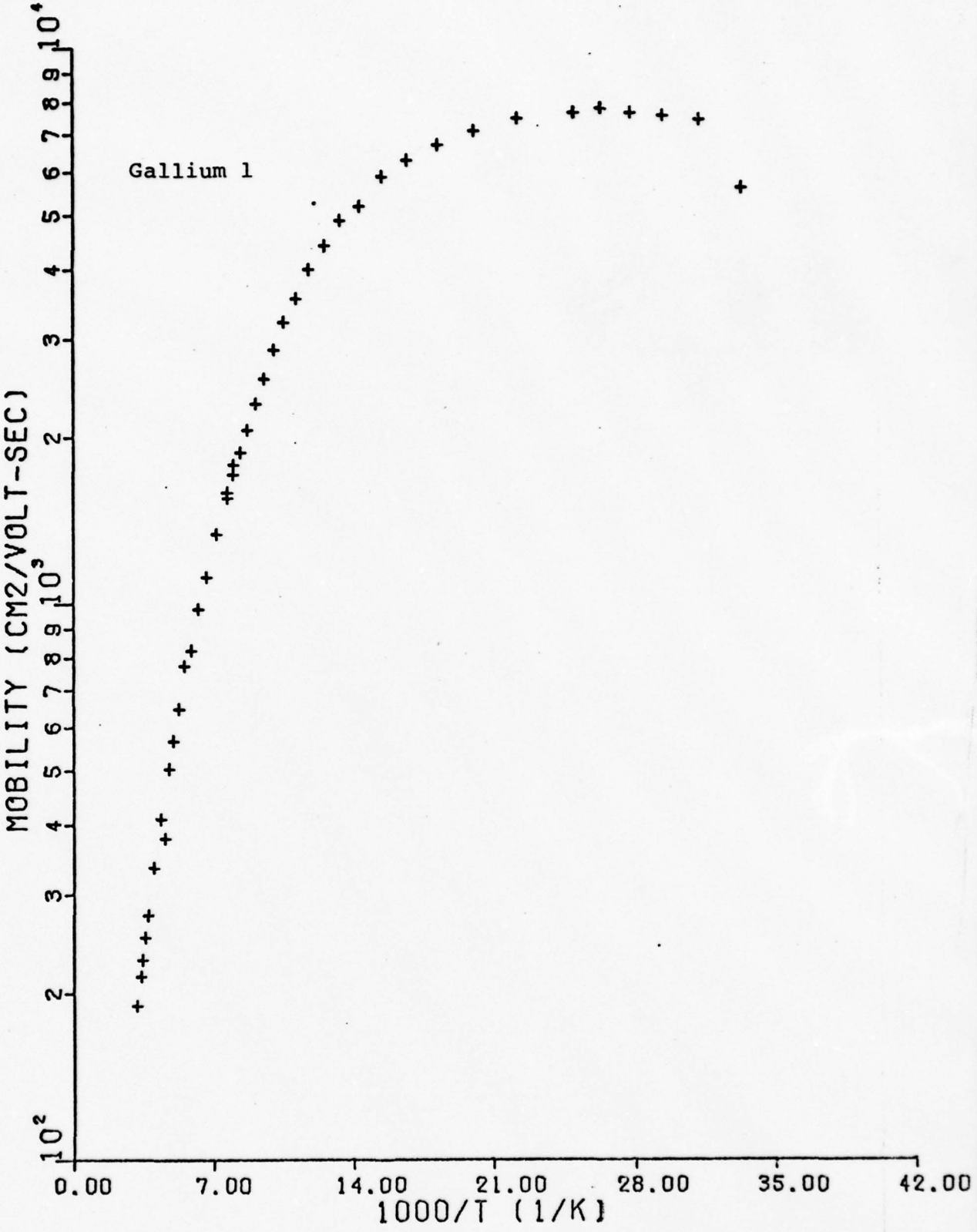

Figure A39 Mobility versus 1000/T

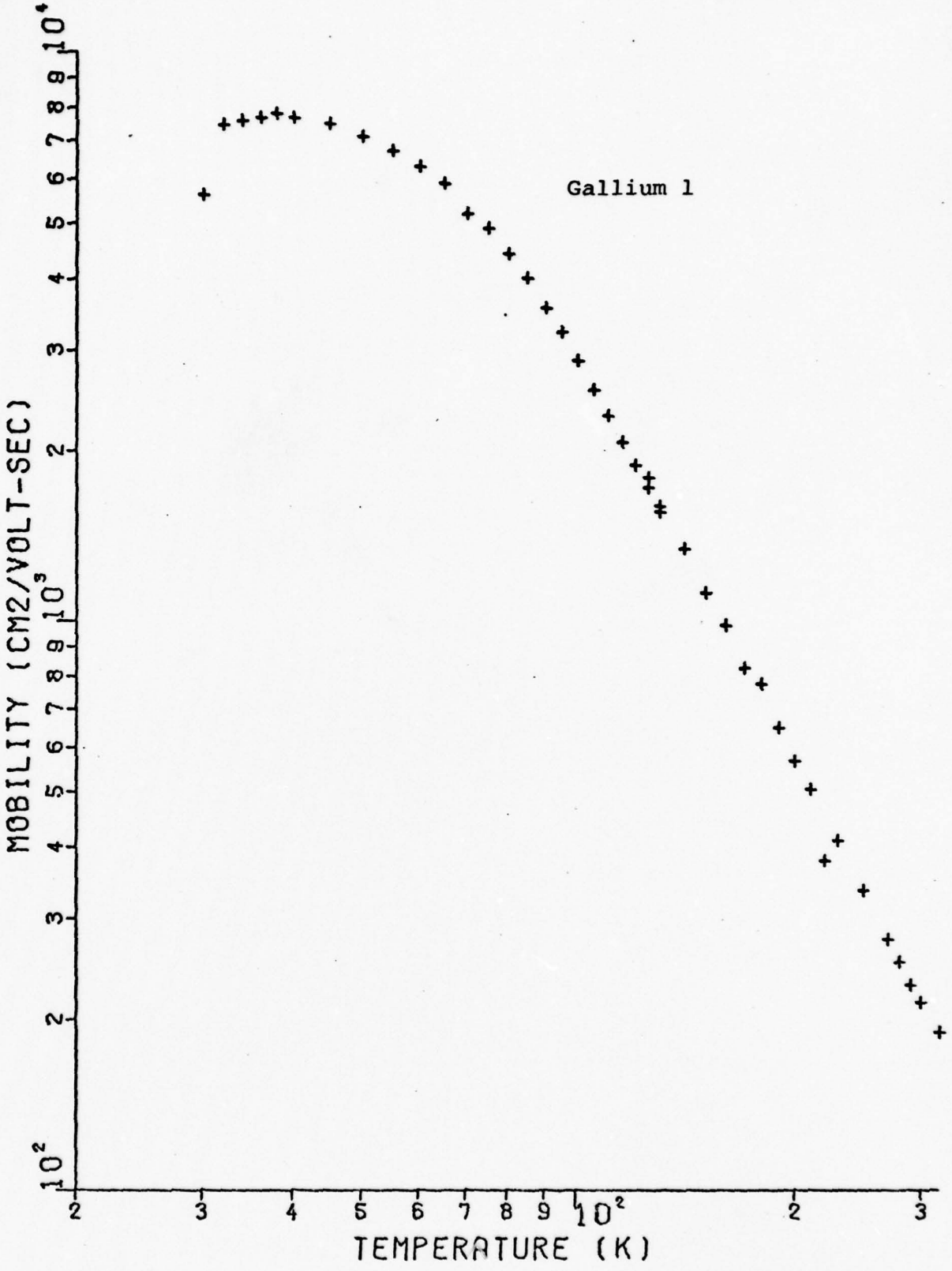

Figure A40 Mobility versus Temperature

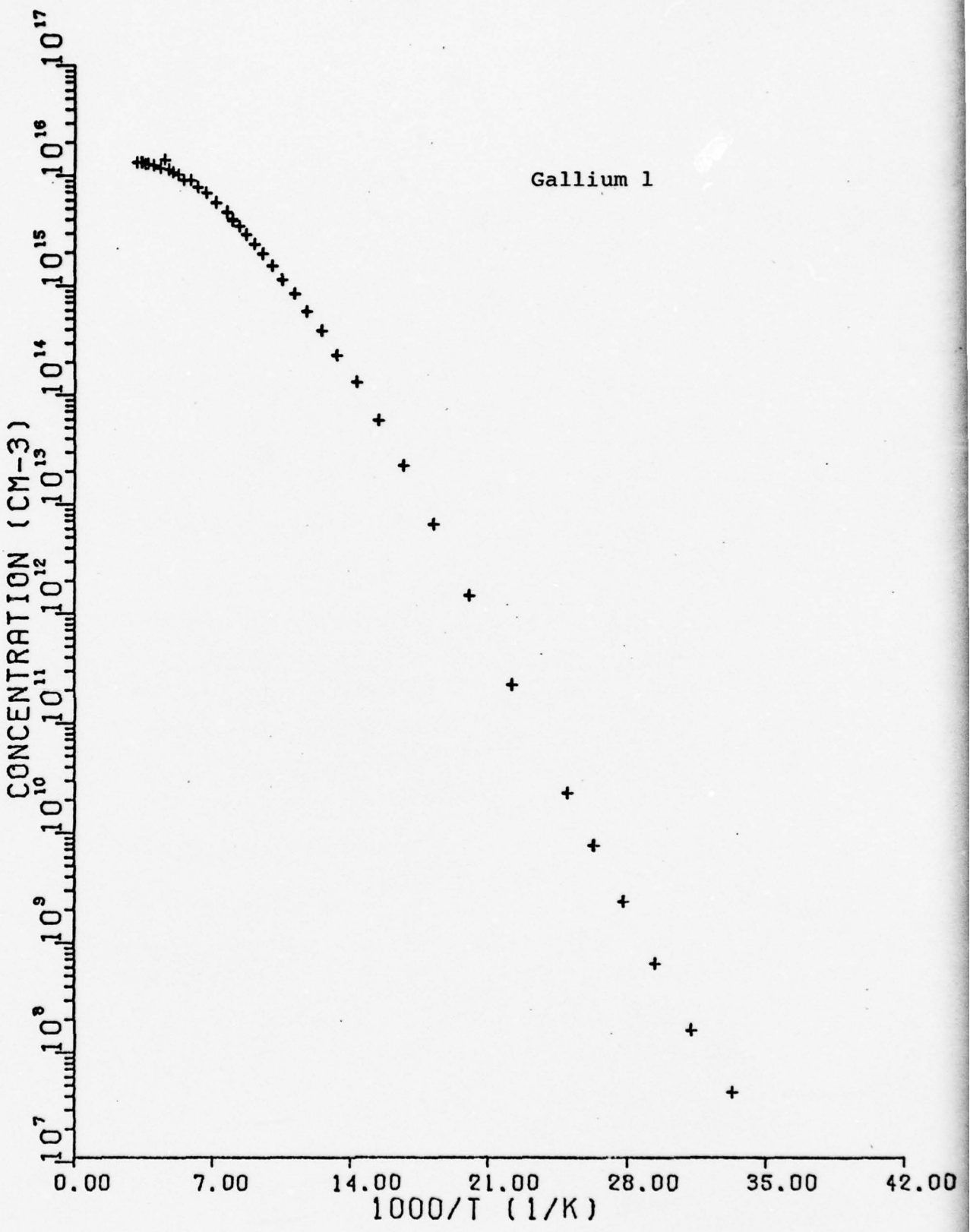

Figure A41 Carrier Concentration versus 1000/T

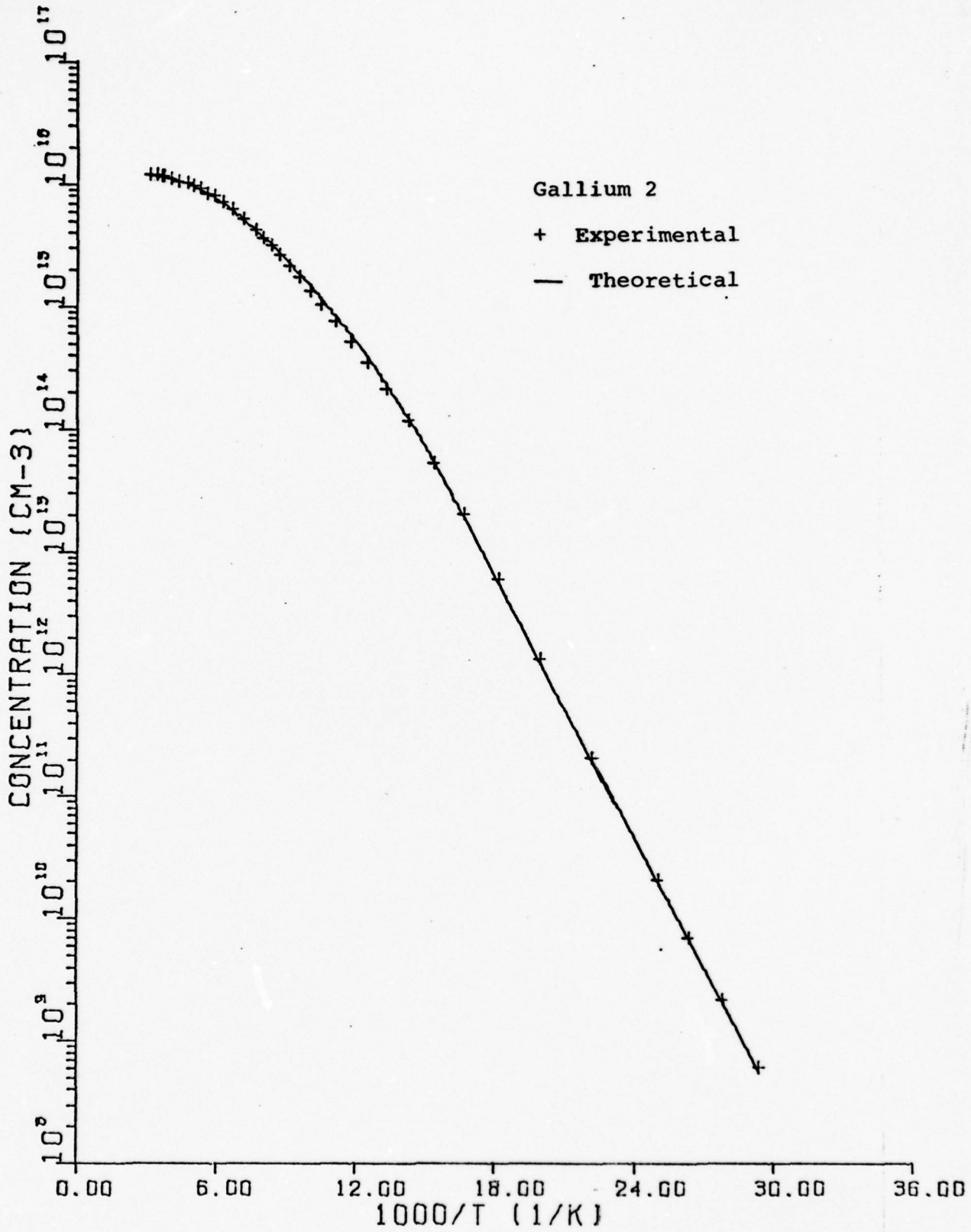

Figure A42 Carrier Concentration versus 1000/T

Gallium 2

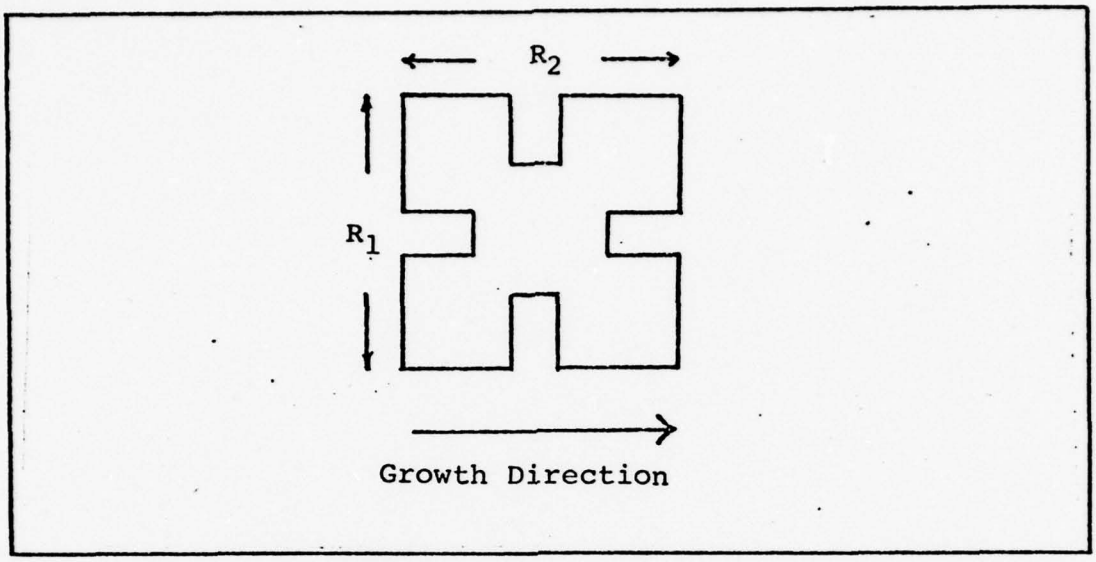

Figure A43 Resistances Relative to the Growth Axis

$N_a = 7.950 \times 10^{15}$ cm^{-3}

$N_d = 6.962 \times 10^{14}$ cm^{-3}

$\epsilon_a = .0634$ ev

thickness .0187 ev

Gallium 2

Table XI

TEMP	1000/T	RATIO	RESISTIVITY	MOBILITY	CONCENTRATION
26	38.462	.567	3.291E+08	4.523E+03	4.193E+06
27	37.037	.624	1.188E+08	4.790E+03	1.097E+07
27	37.037	.236	5.451E+07	1.680E+04	6.817E+06
28	35.714	.647	5.396E+07	4.812E+03	2.404E+07
29	34.483	.681	2.290E+07	4.888E+03	5.576E+07
29	34.483	.127	1.581E+07	1.123E+04	3.517E+07
30	33.333	.702	1.017E+07	4.780E+03	1.284E+08
32	31.250	.755	2.330E+06	4.840E+03	5.535E+08
32	31.250	.138	1.595E+06	1.251E+04	3.129E+08
34	29.412	.841	7.538E+06	9.959E+03	8.315E+08
36	27.778	.782	2.390E+05	1.464E+04	1.784E+09
36	27.778	.738	2.328E+05	1.531E+04	1.752E+09
38	26.316	.784	7.659E+04	1.479E+04	5.511E+09
40	25.000	.777	2.703E+04	1.455E+04	1.598E+10
45	22.222	.782	2.982E+03	1.395E+04	1.501E+11
50	20.000	.766	5.094E+02	1.304E+04	9.334E+11
55	18.182	.762	1.237E+02	1.207E+04	4.180E+12
60	16.667	.760	4.027E+01	1.125E+04	1.377E+13
65	15.385	.764	1.697E+01	1.044E+04	3.522E+13
70	14.286	.772	8.690E+00	9.502E+03	7.559E+13
75	13.333	.774	5.248E+00	8.541E+03	1.393E+14
80	12.500	.780	3.586E+00	7.651E+03	2.275E+14
85	11.765	.784	2.657E+00	6.854E+03	3.427E+14
90	11.111	.788	2.082E+00	6.089E+03	4.941E+14
95	10.526	.792	1.703E+00	5.423E+03	6.759E+14
100	10.000	.794	1.447E+00	4.839E+03	8.915E+14
110	9.091	.798	1.132E+00	3.907E+03	1.412E+15
120	8.333	.797	9.618E-01	3.190E+03	2.035E+15
130	7.692	.798	8.693E-01	2.630E+03	2.730E+15
140	7.143	.800	8.236E-01	2.230E+03	3.399E+15

TEMP	1000/T	RATIO	RESISTIVITY	MOBILITY	CONCENTRATION
150	6.667	.799	8.106E-01	1.882E+03	4.092E+15
160	6.250	.799	8.219E-01	1.617E+03	4.699E+15
170	5.882	.797	8.519E-01	1.392E+03	5.262E+15
180	5.556	.799	8.981E-01	1.205E+03	5.766E+15
190	5.263	.797	9.579E-01	1.071E+03	6.085E+15
200	5.000	.799	1.030E+00	9.512E+02	6.372E+15
210	4.762	.796	1.112E+00	8.407E+02	6.675E+15
220	4.545	.798	1.206E+00	7.663E+02	6.756E+15
230	4.348	.797	1.307E+00	6.734E+02	7.093E+15
240	4.167	.799	1.412E+00	6.085E+02	7.219E+15
250	4.000	.797	1.539E+00	5.446E+02	7.446E+15
260	3.846	.798	1.671E+00	5.000E+02	7.471E+15
270	3.704	.796	1.806E+00	4.601E+02	7.512E+15
280	3.571	.798	1.958E+00	4.176E+02	7.634E+15
290	3.448	.796	2.107E+00	3.791E+02	7.815E+15
300	3.333	.798	2.267E+00	3.523E+02	7.817E+15
310	3.226	.797	2.429E+00	3.260E+02	7.883E+15

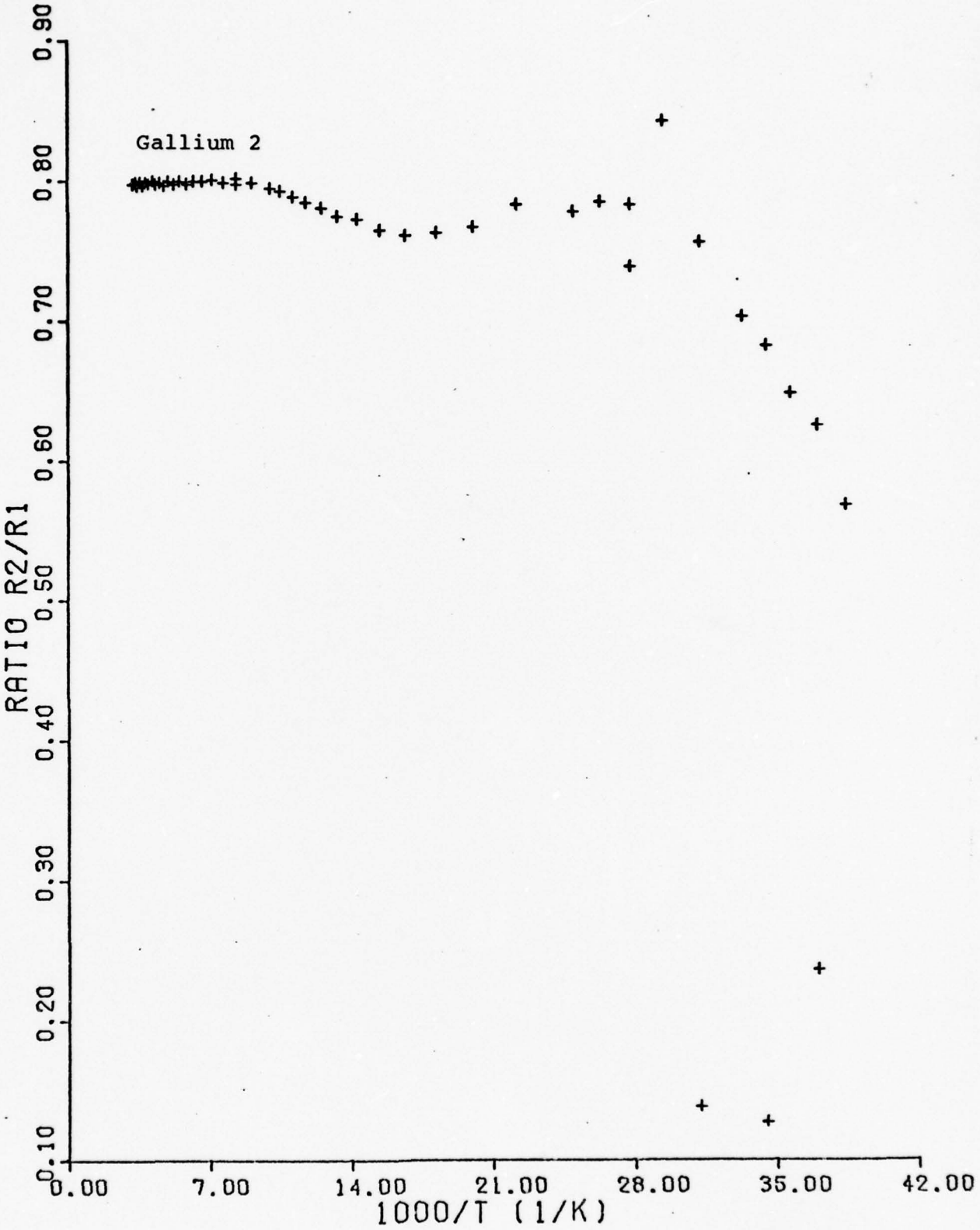

Figure A44 Resistivity Ratio versus 1000/T

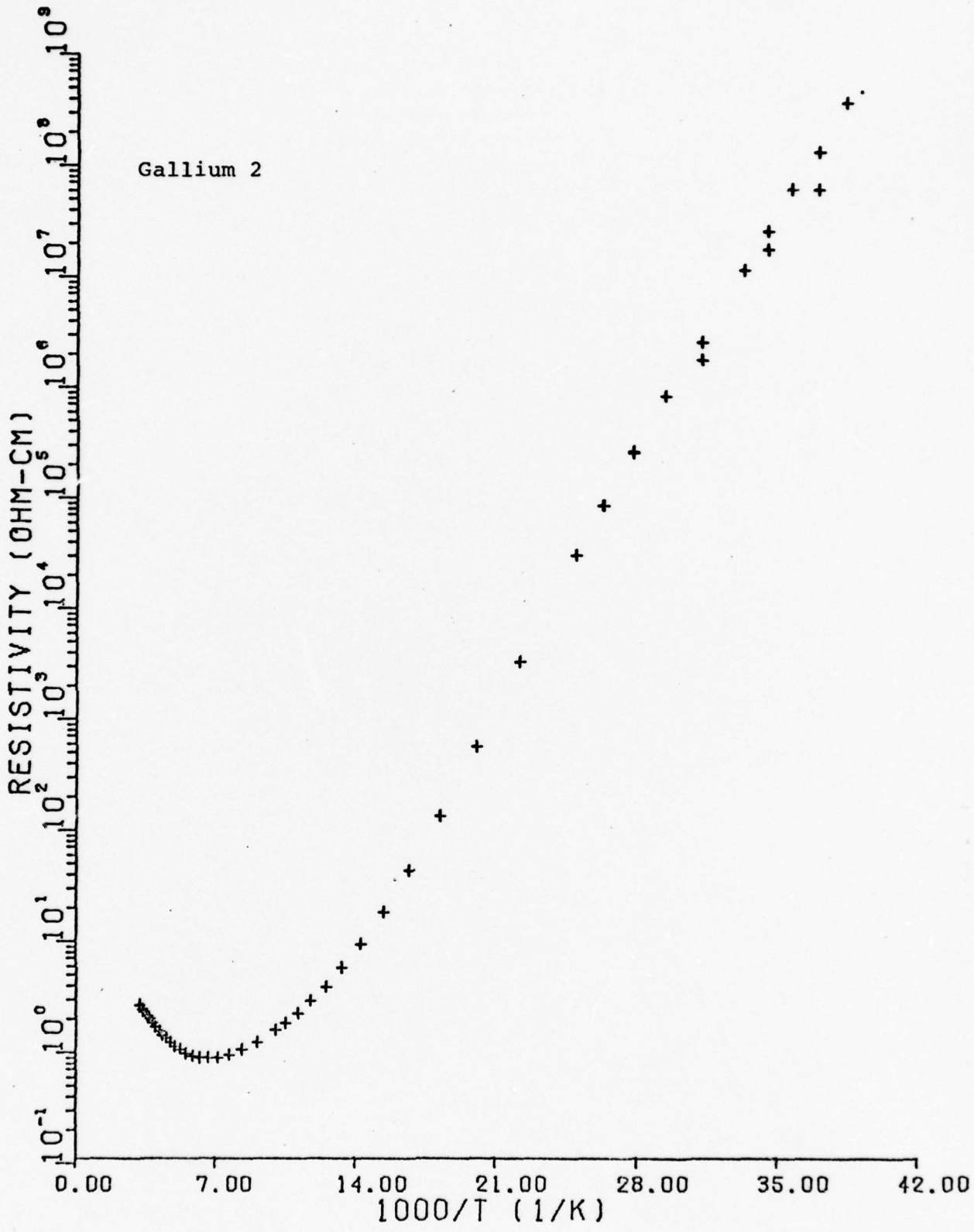

Figure A45 Resistivity versus 1000/T

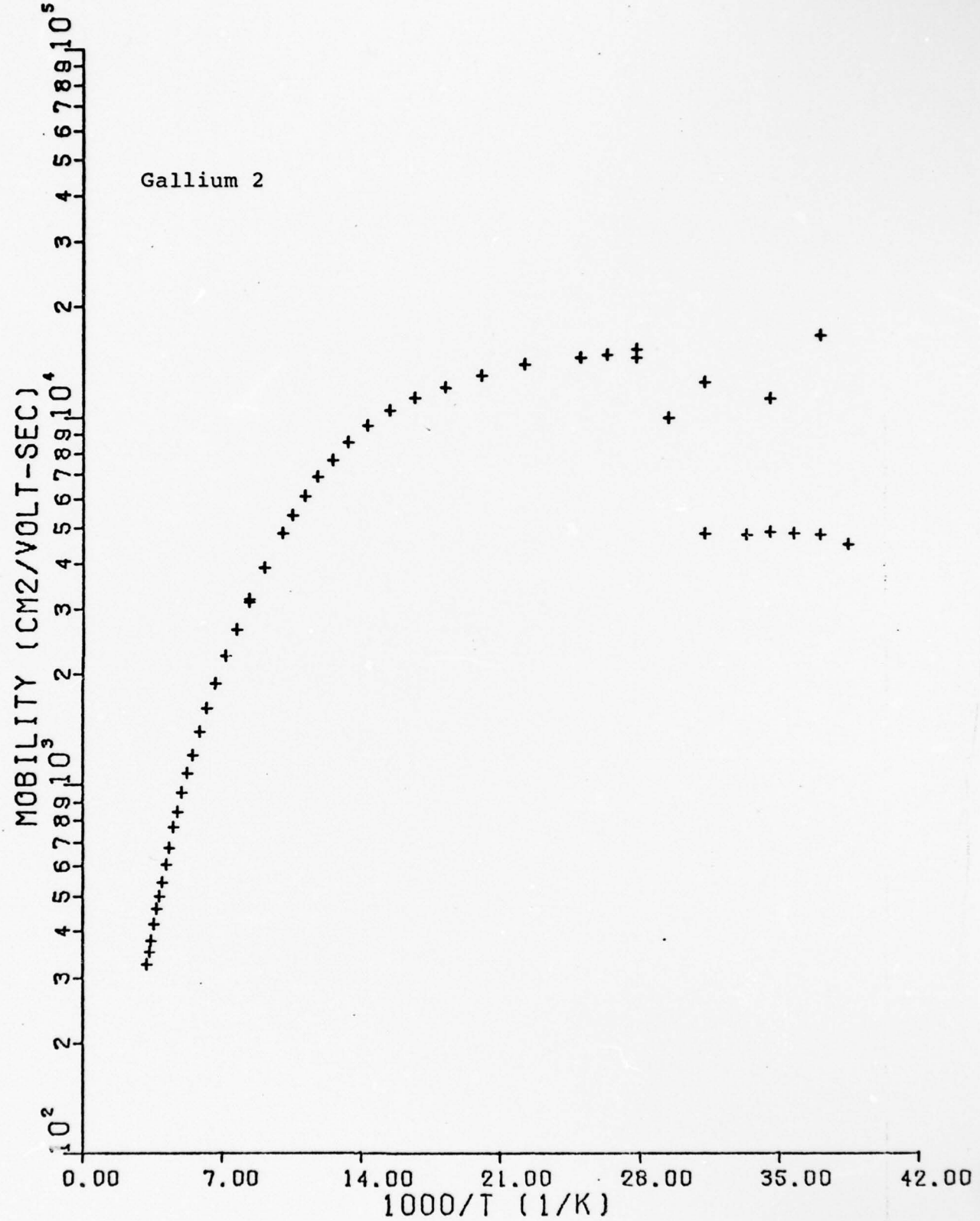

Figure A46 Mobility versus 1000/T

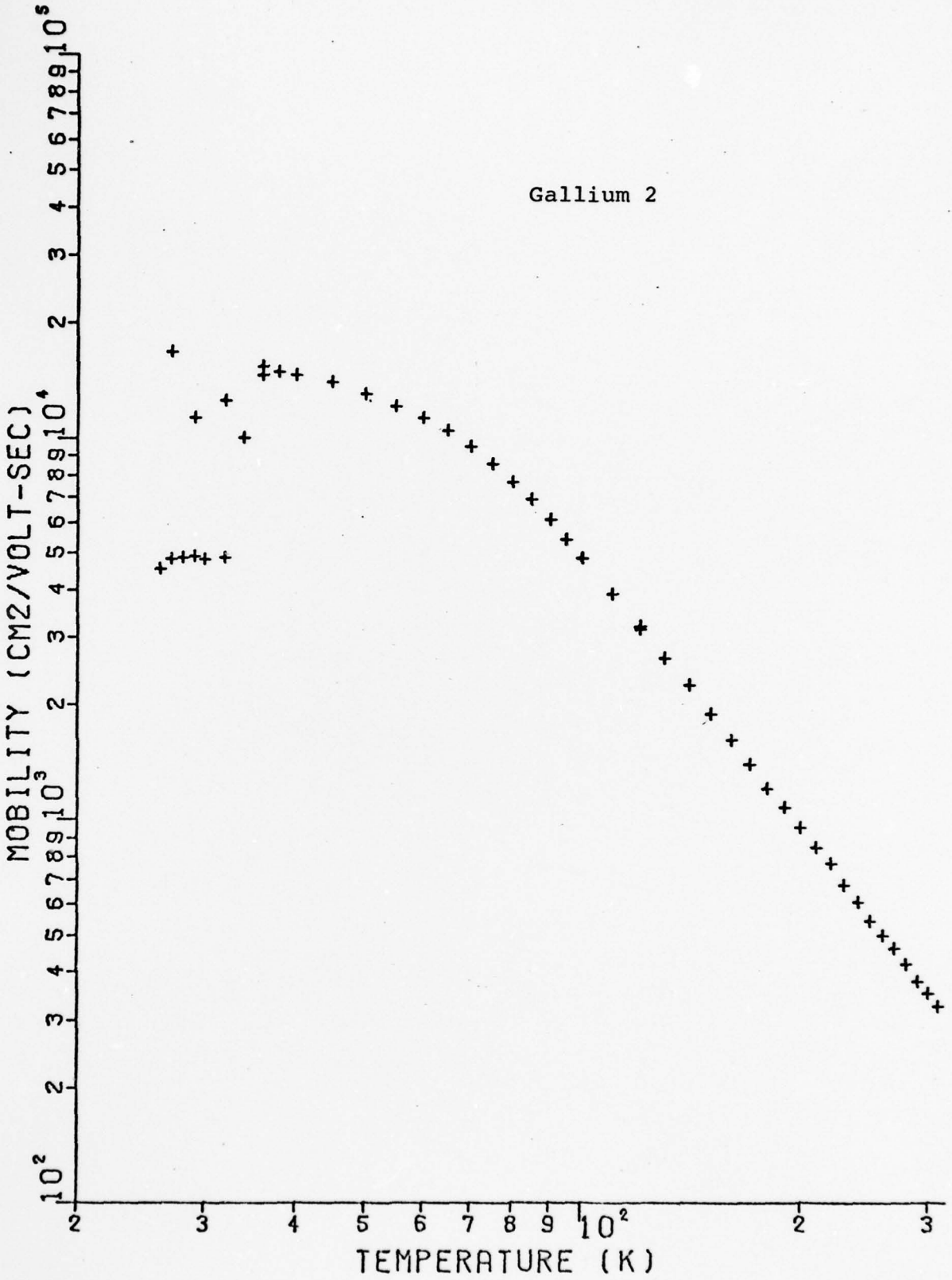

Figure A47 Mobility versus Temperature

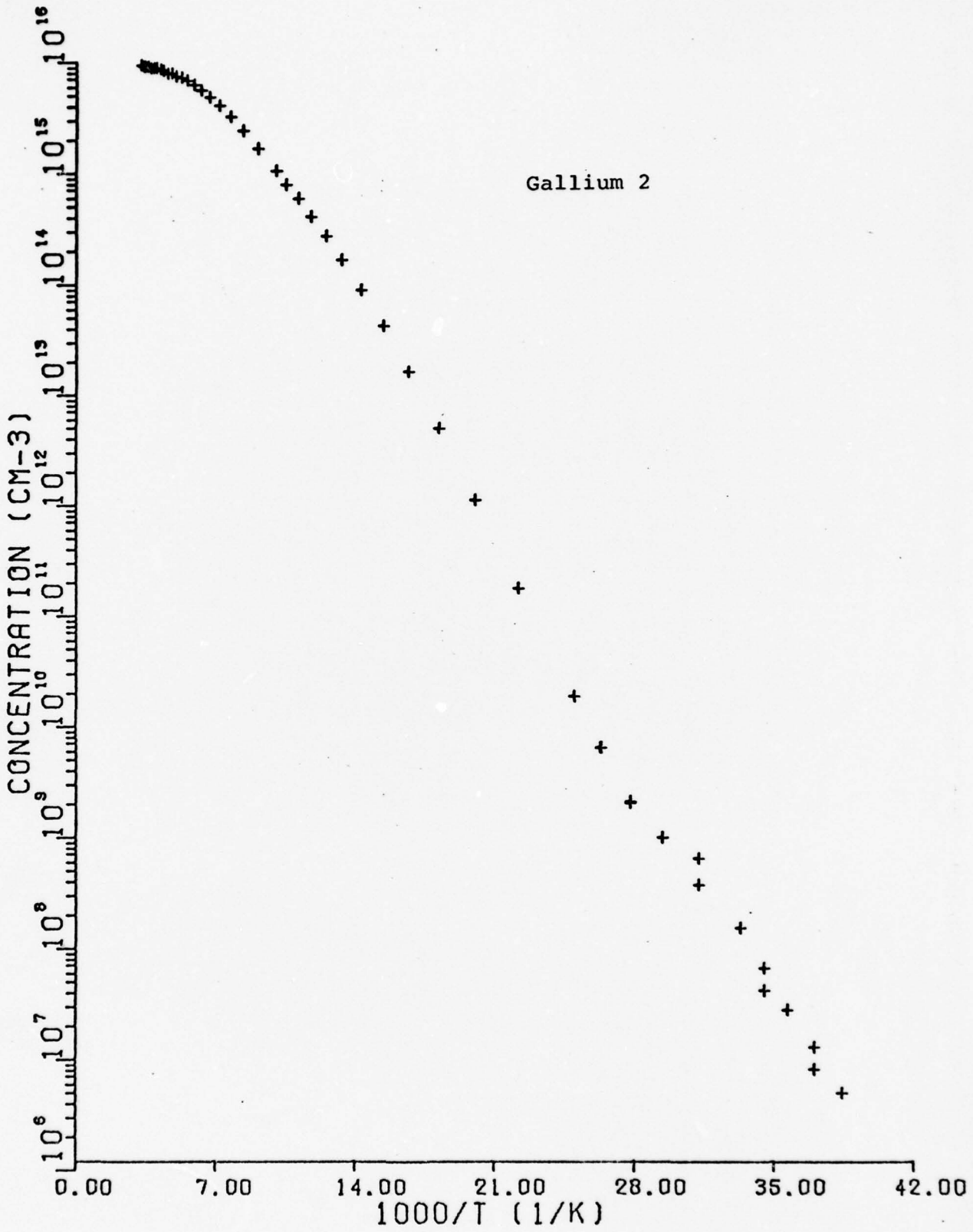

Figure A48 Carrier Concentration versus 1000/T

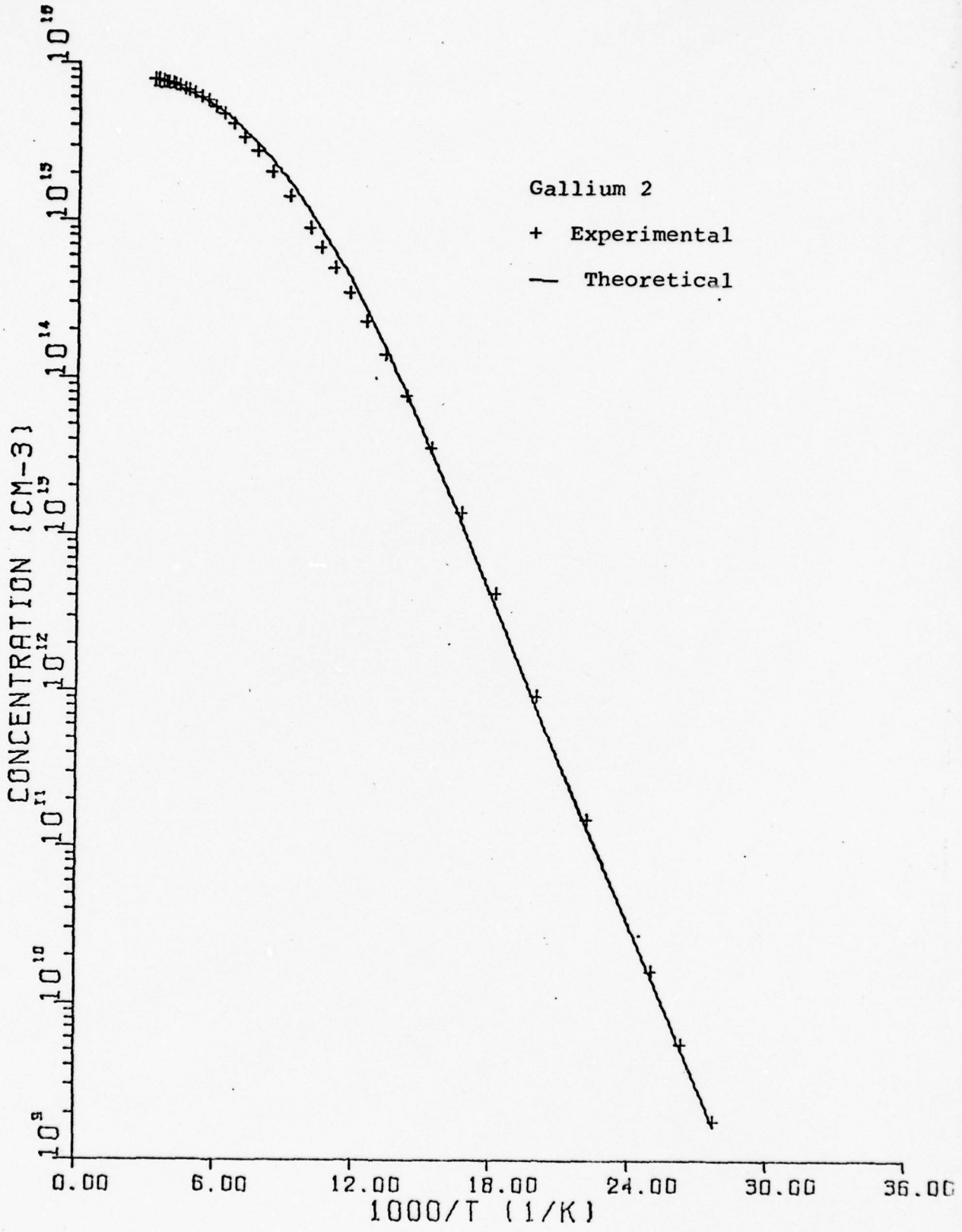

Figure A49 Carrier Concentration versus 1000/T

Undoped

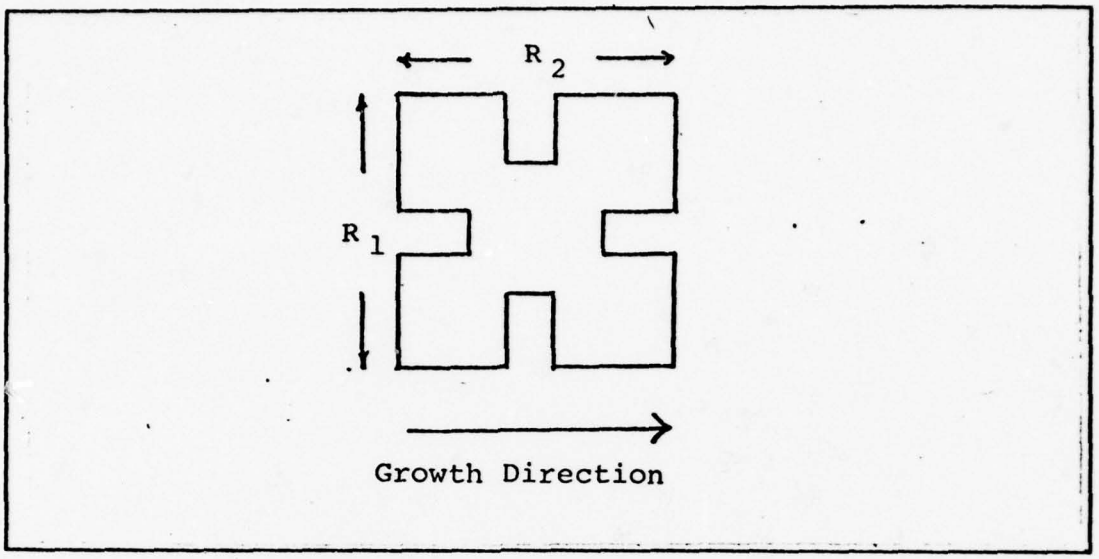

Figure A50 Resistances Relative to the Growth Axis

$N_a = 4.767 \times 10^{14}$ cm^{-3}

$N_d = 3.300 \times 10^{14}$ cm^{-3}

$\epsilon_a = .0397$ ev

thickness .0174 cm

"Undoped"

Table XII

TEMP	1000/T	RATIO	RESISTIVITY	MOBILITY	CONCENTRATION
20	50.000	.160	9.044E+06	1.326E+04	5.206E+07
21	47.619	.433	6.169E+06	1.020E+04	9.918E+07
21	47.619	.197	4.120E+06	1.493E+04	1.015E+08
22	45.455	.306	2.403E+06	1.389E+04	1.871E+08
22	45.455	.236	1.982E+06	1.734E+04	1.817E+08
23	43.478	.285	1.077E+06	7.038E+03	8.235E+08
23	43.478	.236	9.400E+05	4.136E+03	1.606E+09
24	41.667	.526	3.362E+05	1.386E+04	1.340E+09
24	41.667	.649	2.911E+05	1.069E+04	2.007E+09
25	40.000	.587	2.523E+05	1.488E+04	1.663E+09
25	40.000	.679	2.050E+05	1.581E+04	1.926E+09
26	38.462	.540	1.585E+05	1.948E+04	2.022E+09
26	38.462	.605	1.432E+05	2.098E+04	2.078E+09
27	37.037	.556	9.112E+04	2.602E+04	2.633E+09
27	37.037	.585	8.731E+04	2.414E+04	2.961E+09
28	35.714	.598	5.700E+04	2.618E+04	4.184E+09
28	35.714	.580	5.579E+04	2.66LE+04	4.204E+09
29	34.483	.663	3.380E+04	2.715E+04	6.803E+09
30	33.333	.704	2.145E+04	2.817E+04	1.033E+10
32	31.250	.817	8.490E+03	2.933E+04	2.507E+10
34	29.412	.937	3.528E+03	2.963E+04	5.971E+10
36	27.778	1.035	1.587E+03	2.745E+04	1.433E+11
38	26.316	1.068	7.450E+02	2.890E+04	2.889E+11
40	25.000	1.117	3.804E+02	2.783E+04	5.898E+11
45	22.222	1.176	9.130E+01	2.537E+04	2.695E+12
50	20.000	1.191	3.242E+01	2.236E+04	8.609E+12
55	18.182	1.200	1.610E+01	1.951E+04	1.987E+13
60	16.667	1.203	1.028E+01	1.703E+04	3.567E+13
65	15.385	1.208	7.828E+00	1.491E+04	5.348E+13

TEMP	1000/T	RATIO	RESISTIVITY	MOBILITY	CONCENTRATION
70	14.286	1.206	6.686E+00	1.314E+04	7.105E+13
75	13.333	1.208	6.159E+00	1.168E+04	8.676E+13
80	12.500	1.207	6.010E+00	1.043E+04	9.957E+13
85	11.765	1.208	6.048E+00	9.402E+03	1.098E+14
90	11.111	1.213	6.230E+00	8.521E+03	1.176E+14
95	10.526	1.211	6.516E+00	7.762E+03	1.234E+14
100	10.000	1.211	6.862E+00	7.031E+03	1.294E+14
110	9.091	1.212	7.741E+00	5.926E+03	1.361E+14
120	8.333	1.210	8.846E+00	4.947E+03	1.427E+14
130	7.692	1.212	1.016E+01	4.177E+03	1.470E+14
140	7.143	1.210	1.174E+01	3.518E+03	1.512E+14
150	6.667	1.213	1.359E+01	2.974E+03	1.544E+14
160	6.250	1.211	1.575E+01	2.513E+03	1.577E+14
170	5.882	1.211	1.822E+01	2.145E+03	1.597E+14
180	5.556	1.213	2.096E+01	1.831E+03	1.626E+14
190	5.263	1.211	2.408E+01	1.580E+03	1.641E+14
200	5.000	1.208	2.748E+01	1.363E+03	1.667E+14
210	4.762	1.210	3.118E+01	1.184E+03	1.691E+14
220	4.545	1.209	3.521E+01	1.031E+03	1.720E+14
230	4.348	1.210	3.953E+01	9.115E+02	1.732E+14
240	4.167	1.210	4.422E+01	7.987E+02	1.767E+14
250	4.000	1.210	4.919E+01	7.087E+02	1.791E+14
260	3.846	1.209	5.450E+01	6.336E+02	1.808E+14
270	3.704	1.210	5.981E+01	5.703E+02	1.830E+14
280	3.571	1.210	6.490E+01	5.122E+02	1.878E+14
300	3.333	1.211	7.687E+01	4.271E+02	1.901E+14
320	3.125	1.211	9.009E+01	3.535E+02	1.960E+14

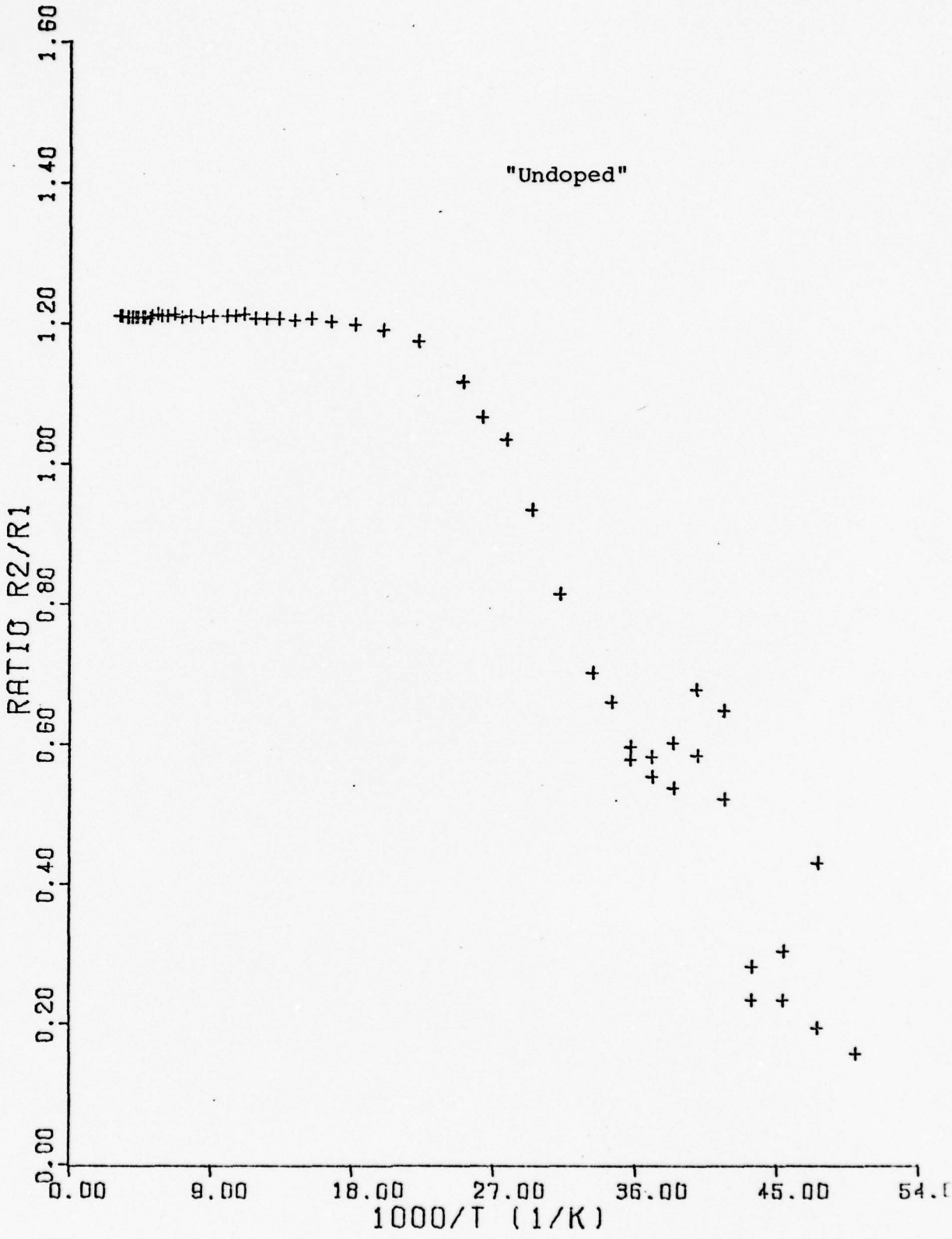

Figure A51 Resistivity Ratio versus 1000/T

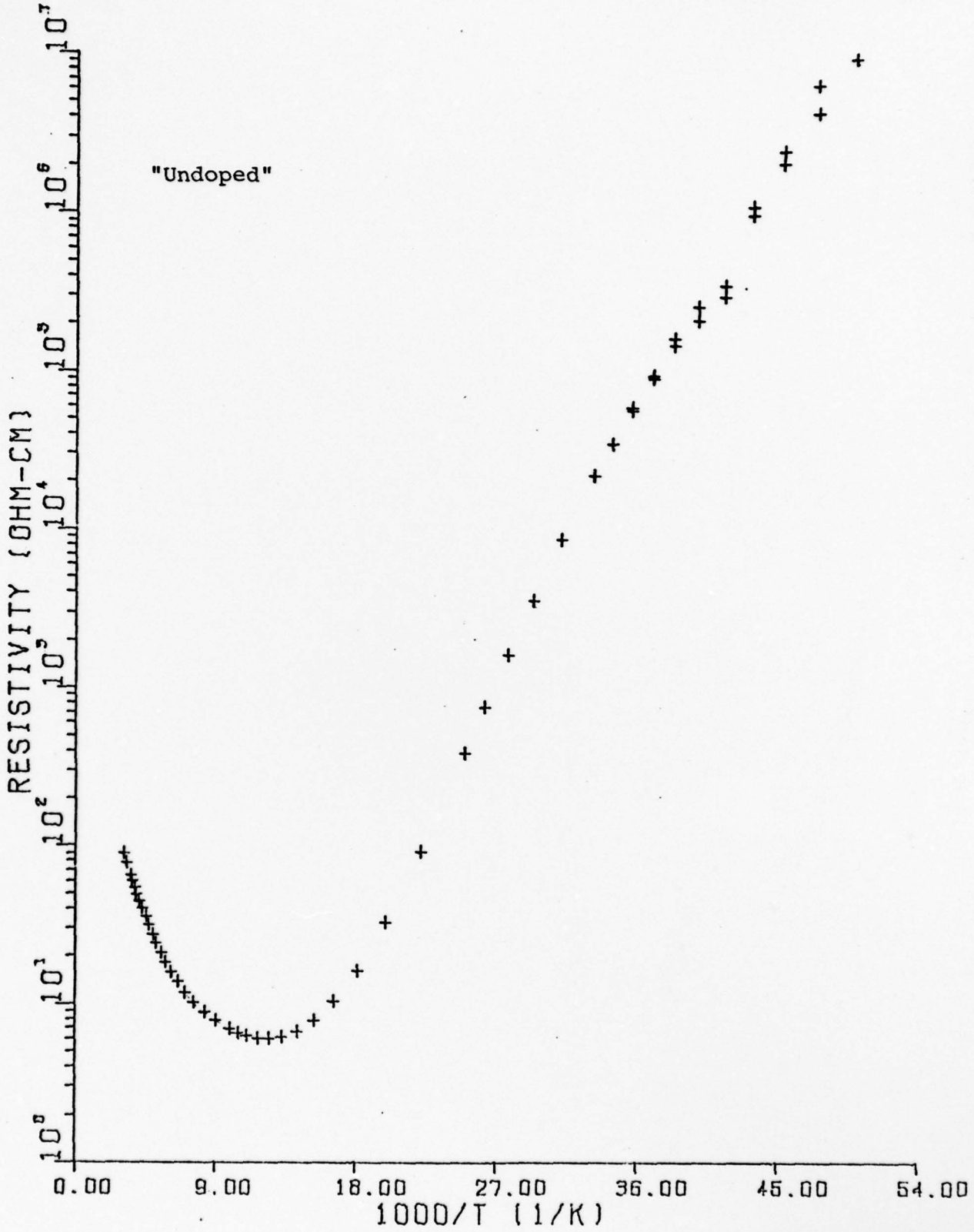

Figure A52 Resistivity versus 1000/T

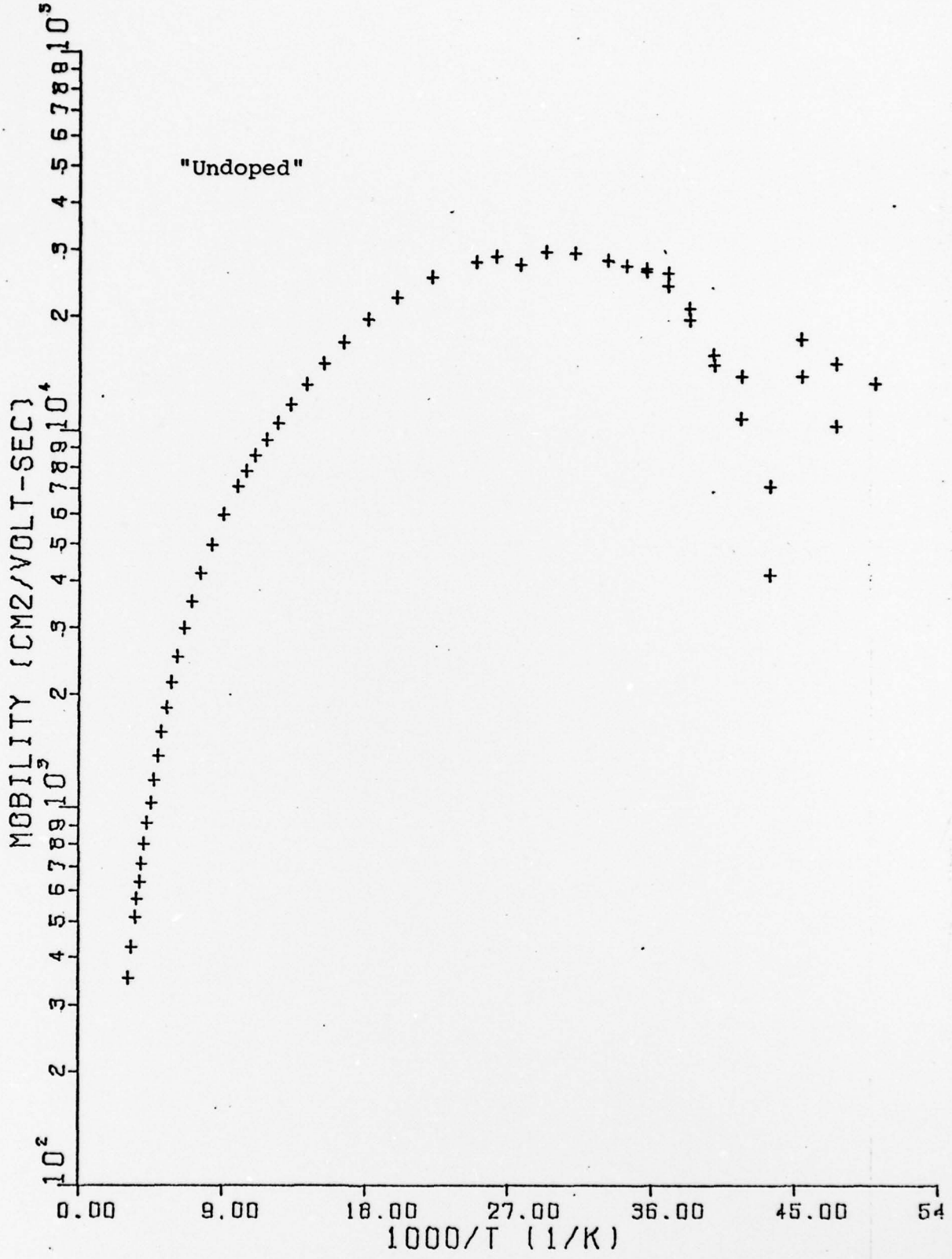

Figure A53 Mobility versus 1000/T

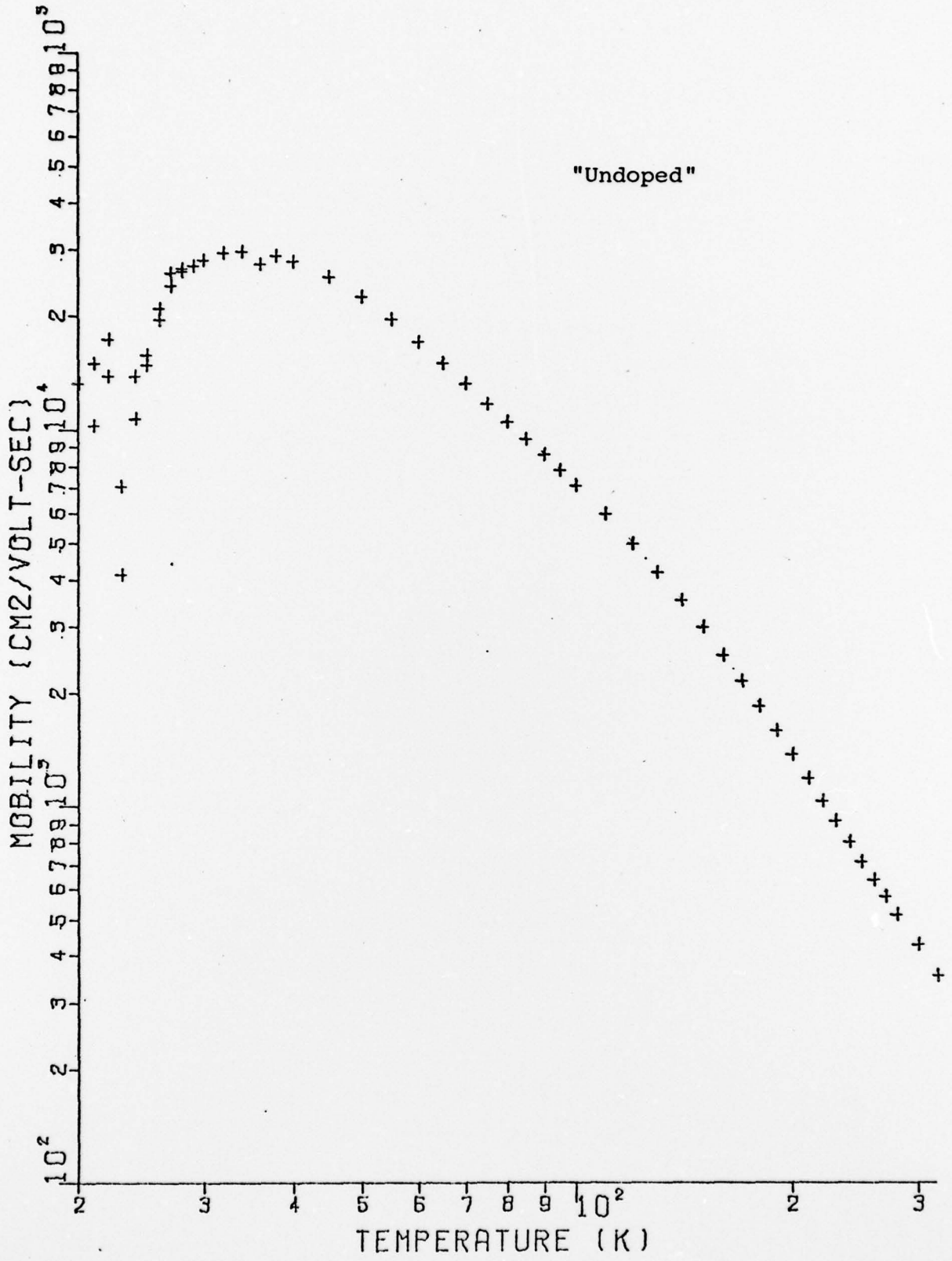

Figure A54 Mobility versus Temperature

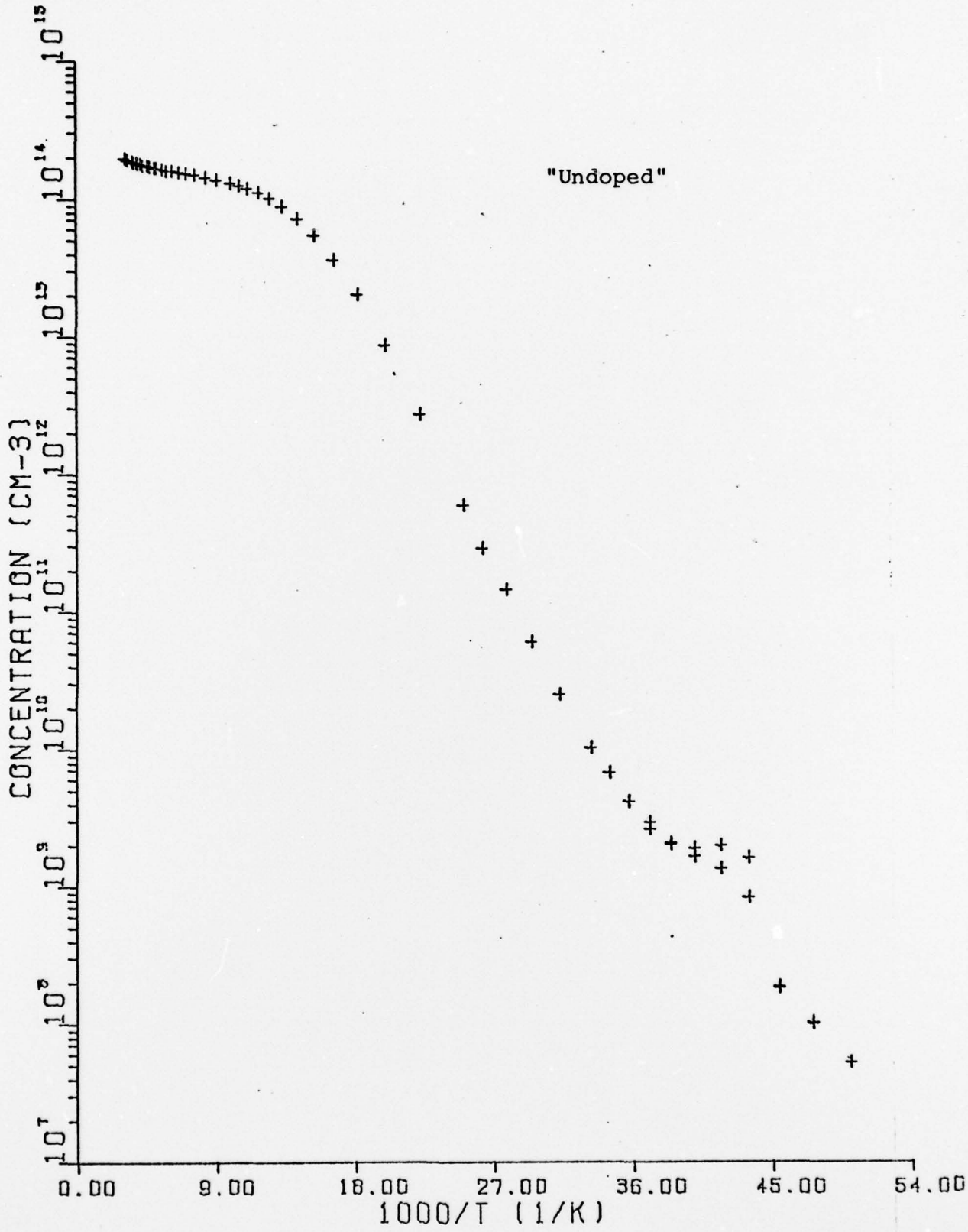

Figure A55 Carrier Concentration versus 1000/T

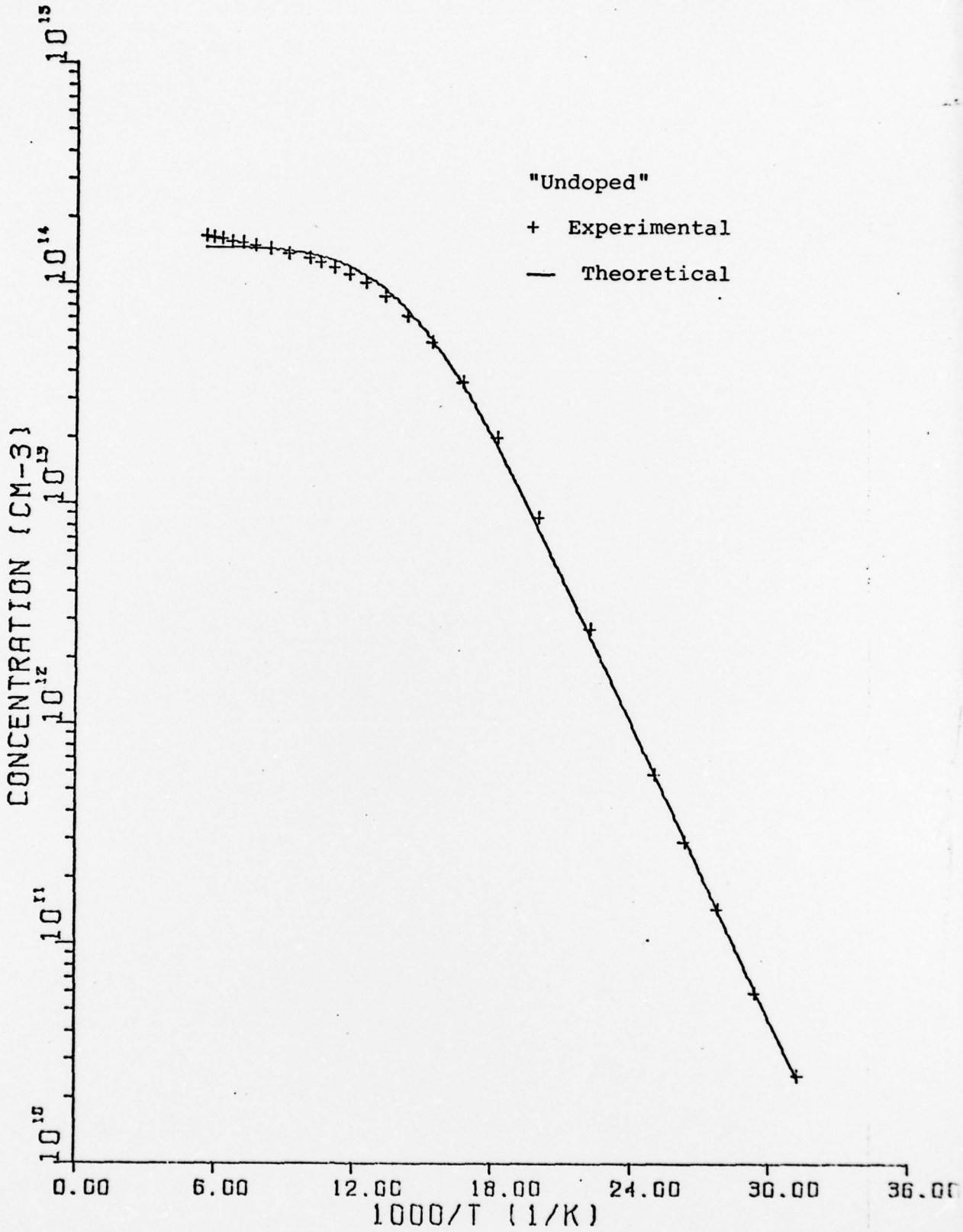

Figure A56 Carrier Concentration versus 1000/T

Appendix B

This appendix explains the derivations of two results used for analysis in this thesis. First is shown, at low temperatures, that the natural logarithm of resistivity plotted against $1/T$ is a straight line. And the slope of the line is proportional to the activation energy. Second, the propagation of error in carrier concentration is derived in more detail.

Resistivity versus 1/T

Starting with equation (28):

$$p = \tfrac{1}{2} (N_D + F) \left[\sqrt{1 + \frac{4 (N_A - N_D) F}{(N_D + F)^2}} - 1 \right] \qquad \text{(B1)}$$

where

$$F = \tfrac{1}{4} N_F \exp (-\epsilon_a / kT)$$

$$N_F = \frac{2 (2 \pi m_k^* kT)^{3/2}}{h^3}$$

At low temperatures where $N_a >> p$ this equation becomes:

$$p = \frac{N_A - N_D}{N_D} F \qquad \text{(B2)}$$

Since,

$$\rho = (pe\mu)^{-1} \tag{B3}$$

equation (B2) can be substituted into this equation to yield:

$$\rho = \frac{1}{e\mu}\left[\left(\frac{N_A - N_D}{N_D}\right)\frac{N_F}{4}\right]^{-1} \exp\left(\epsilon_a/kT\right) \tag{B4}$$

Taking the natural logarithm of both sides and rearranging will produce:

$$\ln \rho = \ln K_1 - \ln \mu - \ln T^{3/2} + \epsilon_a/kT \tag{B5}$$

where

$$K_1 = \frac{1}{e}\left[\left(\frac{N_A - N_D}{2\,N_D}\right)\frac{(2\pi\, m_k^{*}\, k)^{3/2}}{h^3}\right]^{-1}$$

Let $X = 1/T$ then;

$$\ln \rho = \ln K_1 - \ln \mu + \frac{3}{2}\ln X + \frac{\epsilon_a X}{k} \tag{B6}$$

Now taking $\frac{d(\ln \rho)}{dx}$ yields:

$$\frac{d \ln \rho}{dx} = \frac{3}{2x} + \frac{\epsilon_a}{k} \tag{B7}$$

Since $\mu \approx$ a constant at low temperatures, $\ln \mu$ is isnored. Now substituting back in $1/T$ for X gives:

$$\Delta \ln \rho = \left[3/2\ T + \frac{\epsilon_a}{k} \right] \Delta \frac{1}{T} \qquad \text{(B8)}$$

And at low temperatures

$$3T/2 << \epsilon_a/k$$

Thus, a plot of $\ln \rho$ versus $1/T$ is linear at low temperature

$$\Delta \ln \rho \approx \frac{\epsilon_a}{k} \Delta \left(\frac{1}{T}\right) \qquad \text{(B9)}$$

Error Propagation for One Level Acceptors

This sub-section derives equation (32) in more detail. The error in carrier concentration with respect to temperature is determined from:

$$\frac{dp}{dT} = \frac{dp}{dF} \frac{dF}{dT} \qquad \text{(B10)}$$

Rearranging equation (7) into its quadratic form yields:

$$p^2 + (N_D + F)p + (N_D - N_A)F = 0 \qquad \text{(B11)}$$

Then taking the derivative $\frac{dp}{dF}$ gives:

$$2p \frac{dp}{dF} + (N_D + F) \frac{dp}{dF} + p + (N_D - N_A) = 0 \qquad \text{(B12)}$$

and rearranging yields:

$$\frac{dp}{dF} = \frac{N_A - N_D - p}{2p + N_D + F} \qquad \text{(B13)}$$

Since,

$$\frac{dF}{dT} = \frac{3F}{2T} + \frac{F\epsilon_a}{kT^2} \qquad \text{(B14)}$$

equations (B13) and (B14) can then be substituted into equation (B10), which will result in:

$$\frac{dp}{dT} = \left(\frac{N_A - N_D - p}{2p + N_D + F} \right) \left(\frac{3}{2} + \frac{\epsilon_a}{kT} \right) \frac{F}{T} \qquad \text{(B15)}$$

The variance in carrier concentration with respect to temperature is:

$$\Delta p = \frac{dp}{dT} \Delta T \qquad \text{(B16)}$$

And the relative error in p is defined by

$$r = \frac{\Delta p}{p} = \frac{dp}{dT} \frac{\Delta T}{p} \qquad \text{(B17)}$$

Then substituting in equation (B15) into equation (B17) produces equation (32).

$$r(\%) = 100 \left(\frac{N_A - N_D - p}{2p + N_D + F} \right) \left(\frac{3}{2} + \frac{\epsilon_a}{kT} \right) \frac{F\Delta T}{p\,T} \qquad \text{(B18)}$$

Appendix C

Shown in this appendix is the Sloan dektak surface profile scan of the "undoped" web material. This scan was performed by Dr. Melvin Ohmer in the Air Force Materials Laboratory, Wright-Patterson AFB, Ohio. The Sloan Dektak Surface Profile System consists of the Dektak and associated chart recorder. This instrument is used for the measurement of surface profiles and surface evaluations differences from less than 25 $\mathring{A}$ to a maximum of 10^6 $\mathring{A}$. The scan for the undoped silicon sample is shown in Figure C1.

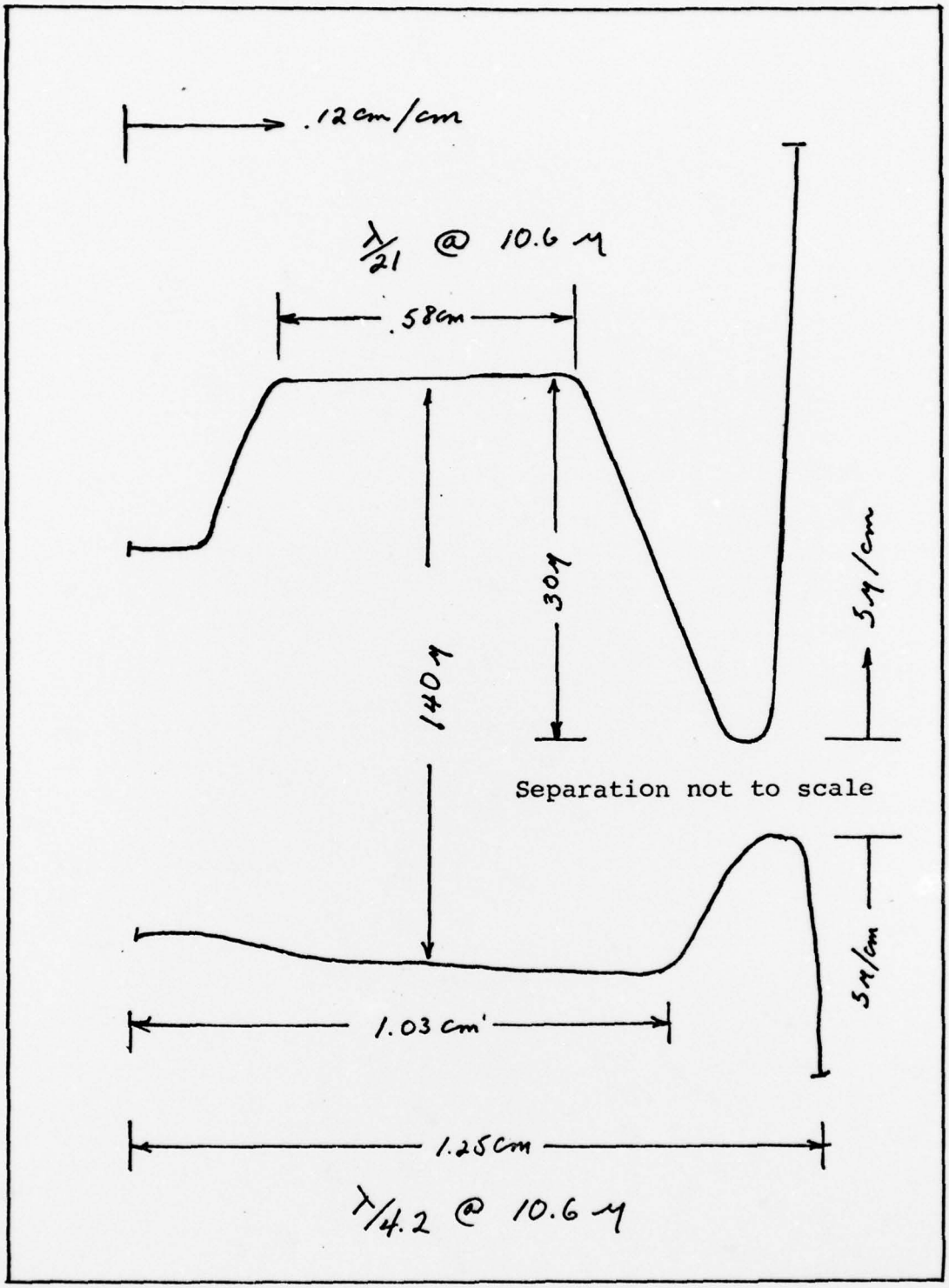

Figure C1 Dektak Scan

Appendix D

This appendix shows a flow chart of the least-squares curve-fitting computer program used in this thesis. To use this program the carrier concentration data and its corresponding temperatures are first read into the program. The natural logarithm of the concentration is then calculated, since the values of p vary from 10^7 - 10^{16} cm^{-3}.

This program calculates N_a, N_d, and ϵ_a by finding the best fit of equation (7) to the data. Ranges of N_a, N_d, ϵ_a, and best guesses of these values are fed in to start the searching routine. By taking random, gradient, average, and jump steps, which ever it determines is yielding the best result, the program fits the charge balance equation to the data. This is accomplished by changing N_a, N_d, and ϵ_a; such that the least deviation between the experimental results and theoretical values calculated exists.

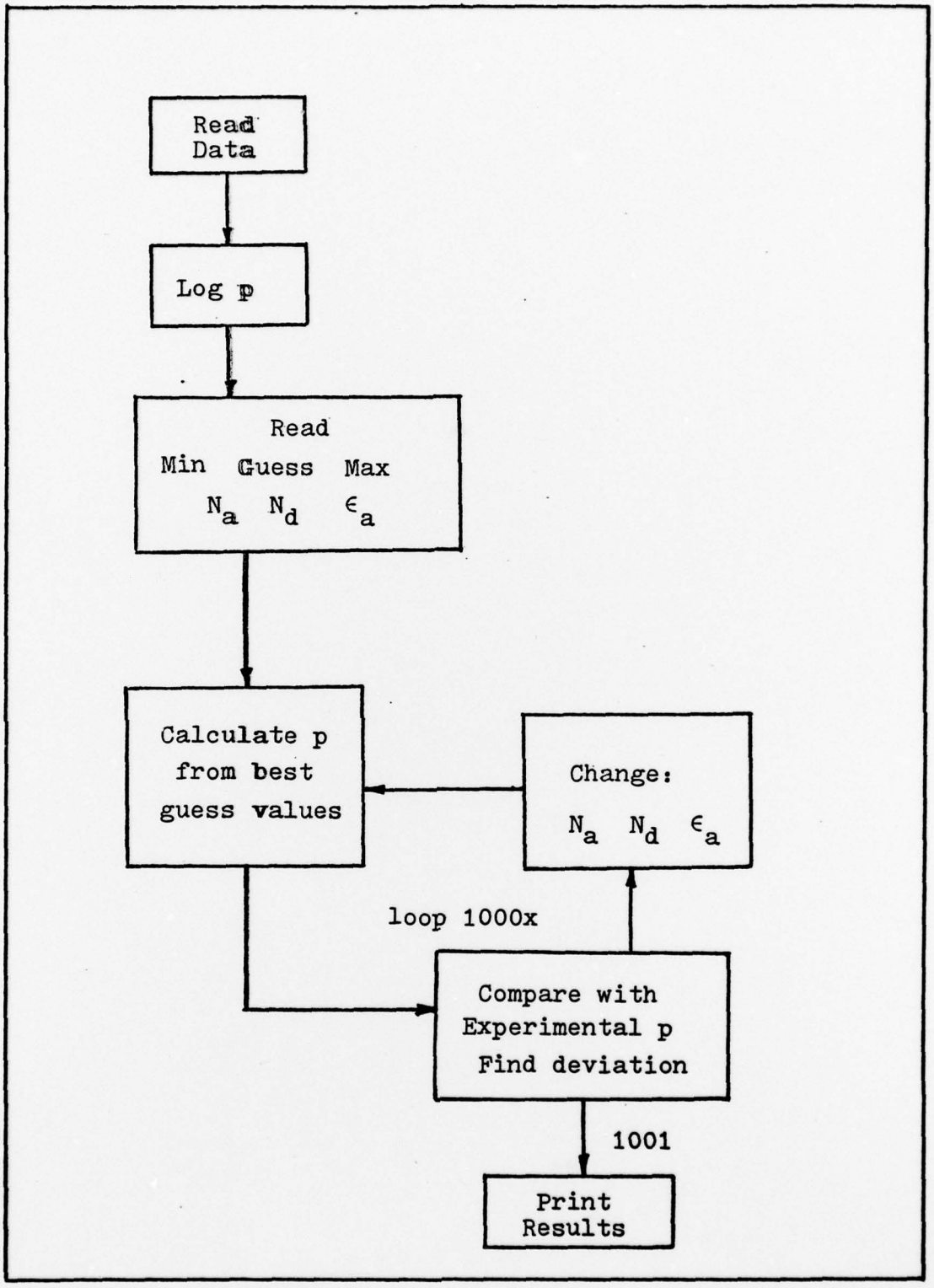

Figure D1 Flow Chart

Vita

Thomas J. Settecerri was born on 1 February 1948 in Detroit, Michigan. He graduated from high school in Detroit in 1966 and attended Michigan State University from which he received the degree of Bachelor of Science in Physics in 1969. After graduation, he received a commission in the USAF through the OTS program. He completed navigator training school at Mather AFB, California and received his wings in July 1970. He attended Electronic Warfare School and upon graduation was assigned to fly EB-57 aircraft at Otis AFB, Massachusetts. He later flew the same aircraft at Westover AFB, Massachusetts and Malmstrom AFB, Montana. In June 1976 he entered the School of Engineering, Air Force Institute of Technology.

Permanent address: 20499 Fairview Dr.
Dearborn Hts, Mich.
48127